UNIVERSITÀ DEGLI STUDI DI PAVIA

DOTTORATO IN SCIENZE CHIMICHE E FARMACEUTICHE E INNOVAZIONE INDUSTRIALE
(XXXV Ciclo)
Coordinatore: Chiar.mo Prof. Giorgio Colombo

Structure-property correlation in low-dimensional perovskites

Tesi di Dottorato di
Rossella Chiara

AA 2021/2022

Tutor
Chiar.mo Prof. *Lorenzo Malavasi*

CONTENTS

ABSTRACT

In the last few decades, the development of technologies based on organic-inorganic metal halide perovskites has been widely pursued by physical-chemistry researchers. However, current priority of the involved scientific community is to overcome the crucial issue of instability of conventional three-dimensional (3D) perovskites. For this reason, two-dimensional (2D) materials have increasingly appealed scientists due to their excellent properties in terms of environmental stability, as well as fascinating structural, optical and electronic characteristics; nevertheless, these compounds still remain quite unexplored. A further great challenge is finding appropriate and efficient solutions to overcome the toxicity issues of lead, which is the most studied metal in perovskites, due to the appealing functional properties it confers to the aforementioned materials.

In the light of these premises, the present work is focused on the development and the characterization of new 2D perovskite materials with the purpose of modulating and optimizing the physical-chemical properties. Through suitable and rational combinations of organic spacers, metallic cations and halogens, novel 2D phases were investigated, disclosing different structural distortion degrees and consequently new potential properties. Therefore, this project aimed to define a rigorous relationship between crystal structure and functional properties in new 2D lead-based and lead-free perovskites.

Each section of the dissertation describes a specific category of incorporated organic spacers, namely aliphatic and aromatic cations, with a single benzene ring and double aromatic ring, monoammonium and diammonium cations, which have been used for the synthesis of lead-, germanium and tin-based systems. Numerous spacers have already been identified; however, the plethora of known structures needs to be expanded in order to achieve a full understanding of 2D perovskite, in terms of structure-

property relationships, stability and performances for the design of novel and optimized devices. Besides traditional structural and optical investigations, stability studies were performed on novel materials under different moisture, light, temperature and pressure conditions, providing additional appropriate correlations between crystal structure and functional properties.

The results of the present work confirm the greater stability and structural diversity of 2D perovskites with respect to 3D compounds, making 2D materials as suitable candidates for the incorporation in high-performance devices.

SUMMARY

The focus of this thesis is the synthesis and the characterization of new hybrid low-dimensional metal halide perovskites for possible applications in opto-electronic devices and in photocatalysis, with a special attention to two-dimensional (2D) materials. The aim of the project was to evaluate functional, optical and electronic properties of these novel compounds in relation to structural changes induced by different compositions in terms of metallic cation, halogen and organic spacer or induced by temperature and pressure effects, in order to define a rigorous correlation between crystal structure and physical properties.

The thesis is divided in 8 chapters.

Chapter 1 provides a detailed background of the perovskite field, including structure, stability, composition and properties.

C**hapter 2** reports a description of the synthesis techniques used for the growth of 2D single crystals.

The following chapters comprise the experimental section, divided on the basis of the organic spacer incorporated in the structure. In order to better organize the experimental results, the choice was to include in the thesis our published papers about the discussed topics, each of them endowed with its own bibliography.

In **chapter 3,** 2D Ruddlesden-Popper perovskites based on monoammonium aliphatic cations are investigated, exploring the effect on structural and physical properties due to the elongation of the organic chain in lead-based systems.

In **chapter 4**, in order to study lead-free compounds and more complex organic cations, as well as to produce novel phases with new potential properties, germanium-based systems including single-ring aromatic spacers are presented.

Chapter 5 deals with single-ring aromatic cations containing a diammonium group, with the aim of exploring 2D perovskites belonging to the Dion-Jacobson type.

In **chapter 6** diphenyl spacers are investigated and the photocatalytic activity of the resulted perovskites is tested.

Chapter 7 provides a discussion on high-pressure studies and the relative changes in structural and optical properties of the examined perovskites. The last chapter summarizes the main outcomes of the work and gives an overview of future perspectives for this class of materials.

CHAPTER 1.

INTRODUCTION

Over the last decades, Metal Halide Perovskites (MHPs) have become one of the most promising materials for the application in optoelectronic devices such as solar cells, light emitting diodes (LEDs), lasers, detectors, field effect transistors (FETs), because of their fascinating physical properties in terms of long carrier lifetime, high mobility, structural defects and tunability. [1,2] Besides the classical deeply investigated three-dimensional (3D) perovskites, lower-dimensional materials, in particular hybrid two-dimensional (2D) compounds, have attracted increasing interest in the scientific community, due to the possibility of tuning the physical properties by modifying layer thickness, cage and spacer cations. [3] Moreover, the presence of organic spacer plays an important role in improving the stability and hydrophobicity of these perovskites with respect to 3D materials. [4]

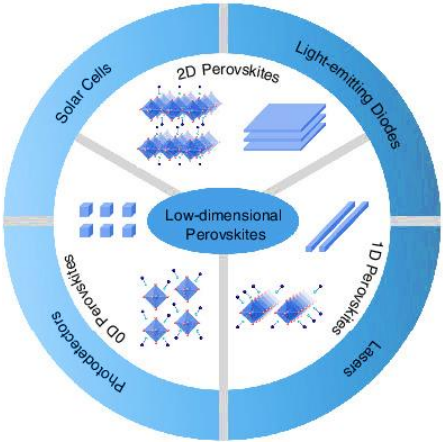

Figure 1 *Possible applications of low-dimensional MHPs. Reprinted with permission from ref. [5] Copyright © 2020 InfoMat.*

Initially, these promising materials have been a subject of interest as protective layers of 3D perovskites for solar cells. However, their current use is not restricted to photovoltaic application and, thanks to the discovery of new properties of these low-dimensional materials, they become attractive also for other technology fields (Figure 1), such as manufacturing of light-emitting diodes, lasers, photodetectors, [5] as well as in photocatalysis.
Nevertheless, application of 2D perovskites in optoelectronic devices requires robust studies aimed at explaining the effect on structure, properties, and performances of the inclusion of different spacers in these novel materials. [6] Indeed, the opportunity of modulating the properties through the combination of metals such as Pb, Sn, Ge, Bi and different halides with all the possible organic spacers offers a rich ground of versatile tools. Through computational elaborations, the existence of more than 90 thousand perovskite materials bearing various dimensionalities has been predicted, although only an extremely limited percentage of them has been synthetized and characterized up to date. [7] In particular, evidences correlating functional properties of these materials to their peculiar crystal structure are relatively unexplored in the current scientific literature, thus representing a crucial issue for investigators.

1.1 Perovskites

Originally, the concept of *perovskite* was introduced for the $CaTiO_3$ mineral in 1839 by Gustav Rose and its name was subsequently derived from the Russian mineralogist Count Lev Alekseyevich von Perovski. Later, the perovskite term was extended to all the families of materials with the same formula ABX_3. In general, perovskite minerals are found in nature as oxides, mainly silicates, but they can also occur as fluorides, chlorides, hydroxides, arsenides, and intermetallic compounds. [8] After a century since the first identification of natural oxide perovskite, a class of artificial inorganic metal trihalide perovskite with general stoichiometry ABX_3 (X = Cl, Br, I) was reported in literature, synthetized through a simple reaction between two

salts. [9] The importance of these materials became rather relevant along with the discovery of intriguing electronic properties, as well as of interesting ferro- and antiferromagnetic, ferroelectric and piezoelectric characteristics. The turning point occurred when the introduction of hybrid organic-inorganic systems revealed several advantages in terms of exciton binding energy, lifetimes, and electronic tunability of these novel compounds. [9]

1.1.1 Crystal structure

The ideal perovskite crystal lattice can be described by a primitive cubic structure with *Pm-3m* space group, presenting the general formula ABX_3, where B is a metallic cation, X is oxygen or a halogen and A is a voluminous cation which can be metallic (*totally inorganic perovskite*) or an organic cation (*hybrid organic-inorganic perovskite*). This structure can be visualized as a three-dimensional network of BX_6 octahedra sharing all the corners, while A cations are located among them (Figure 2).

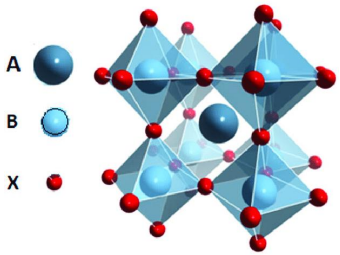

Figure 2 *Schematic representation of ABX_3 perovskite structure.*

The perfect cubic structure presents the highest symmetry and occurs rarely, for example as $SrTiO_3$ (tausonite). Deviations from the ideal stoichiometry can be obtained if A and B cation sites become partially or fully vacant, resulting in the so-called *vacancy-ordered* perovskites, or if

cations are substituted with a mixture of other cations, always maintaining the neutral charge balance, and forming double or quadruple perovskites. Lattice distortions, distorted octahedra, ordered cations, vacancies, and presence of organic cations are the main reasons of the reduced symmetry in the majority of perovskites. [8] The structures resulting from these deviations, reported in Figure 3, are the following:

- Anti-perovskites, in which A and B sites are occupied by a halide and a chalcogenide, respectively, while X sites include a monovalent cation;
- Distorted perovskites, generated from the tilting of the octahedra;
- Vacant perovskites, with A-site vacant BX_3 octahedra;
- Ordered perovskites, in which two B^{2+} metals are replaces by a combination of a M^{+} and a M^{3+} cations;
- Vacancy ordered perovskites, with the B-site cation partially replaced by a M^{3+} or a M^{4+} and a vacancy.

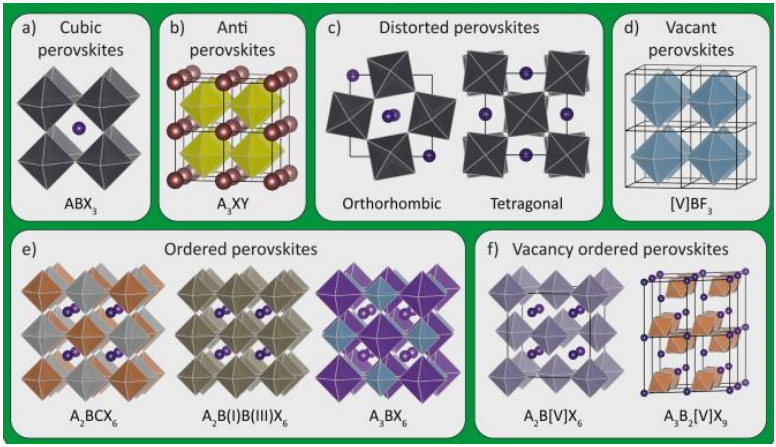

Figure 3 *Overview of the different deviations from the ideal cubic structure in MHPs. a) Cubic perovskite, b) anti-perovskites, c) distorted perovskites, d) vacant perovskites, e) ordered perovskites, and f) vacancy ordered perovskites. Reprinted with permission from ref. [8] Copyright © 2020 American Chemical Society.*

1.1.2 Dimensionalities

Actually, MHPs are characterized by different crystal structures related to the way of connection between the B cation coordination octahedra. These possible arrangements generate four dimensionalities of the same perovskite, exhibiting different properties: 3D (Three-Dimensional), 2D (Two-Dimensional), 1D (One-Dimensional) and 0D (Zero-Dimensional) (Figure 4). [10]

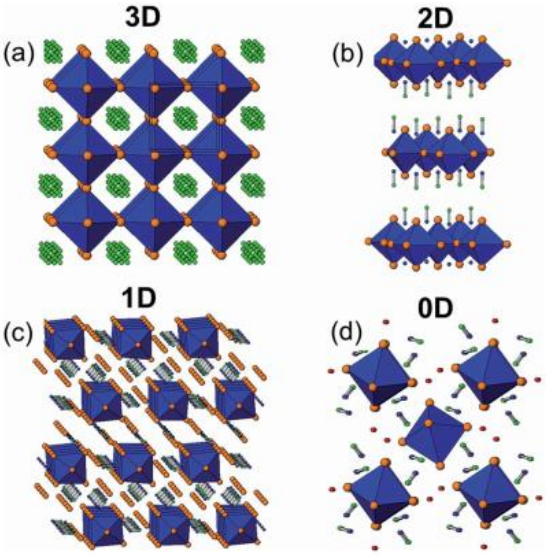

Figure 4 *General representation of crystal structures of a) 3D, b) 2D, c) 1D and d) 0D. Reprinted with permission from ref. [11] Copyright © 2014 Royal Society of Chemistry.*

As mentioned above, 3D perovskites present ABX_3 stoichiometry and are characterized by $[BX_6]^{4-}$ octahedra sharing all the corners, while the A^+ cations fill the voids created by four connected octahedra. Another example of 3D perovskite is the structure named *double perovskite* with $A_2B^+B^{3+}X_6$ formula, simply generated from the replacement of B^{2+} cation with one monovalent and one trivalent cation.

2D perovskites are also defined *layered* perovskites and can show AB_2X_5 stoichiometry made of alternating A^+ ions and $[B_2X_5]^-$ polyhedra, or A_2BX_4 formula in which A^+ cations slabs are alternated with slabs of corner-sharing $[BX_6]^{4-}$ octahedra. Another type of 2D perovskite has $A_3M_2X_9$ stoichiometry, constituted by $[M_2X_9]^{3-}$ isolated clusters made of two face-sharing octahedra with A^+ cations acting as a bridge between the clusters.

Instead, in 1D perovskites each octahedron BX_5 is connected at two opposite corners with its neighbour forming separated endless chains. [11] . In this case the general stoichiometry is A_3BX_5.

Lastly, 0D perovskites can present A_4BX_6 stoichiometry with totally uncoupled $[BX_6]^{4-}$ octahedra and the anions are no longer shared between them; or A_2BX_6 formula in which the unit cell is constituted by four decoupled $[BX_6]^{4-}$ octahedra at the corners and at the faces centre, as well as eight A^+ cations in the interstitials. All the possible types are reported in Figure 5.

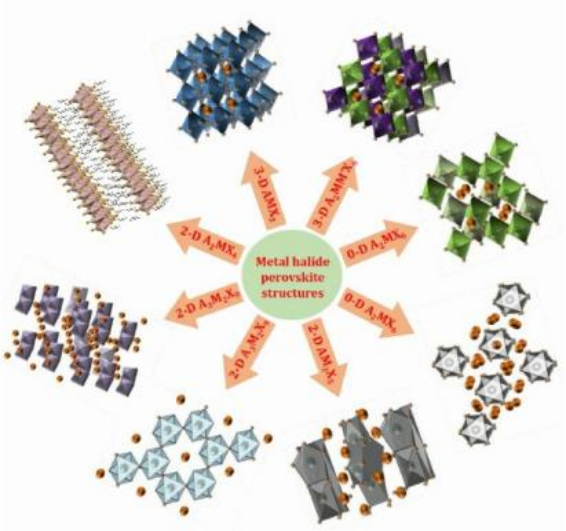

Figure 5 *Schematic representation of different MHPs crystal structures of 3D AMX_3, 3D double perovskite $A_2MM'X_6$, 2D A_2MX_4, 2D $A_3M_2X_9$, 2D AM_2X_5, and 0D A_4MX_6. Reprinted with permission from ref. [8] Copyright © 2020 American Chemical Society.*

1.1.3 Structural stability

The original perovskite structure is quite simple, although several structural modifications may often occur in this class of materials, due to the diversity of ionic radius of the elements included, leading to a slight distortion of the unit cell.

In 1920s Goldschmidt introduced an experimental factor, called *tolerance factor* (*t*), allowing to predict the stability of the perovskite structure. [12] For a perovskite with chemical formula ABX_3, the tolerance factor is described by the following equation:

$$t = \frac{r_A + r_X}{\sqrt{2}(r_B + r_X)}$$

where r_A, r_B and r_X are the two cations and the anion ionic radii, respectively. It considers the ions size the structure can tolerate without giving a phase transition to a more stable structure. The accepted values of *t* range from 0.76 to 1.13 (Figure 6). Higher or lower values of the tolerance factor mean a structural deviation from the ideality. Distortions from the ideal cubic structure can derive from a mismatch due to the different size of cations and anions, from a displacement of B cation from the middle of the octahedra, from ordering of one of the cations, of both the cations or of the anion. The occurrence of these phenomena results in different perovskite structures and non-perovskite constructs. In particular, distorted structures induced by the tilting of octahedra are obtained with a tolerance factor of 0.7 – 0.9, resulting in orthorhombic and rhombohedral derivatives. While a higher or lower tolerance factor gives non-perovskite structures such as hexagonal ($t > 1$) or corundum/ilmenite – type ($t < 0.7$).

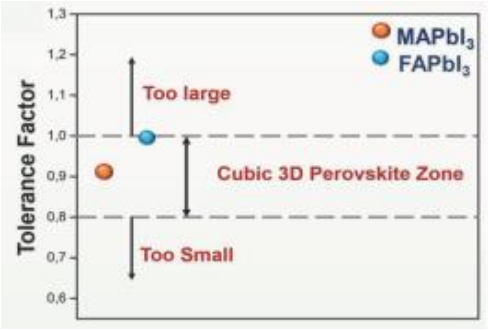

Figure 6 *Tolerance factor for the formation of the ideal cubic perovskite structures. Reprinted with permission from ref. [13] Copyright © 2019 WILEY-VCH Verlag GmbH & Co. KGaA Weinheim.*

The 3D perovskites being more affected by structural instability are the iodide-based compounds, since they show tolerance factors at the limit of the mentioned range: for instance, $FAPbI_3$ (cubic 3D) and $CsPbI_3$ (orthorhombic 3D) give phase transitions to more stable hexagonal and orthorhombic 1D structures (Figure 7). [14]

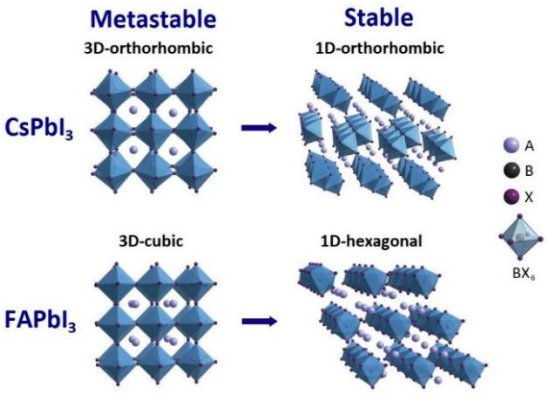

Figure 7 *Phase transition to the more stable structures for iodine-based 3D perovskites. Reprinted with permission of ref. [14] Copyright © 2017 The American Association for the Advancement of Science.*

Moreover, a subsequent parameter used to prove the perovskite structural stability is the *octahedral factor* (μ) which describes the [BX_6] octahedra stability: [15]

$$\mu = \frac{r_B}{r_X}$$

where r_B and r_X are the radii of the respective ions. The range of μ varies from 0.44 to 0.895.

These two factors are exploited to predict the stability even for low-dimensional perovskites. In particular, the *t*-value threshold can be relaxed if the compound under examination is expected to crystallize in the 2D structure rather than the 3D one. [16] The probable reason of this phenomenon is that the strain accumulation induced by the larger A-cation is compensated by separating flexible organic slabs. The spacer cations play a role of buffers reducing the compression caused on the inorganic layers. [17]

1.2 2D layered perovskites

In the last few decades, hybrid organic-inorganic halide perovskites have become one of the most promising classes of semiconductor materials for their high performance in optoelectronic devices. Besides the thoroughly investigated 3D systems, next generation of MHPs is represented by perovskites with a reduced dimensionality, in particular the 2D materials, which seem to exhibit excellent photo-physical properties. [18]

One of the crucial issues of MHP is the sensitivity of all these materials to moisture. Nevertheless, it is believed that a partial solution to the reduced stability of 3D compounds could reside in the reduction of structural dimensionality. The increased stability of low-dimensional perovskites seems due to a structure in which inorganic octahedra are probably more shielded by the organic members. These spacers act as protective layers allowing to prevent the rapid oxygen absorption and thus delaying the

decomposition of materials. The second reason of the increasing interest towards 2D perovskites is the chemical tunability of their structural and optical properties, through the modulation of the nature of the organic spacer. [3]

2D perovskites can be divided in different structures on the basis of the crystallographic planes where the organic spacers separate the inorganic octahedra, resulting in ⟨100⟩-oriented, ⟨110⟩-oriented, and ⟨111⟩-oriented 2D materials. The most investigated are the ⟨100⟩-oriented perovskites, which can be further categorized into the following phases (Figure 8):

- Ruddlesden-Popper (RP) phase, with formula $A'_2A_{n-1}M_nX_{3n+1}$ where both A (smaller) and A' (larger) are monovalent organic cations, presents staggered layer stacking. It consists of two interlayer organic spacers sheets, each interacting with inorganic layers only at one side, while on the other end of the chain they interrelate each other through van der Waals forces. [19]

- Dion-Jacobson (DJ) phase, with stoichiometry $A'A_{n-1}M_nX_{3n+1}$ where A is a smaller monovalent organic cation and A' is a larger divalent organic cation, show eclipsed layer stacking. In this case, using a diammonium cation, ammonium groups at both the ends of the organic chain can interact with the inorganic slabs forming hydrogen bonds. [20]

- Alternating cations in the interlayer space (ACI) phase, with formula $A'A_nM_nX_{3n+1}$ where both A and A' are small monovalent organic cations, and staggered layer stacking along the *b* direction, while eclipsed along the *a*-axis. In this case, the A-site cation (such as methylammonium) is not only in the octahedral cage but it is also present between the inorganic layers alternating with the other larger cation. For this reason, the ACI structure can be templated only by the guanidinium cation as A'. [21]

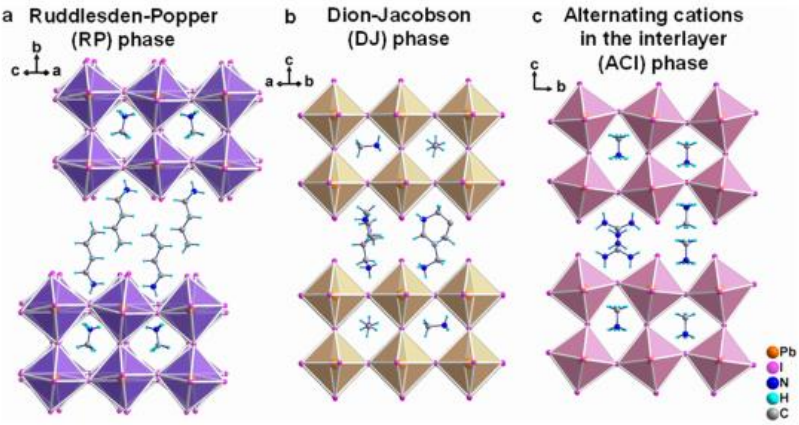

Figure 8 *Structures of ⟨100⟩-oriented 2D perovskites. a) Ruddlesden – Popper (RP) phase, b) Dion – Jacobson (DJ) phase, c) Alternating cations in the interlayer (ACI) phase. Reprinted with permission from ref. [6] Copyright © 2021 American Chemical Society.*

The A cations may be fully or partially replaced by the larger A' cations, resulting in structures with a single inorganic layer (n = 1) or more adjacent inorganic slabs (n = 2, 3, 4, etc. They undergo the definition of *quasi-2D* perovskites). n = ∞ corresponds to the 3D perovskite (Figure 9). Sorting the number of inorganic layers, properties of these materials can be modulated, accordingly. The exact n-layer thickness can be tailored through a simple synthetic chemical route, allowing to tune the quantum-confinement effects. Up to date, the highest number of layers which has been characterized in a 2D perovskite is n = 7. With n > 7 the unit cell becomes too large preventing the full characterization of these materials, since the intergrowth of various phases reduces the crystallinity. [6]

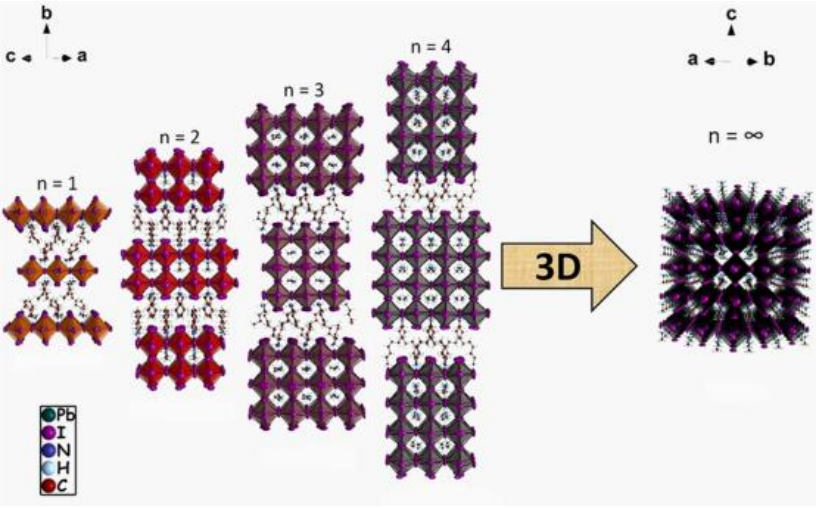

Figure 9 *Crystal structures of 2D perovskites extending from n = 1 to n = ∞. Reprinted with permission from ref. [19] Copyright © 2016 American Chemical Society.*

1.2.1 Organic spacer cations

The selection of the organic spacer should be made considering all any possible factors that could stabilize the 2D perovskite, such as size, shape, charge, and presence of heteroatoms. The ⟨100⟩-oriented 2D structure allows the incorporation of a plethora of organic cations, actually acting as a template to build the perovskite itself up. The different kind of organic spacers can affect the distortion both within and between the inorganic octahedra, tune the exciton binding energy and improve the stability by controlling the hydrophobic chain. [4]

One of the fundamental aspects that should be taken into account in the choice of the spacer cation is its nature and therefore its shape, considering the characteristics of the organic tail and the amino head. The first one can be linear, branched or cyclic, also differentiating between aliphatic and aromatic molecules. Obviously, linear-chain cations are more flexible and

can easily give the 2D motif. [22] On the contrary, a more complexity of the chain induces a higher rigidity of the spacer, reducing its freedom to move, especially due to increasing steric hindrance in branched cations and stiffness of the ring in aromatic spacers; therefore, tilting and formation of hydrogen bonds with inorganic slabs are consequently hindered. [23] As concerns the aminic group at the end of the chain, it needs to show the suitable size to penetrate through the inorganic layer reaching the terminal halides. For this reason, the formation of 2D structure is more favoured by primary ammonium cations, followed by secondary, then tertiary and lastly quaternary ammonium cations: $R\text{-}NH_3^+ > R_2NH_2^+ > R_3NH^+ > R_4N^+$. In particular, the presence of bulky groups as substituents on the N atom may destabilize the 2D structure. [24]

The size of the whole spacer is essential to discriminate between 2D and the other perovskite structures. The smallest monoammonium cation reported in literature, recognized as able to generate the 2D motif, is methylhydrazinium. [25] Compounds with linear monoammonium chains with up to 18 carbon atoms have been investigated, constantly resulting in 2D structures. [22,26,27] While, among linear diammonium cations, the shortest spacer that can be used is 1,4-butanediammonium. [28] Instead, for cyclic spacers, monoammonium cations with different carbon atoms number in the ring have been studied, obtaining 2D structures only from three to six carbon atoms. [29,30] A bigger size of the ring, as well as the presence of too numerous rings in the spacer, may destabilize the 2D perovskite structure.

Another important aspect to take into account is the formation of hydrogen bonds between the organic spacer and the inorganic slabs, which play a key role in the stabilization of the 2D structure. The variation in the type of the spacer can change the strength of hydrogen bonds, significantly affecting structural and thus functional properties of materials. In particular, when heteroatoms are present in the organic spacer, new hydrogen bonds may occur and this could modify the cation configuration, sometimes providing a displacement of the unit cell. [31] Figure 10 shows an overview of the organic spacers that have been employed in literature for 2D perovskites.

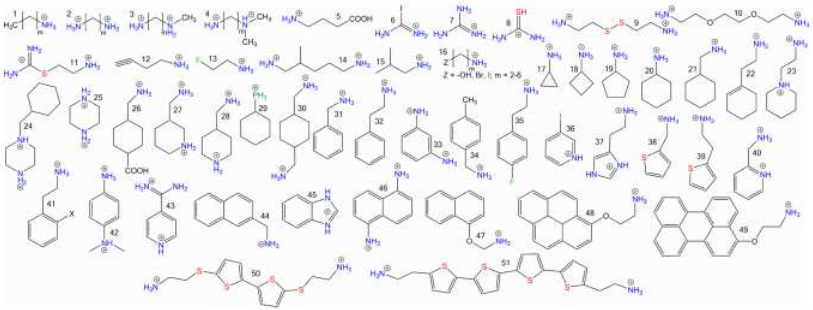

Figure 10 *Reported organic cations used to template 2D perovskites.* ***1)*** *primary alkylammonium (m = 0-1),* ***2)*** *primary alkyldiammonium (m = 3-12),* ***3)*** *N^1-methylethane-1,2-diammonium (N-MEDA) (m = 2), N^1-methylpropane-1,3-diammonium (N-MPDA) (m = 3),* ***4)*** *2-(dimethylamino)ethylammonium (DMEN) (m = 2), 3-(dimethylamino)-1-propylammonium (DMAPA) (m = 3), 4-(dimethylamino)butylammonium (DMABA) (m = 4),* ***5)*** *ammonium 4-butyric acid,* ***6)*** *iodoformamidinium,* ***7)*** *guanidinium,* ***8)*** *protonated thiourea cation,* ***9)*** *2,2'-dithiodiethanammonium,* ***10)*** *2,2'-(ethylenedioxy)bis(ethylammonium) (EDBE),* ***11)*** *protonated 2-(aminoethyl)isothiourea,* ***12)*** *but-3-yn-1-ammonium (BYA),* ***13)*** *2-fluoroethylammonium,* ***14)*** *2-methylpentane-1,5-diammonium,* ***15)*** *isobutylammonium (IBA),* ***16)*** *heteroatom-substituted alkylammonium,* ***17-20)*** *cyclopropylammonium, cyclobutylammonium, cyclopentylammonium, and cyclohexylammonium,* ***21)*** *cyclohexylmethylammonium,* ***22)*** *2-(1-cyclohexenyl)ethylammonium,* ***23)*** *N-(aminoethyl)piperidinium,* ***24)*** *N-benzylpiperazinium,* ***25)*** *piperazinium* ***26)*** *(carboxy)cyclohexylmethylammonium,* ***27)*** *3-(aminomethyl)piperidinium (3AMP),* ***28)*** *4-(aminomethyl)- piperidinium (4AMP),* ***29)*** *cyclohexylphosphonium,* ***30)*** *1,4-bis(aminomethyl)cyclohexane,* ***31)*** *benzylammonium (BZA),* ***32)*** *phenylethylammonium (PEA),* ***33)*** *m-phenylenediammonium,* ***34)*** *4-methylbenzylammonium,* ***35)*** *4-fluorophenylethylammonium,* ***36)*** *3-iodopyridinium,* ***37)*** *histammonium,* ***38)*** *2-thienylmethylammonium,* ***39)*** *2-(2-thienyl)ethanaminium,* ***40)*** *2-(ammoniomethyl)pyridinium,* ***41)*** *2-substituted phenethylammonium (X = F, Cl, Br),* ***42)*** *N,N-dimethyl-p-phenylenediammonium,* ***43)*** *4-amidinopyridinium,* ***44)*** *2-naphthylmethylammonium,* ***45)*** *benzimidazolium,* ***46)*** *1,5-diammoniumnaphthalene,* ***47-49)*** *naphthalene-O-ethylammonium, pyrene-O-ethylammonium, perylene-O-ethylammonium,* ***50)*** *5,5'-bis(ammoniumethylsulfanyl)-2,2'-bithiophene (BAESBT),* ***51)*** *5,5'''-bis(aminoethyl)-2,2':5',2'':5'',2'''-quaterthiophene (AEQT). Reprinted with permission from ref. [6] Copyright © 2021 American Chemical Society.*

1.2.2 Optoelectronic properties and applications

MHPs have attracted increasing interest in the scientific community thanks to their excellent properties in terms of light absorption coefficient, photoluminescence quantum yield, long charge carrier lifetime, diffusion

length, tunable band gap, excitonic binding energy, and defect tolerance. These properties made them suitable for application in photonic and electronic devices.

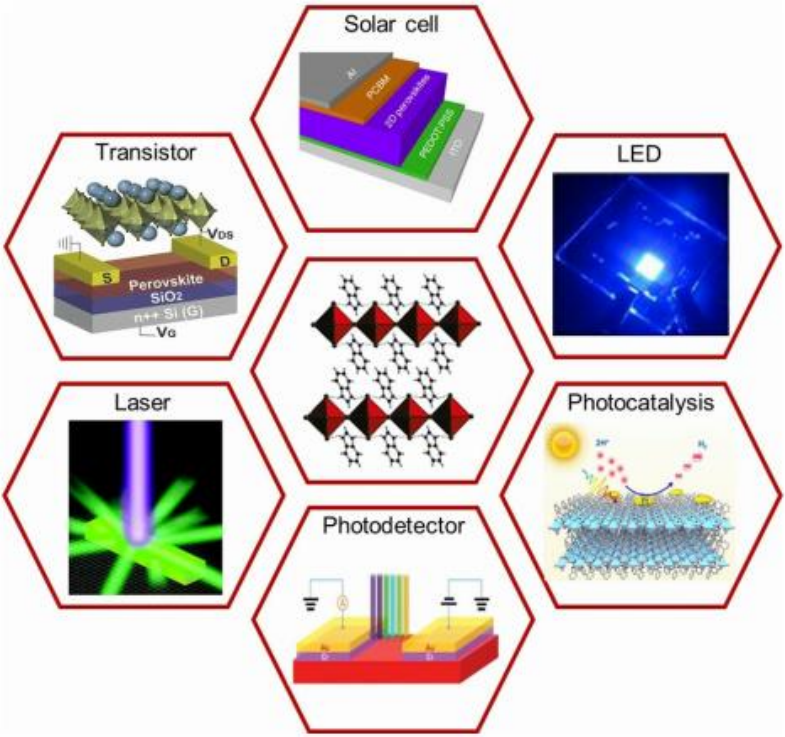

Figure 11 *Illustration of optoelectronic applications of 2D MHPs. Reprinted with permission of ref. [32] Copyright © 2021 Wiley-VCH GmbH.*

In the past few years, important improvement was especially achieved by solar cells based on 3D perovskites, despite the crucial issue of their instability. The introduction of 2D materials may represent a possible solution to this problem, since layered materials show a more pronounced tolerance to moisture, humidity, and water due to their particular structure. Their hydrophobic nature, derived from the presence of organic chains,

makes them appropriate candidates also for photocatalytic applications. Moreover, their binding energy and photoluminescence efficiency are significantly enhanced by the important quantum confinement in 2D perovskites with respect to 3D materials, allowing their application in LEDs and laser devices (Figure 11). [5]

Electronic structure

2D MHPs have a band gap based on the overlapping degree of the metal-halogen bonds, similar to the case of 3D perovskites. The overlapping of *s* orbital of metal ion and *p* orbitals of halide ions forms antibonding hybrid states, that constitute the valence band maximum (VBM). Whereas, the conduction band minimum (CBM) consists of antibonding states formed by the overlapping of mixed *p* orbitals of metal ion and halide ions. A spin-orbit splitting of *p* orbitals of the metal ion gives a further stabilization of the CBM and may be the reason of the defect tolerance of these materials. Despite wide bands observed in 3D MHPs, the valence and the conduction bands include localized narrow bands in 2D perovskites, probably as a consequence of Jahn-Teller effect and the zero-dispersion along the vertical axis. For this reason, higher bandgaps and exciton binding energies are shown in 2D materials with respect to the corresponding 3D compounds. Indeed, 2D perovskites are excitonic semiconductors with bandgap energies typically above 2.5 eV and exciton binding energies exceeding 300 meV, resulting in quantum and dielectric confinement effects. [33]
As mentioned before, the nature of the organic cation deeply influences the structural and optoelectronic characteristics in these compounds, including the band gap. Indeed, the electronic properties are determined by the band alignment of the organic spacer with the inorganic slabs. In general, the bandgap of the organic layer is higher than the one of the inorganic layers, creating a quantum well-barrier structure, in which the inorganic layers act as potential wells while the organic components as potential barriers (Figure 12). [13]

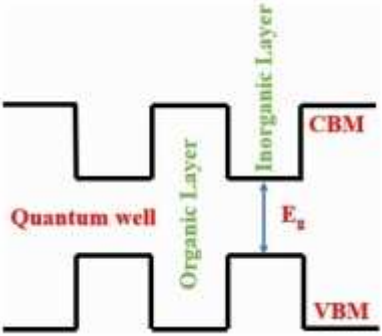

Figure 12 *Schematic representation of quantum well structure of a 2D perovskite. Reprinted with permission from ref. [13] Copyright © 2019 WILEY-VCH Verlag GmbH & Co. KGaA Weinheim.*

Applications

2D materials revealed several advantages compared to the corresponding 3D perovskites. The alternating organic and inorganic layers make 2D perovskites appealing for unique properties they confer them. Modifying the number of inorganic slabs (n = 1, 2, 3, 4, …) optoelectronic characteristics such as quantum confinement, charge carrier recombination, etc. can be easily tailored. One of these features is the dielectric confinement along the *c*-axis deriving from the difference in the dielectric constants, lower for the organic sheet and higher for the inorganic layer. Thanks to all these assets, 2D perovskites seem to be excellent candidates for LEDs applications. Furthermore, the hydrophobic nature of organic spacers can provide a remarkable stability to the perovskite under ambient conditions, making it suitable also for photocatalytic applications, as well as accounting for the larger surface area due to the low dimensionality. Another positive aspect, related to the reduced dimensionality is the poor dark current in devices, since the halide ions migration in 2D MHPs can be considered negligible. [34] Due to the high exciton binding energy and quantum confinement, 2D MHPs present high photoluminescence quantum yield, appealing for LED

application. In particular, the increase of number of inorganic layers improves the charge carrier concentration, the mobility and the quantum efficiency. [32] The utilization in photodetectors is favoured by the anisotropic charge carrier properties due to the quantum well structure, which makes the exciton diffusion easier through the inorganic layers, resulting in a better dissociation of excitons into free carries and, thus, improved efficiency of the device. [35]

However, besides these indisputable advantages of 2D perovskites, many drawbacks limit their optoelectronic application especially in photovoltaic, photodetector, and photocatalytic applications. For instance, the larger bandgap of the pure 2D perovskites (which is > 2.3 eV) is not so suitable for photovoltaic application. [13] The solution to face this drawback consists of mixing 2D perovskites with 3D materials, in order to decrease optical bandgap and exciton binding energy, to enhance the efficiency and to improve the stability due to the 2D perovskite hydrophobicity induced by the organic spacer. [36] Another problem concerns the high exciton binding energy caused by the reduced dimensionality, that confines the excitons within the inorganic layers, resulting in very low charge carriers separation. This inconvenience could be rectified by increasing the number of inorganic layers. [37] Indeed, 2D perovskites exhibiting the poorest optoelectronic features are the n = 1, due to the more prominent electro-phonon interaction observed because of the high portion of organic components with respect to the inorganic moiety. Secondly, high exciton binding energies and enhanced electron-hole interactions lead to non-radiative recombination processes of some excitons, limiting devices performance. [38] On the contrary, quasi-2D MHPs exhibit excellent electronic peculiarities, making them suitable for devices reported in Figure 11. Also, tuning the dielectric confinement by using spacer cations with higher dielectric constant can reduce the dielectric difference between the inorganic and organic layers, lowering the exciton binding energy, and making 2D perovskites more appropriate materials for this kind of applications, up to date an exclusive prerogative of 3D systems. [39]

1.2.3 White-light emitters

Broadband emitters are single-phase compounds able to emit photoluminescence (PL) covering almost the whole visible spectrum and generating white light. These materials are quite rare but they represent the next generation of solid-state phosphors, substituting the current method of white light production by mixing different phosphors of LEDs.
Interestingly, broadband white-light emission has been observed in 2D MHPs, making them desirable materials for this kind of application. First examples of 2D white emitters have been reported by *Smith et al.* in 2014 investigating (N-MEDA)$PbBr_4$ and (EDBE)PbX_4 (*N*-MEDA = N^1-methylethane-1,2-diammonium, EDBE = 2,2′-(ethylenedioxy)bis(ethylammonium), X = Cl and Br) (Figure 13). [40] Later, new 2D perovskite phases have been studied as broadband emitters in order to explain the emission mechanism, also as a function of temperature.

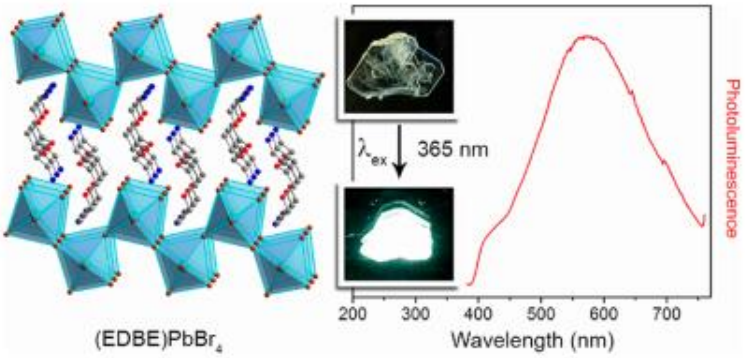

Figure 13 *Structure of (EDBE)$PbBr_4$ and its emission which cover the entire visible spectrum. Reprinted with permission from ref. [40] Copyright © 2018 American Chemical Society.*

High exciton binding energy of 2D perovskites provides a strong PL at room temperature. These fascinating results have prompted the study of these materials even at low temperature, obtaining in some cases a combination of narrow and broad emissions, probably as a consequence of self-trapping;

an important dependence of emission on the temperature was thus demonstrated. [40]

The exciton self-trapping is the proposed mechanism at the origin of broad PL, with a further enlargement induced by the presence of defects in the material. Self-trapped excitons occur in materials presenting soft lattice and electron-phonon interactions strong enough to cause elastic distortions in the lattice by excited electrons and holes. After the photogeneration of electrons and holes, they are quickly self-trapped in order to reach a more stable state with respect to the former condition, in which they can move, increasing the lattice distortion. This phenomenon provides the emission of photons with broad spectrum and significant Stokes shift from the absorption curve (Figure 14). [41]

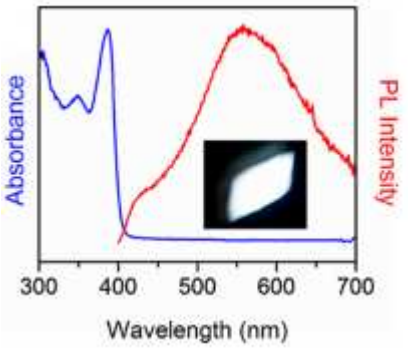

Figure 14 *Absorption and photoluminescence spectra of (N-MEDA)$PbBr_4$. It can be noted a significant Stokes shift between the narrow absorption curve and the broad PL spectrum. The inset shows the photograph of PL from the powder. Reprinted with permission from ref. [40] Copyright © 2018 American Chemical Society.*

The color of the broad PL can be tuned by substituting the halide (Br/Cl) in the perovskite, allowing to obtain both cold and warm white light. The partial chloride substitution in a 2D bromide perovskite affects two parameters: the first one is the emission colour-rendering index (CRI), quantifying the ability of a light source to reflect the true colour of an

illuminated sample. It increases along with the Cl amount. Commercial indoor illumination phosphors are required to have a CRI value > 80. For instance, (EDBE)$PbBr_4$ possesses a CRI = 84. The second parameter is termed CIE (chromaticity coordinates, CIE_x and CIE_y) and defines the colour of the broad emission. The progressive replacement of bromide with chloride shifts the CIE values even closer to the pure white light, near to the sunlight. An example of CIE diagram is reported in Figure 15. [42]

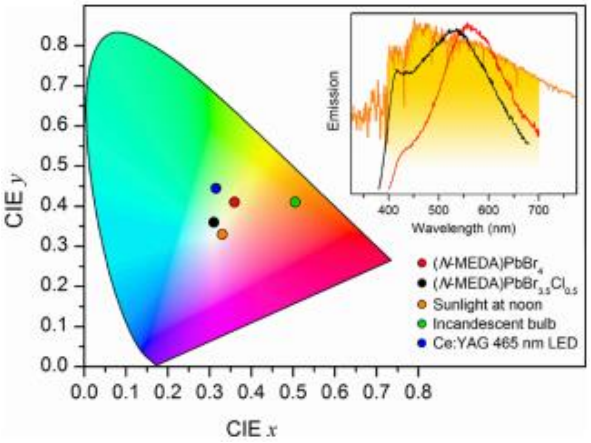

Figure 15 *Chromaticity coordinate diagram for some white-light emitters. In the inset: solar spectrum (orange) with the visible region shaded in yellow and the emission spectra of (N-MEDA)$PbBr_4$ (red) and (N-MEDA)$PbBr_{3.5}Cl_{0.5}$. Reprinted with permission from ref. [42] Copyright © 2014 American Chemical Society.*

1.3 *Lead-free* materials

The most deeply investigated MHPs systems are based on Pb^{2+} as B cation, since this metal provides perovskites with the best functional properties in terms of good stability, despite all perovskite materials are sensitive to moisture, and high devices performance. Therefore, struggling with the toxicity issues of lead-containing systems, researchers on MHPs are now significantly enlarging the panorama of possible metals (e.g., Sn, Bi, Sb, Ge), with Sn as the major player in this novel sustainable future. [43,44] The commercialization of lead-based devices is limited by this metal's toxicity, probable carcinogenicity, bioavailability and water solubility that might causes water contamination, representing a potential risk for both humans and environment. [45]

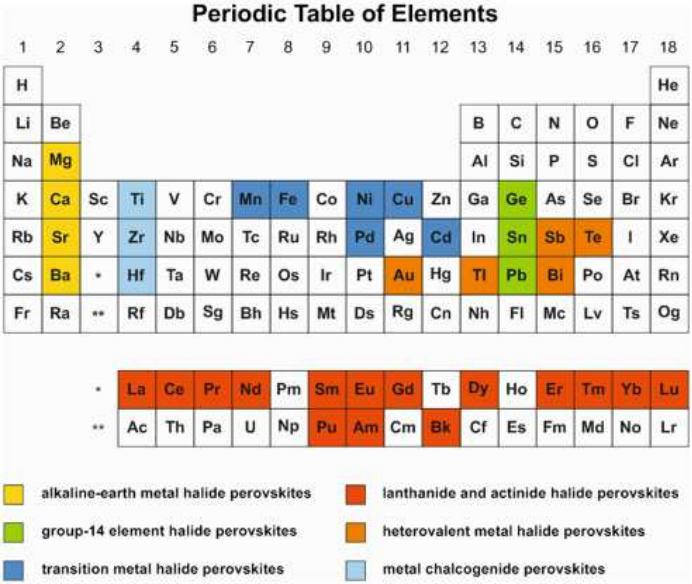

Figure 16 *Periodic table of the elements in which candidates for lead replacement are highlighted. Reprinted with permission from ref. [45] Copyright © 2017 Springer Nature.*

Figure 16 shows all the possible candidates for lead replacement in the periodic table of the elements. The substitution can be achieved through two approaches:

- a homovalent substitution with 14th-group elements (Ge^{2+}, Sn^{2+}), alkaline-earth metals (Mg^{2+}, Ca^{2+}, Sr^{2+}, Ba^{2+}), transition metals (Cu^{2+}, Fe^{2+}, Pd^{2+}), and lanthanides and actinides (Eu^{2+}, Tm^{2+}, Yb^{2+});

- or a heterovalent substitution with a combination of aliovalent cations with the aim to maintain the neutral charge balance. For instance, transition metals such as Au, main group elements (Tl, Sb, Bi, Te), lanthanides (La, Ce, Pr, Nd, Sm, Eu, Gd, Dy, Er, Tm, Lu), and actinides (Pu, Am, Bk) with a different oxidation state from the bivalent one.

1.3.1 Germanium as B cation

Ge-containing perovskites still deserve a deep investigation, starting from the basic science point of view, to further exploit their possible functionalities which could extend to a rich range of fields, in analogy with Pb-and Sn-based systems. While sharing with tin some issues related to cation oxidation, Ge appears to be more stable, and a proper materials chemistry design based on metal alloying and organic cation tailoring could improve the stability of germanium halide perovskites. Other issues to overcome, shared with Bi- and Sb-perovskites, are the poor solubilities in common polar organic solvents of germanium precursors, but the advancement in the field of physical vapor deposition of MHPs could provide the required answer. [46] Exploration of lower-dimensional systems is still at infancy and the exciting results accumulated in the last years on tin and lead analogues should trigger a significant amount of experimental and computational research to unveil the structure-property correlations in these systems. Lower-dimensional Ge-based perovskites in addition to RP

materials still call for a significant experimental and computational investigation to highlight the role of spacer cation, structural distortion, alloying and quantum confinement on optical properties. Another strategy that could be explored for Ge-based materials is the preparation of perovskite derivative materials including Ge^{4+} cations, thus getting rid of the oxidation issues. This approach has been successfully applied for Sn-based perovskites where Cs_2SnX_6 vacancy-ordered inorganic double perovskite proved to be promising phases for photovoltaics and optoelectronic properties. [47,48] To date, only the computational investigation of possible Ge-based vacancy ordered perovskites has been accomplished and urgent experimental effort should be directed in this way. [49]

3D Ge perovskites

Germanium-based MHPs are still scarcely investigated but we may anticipate a growing interest towards such materials in the next years for a wide spectrum of applications. Hybrid organic-inorganic 3D germanium halide perovskites have been among the first to be deeply investigated in analogy with the Pb-containing materials. Initially, a series of $AGeI_3$ materials with A = methylammonium (MA), formamidinium (FO), acetamidinium (MFO), guanidinium, trimethylammonium, and isopropylammonium, was reported in 2015 by Stoumpos *et al.* [50] Only with the first three organic cations 3D perovskites were crystallized while, in the remaining cases, 1D infinite chains compounds were found, as also observed in analogous Pb-containing systems when the size of the organic cation increases. [51] For the 3D perovskite materials, the band gap has been shown to increase progressively by 0.3 eV by replacing smaller Cs^+ cation with bigger MA (1.9 eV), FO (2.2 eV), and MFO (2.5 eV) cations. [50] This is a quite unusual trend since the organic cation size in Pb-based 3D perovskite only marginally affects the band gap. The increased spatial separation of the $[GeI_3]$ inorganic units induced by cation size is believed to be responsible for a reduced orbital overlap. This in turn results in narrow

bandwidths leading to a greater band separation and band gap increase. [50]

More recently, the $MA_{1-x}FA_xGeI_3$ (x =0, 0.25, 0.5, 0.75, 1) solid solution was systematically investigated by *Yue et al*. [52] The optical properties characterization showed a progressive modulation of the band, spanning the interval from 2.26 to 1.98 eV. Interestingly, the analogous Pb-based system, namely $MA_{1-x}FA_xPbI_3$, shows a very limited variation of the band gap moving from $MAPbI_3$ (1.48 eV) to $FAPbI_3$ (1.53 eV). [53] A clear definition of the stronger impact of the organic cation on Ge-based perovskites with respect to the Pb-analogues warrant further detailed structural investigation, e.g. by local structural probes, since this large effect may be exploited for electronic properties tuning as an additional degree of freedom with respect to halide substitution. [54,55] The authors carried out also a deep study on the stability of the prepared phase by performing XRD analysis as a function of exposure time of the perovskite under glove-box conditions and air. In general, while a good stability under argon storage has been found, air-exposure leads to GeO_2 formation after 24 hours, thus confirming the instability of the Ge^{2+} ion toward oxidation to Ge^{4+}. [52]

In parallel to these limited experimental works, advanced computational modelling has been used to explore the electronic and optical properties of Ge-containing perovskites, define their stability, and predict possible novel compositions. Structures and formation energies, electronic band-structures, and optical properties were calculated in great detail indicating, as main conclusions, that $MAGeI_3$ exhibits an electronic character close to the one of $MAPbI_3$ and that Ge-based perovskites are less prone to oxidation with respect to the Sn counterparts providing the following order of stability $MAPbI_3 > MAGeI_3 > MASnI_3$. [56]

As for other 3D MHPs, B-site metal alloying has been explored also for Ge-based perovskites. A detailed experimental study on the $MASn_{1-x}Ge_xI_3$ ($0 \leq x \leq 1$) solid solution has been provided by Nagane *et al*. based also on the computational prediction of the possibility of realizing mixed Sn-Ge perovskites. [57,58]

All-inorganic $CsGeX_3$ (X=Cl, Br, I) have been as well object of several computational works, which highlighted strong absorption coefficients, large dielectric constants, small effective masses, non-linear optical behaviour, strong ferroelectric polarization, and even ultralow thermal conductivities of interest for thermoelectric applications. [56,59–62] Despite this significant amount of computational and theoretical work on $CsGeX_3$ perovskites, few experimental works have been reported in the current literature. Among them, $CsGeX_3$ (X = Cl, Br) perovskites were investigated by Schwarz and co-workers also highlighting the effect of the application of high-pressure on the structural and electronic properties. [63,64] Quite impressively, the band gap of both perovskites has an extremely large reduction (red-shift) by increasing pressure with a rate, of –0.61 eV/GPa. [65] An analogous behaviour has been observed in Sn-based perovskites, while for Pb analogues the impact of high-pressure on the band gap is usually smaller. [66–68]

Low-dimensional Ge perovskites

Together with 3D metal halide perovskite, some limited research efforts were directed towards low-dimensional perovskites, especially 0D and 2D systems. Chang and co-workers investigated the Ruddlesden-Popper series $BA_2MA_{n-1}Ge_nBr_{3n+1}$ derived by layering the parent 3D perovskite $MAGeBr_3$ (with butylammonium $BA=CH_3(CH_2)_3NH_3^+$ and methylammonium $MA=CH_3NH_3^+$). [69] Analogously to the Pb-counterparts, the crystal structure of these materials consists of the stacking of n inorganic perovskite layers, intercalated with bulky butylammonium cations acting as spacers. The authors focused on the *n* = 1 and 2 of this series with the aim of highlighting the quantum confinement effects and comparing their properties with $MAGeBr_3$. The band gaps extracted from the Tauc plots of absorption demonstrate a progressive blue-shift moving from $MAGeBr_3$ (2.85 eV) to BA_2GeBr_4 (2.95 eV), and to $BA_2MAGe_2Br_7$ (2.98 eV), as expected from increased quantum confinement of optical excitations within the layers by reducing n. Through DFT calculations of the electronic structure, the authors attributed the weak dependence of band gap on quantum

confinement to the peculiar nature of the germanium orbitals, leading to band structure of layered RP germanium bromide perovskites similar to the parent 3D perovskite, differently to the case of analogous lead-based compounds. [69]

The PEA_2GeI_4 (PEA=$C_6H_5(CH_2)_2NH_3^+$) 2D perovskite has been reported by Cheng and co-workers as one of the first examples of layered iodide Ge-based perovskite. The authors performed one of the few stability tests available for Ge-based perovskite by comparing $MAGeI_3$ and PEA_2GeI_4 powders exposed to a relative humidity level of 60 % at 25 °C. After 2 days storing in the humidity environment, $MAGeI_3$ showed evident MAI and GeI_4 diffraction peaks in the patterns due to the decomposition and oxidation processes. On the other hand, the pattern of PEA_2GeI_4 remained almost unchanged: this result comes from the hydrophobic nature of PEA cations avoiding the direct contact of water with perovskite, thus delaying the moisture degradation and the subsequent oxidation. [70] The same authors further investigated the mixed Sn-Ge, $PEA_2Ge_{1-x}Sn_xI_4$ system (x = 0, 0.125, 0.25, 0.5). [71]

A variety of further computational works explored other Ruddlesden-Popper Ge-containing perovskites such as the $BA_2MA_{n-1}Ge_nI_{3n+1}$ (n = 2 - 4) systems. By DFT calculations, the trend of electronic and optical properties was predicted showing a band gap decrease from 2.35 eV to 2.29 eV for Ge-based 2D perovskites by increasing the layer thickness from n = 1 to 4, with also a reduction of exciton binding energies and light absorption improvement with increasing layer thickness. [72] Such computational data provide an indication that Ge-based 2D perovskites may be suitable lead-free candidates to be incorporated in photovoltaic and/or photoelectronic devices providing reasonable performance, lower environmental concerns and enhanced device longevity. To date, the number of experimental reports on two-dimensional Ge-containing MHPs is very limited but they appear to be, relying even on the intrinsic distortion observed in the GeX_6 octahedra, good candidates for broadband emitting materials. Moreover, 0D and 1D Ge-based materials appear to be a nearly completely unexplored research field which should be considered in the future.

CHAPTER 2.

2D SINGLE CRYSTALS SYNTHESIS TECHNIQUES

It is noticeable that novel phases of these materials, even if they can be similar to already known 2D structures, need to be investigated by single-crystal X-ray diffraction, because the incorporation of new spacer cations may induce distortions reflecting on differences in physical properties. For instance, the M-X-M bond angle influences the electronic structure, providing a narrower bandgap when the angle is close to 180° and this is ideal for the application in solar cells. The optical properties can be also affected by the interlayer distance and M-X bond length. [73] For these reasons, the structure-property relationship of novel compounds is essential to be studied and the single crystals preparation is required for this purpose.

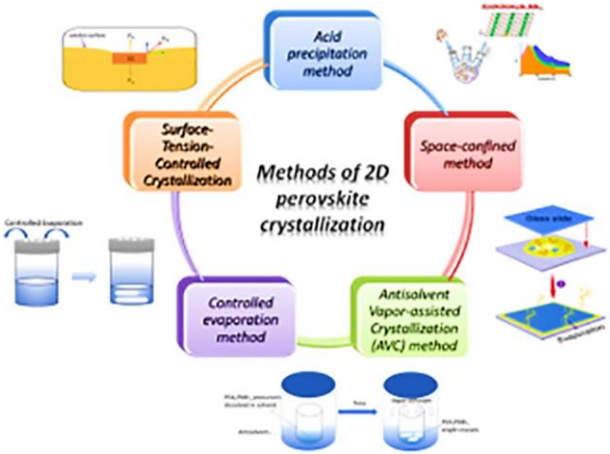

Figure 17 *Schematic representation of the methods to prepare 2D perovskite single crystals. Reprinted with permission from ref. [75] Copyright © 2020 EcoMat.*

It's imperative to find a suitable efficient strategy of synthesis for each material: the first method of MHPs single crystals production was reported in 1987 by Poglitsch and Weber, consisting in a cooling of a HX-based solution. Later, new more advanced methods were introduced, such as a top-seeded solution growth (TSSG), antisolvent-assisted crystalline procedure, an antisolvent vapor-assisted crystallization (AVC) technique, and the inverse temperature crystallization (ITC). [74] Unfortunately, these single crystals preparation strategies were often efficient for 3D perovskites while they failed for 2D materials. In general, the best and most used method to synthetize hybrid 2D perovskite single crystals is the solution process, during which parameters such as solubility, temperature, solvent content, need to be kept under control. Figure 17 shows a schematic representation of the possible crystallization routes.

2.1 Acid precipitation method

This method is based on the increasing solubility of the perovskite along with the temperature in the HX solution, where X = Cl, Br and I. It was described for the first time in 1987 by Poglitsch and Weber for the growth of 3D perovskite single crystals through a cooling method and then extended also to 2D perovskites. [75] By heating the HX perovskite precursor solution up to a temperature > 90°, followed by a slow gradual cooling down to room temperature, single crystals can be grown. The cooling rate needs to be properly monitored in order to obtain high-quality and large single crystals. On the contrary, fast cooling induces the formation of multiple nucleation sites, providing a polycrystalline powder as a final result. An efficient cooling rate is 1°C/h. In the case of n = 1 layered perovskites, single crystals of the right desired phase are easily obtained by this method. Therefore, when n is greater than 1, a mixture of phases may develop, due to the difference of two organic cations solubility in the same solvent. An example is reported by Bakr's group, who prepared $PEA_2PbI_4{\cdot}(MAPbI_3)_{n-1}$ with n = 1, 2, 3 (PEA, phenethylammonium; MA, methylammonium), while for n > 3 they were

not able to obtain the phases of interest, since a mixture of the pure 3D perovskites was formed. [76]

2.2 Space-confined method

This method, also known as *induced peripheral crystallization* (IPC), was proposed by Liu's group for the preparation of PEA_2PbI_4 single crystals. [77] It was designed with a view of limiting the growth in a confined spaced, allowing to exclusively obtain 2D materials.

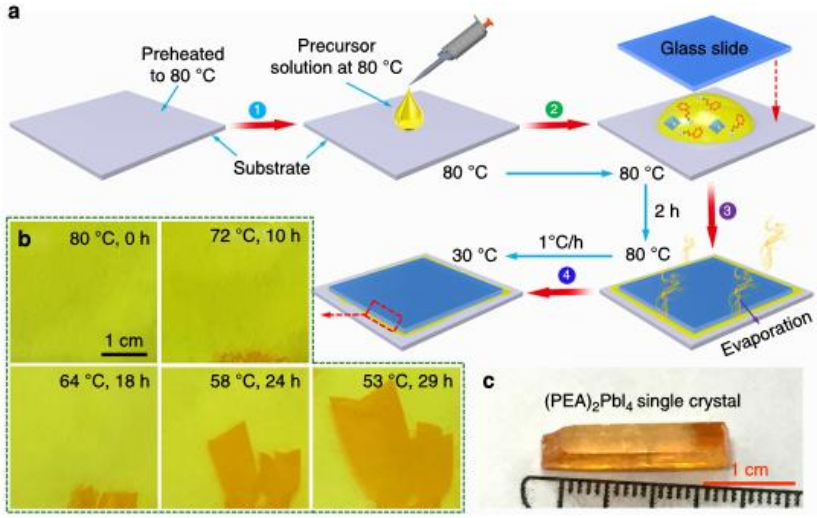

Figure 18 *a) Schematic illustration of IPC method to grow 2D PEA_2PbI_4 single crystals. b) Photographs of PEA_2PbI_4 single crystals at different stages of the growth process. c) Photo of the obtained PEA_2PbI_4 single crystals. Reprinted with permission from ref. [77] Copyright © 2018 Springer Nature.*

A solvent in which the perovskite solubility increases with the temperature, such as γ-butyrolactone (GBL), is required and the apparatus consists of a uniform substrate (like PET, polyethylene terephthalate), a top glass and a

thermostat. The precursor saturated solution is deposited on the preheated substrate (80°C), covered with the top glass and kept at constant temperature. Initially, only the GBL at the edges of the two plates evaporates, while the rest of the solution remains sealed inside by the edge crystals. Reducing the temperature, the perovskite solubility decreases and crystal growth starts at the edge. The cooling rate needs to be controlled in order to avoid the formation of multiple nucleation sites induced by too fast cooling. Figure 18 reports the schematic representation of IPC method and the resulted PEA_2PbI_4 single crystals as a function of slow temperature decrease.

2.3 Antisolvent vapor-assisted crystallization (AVC) method

The AVC method, also called *solvent engineering approach and fast crystallization deposition*, was introduced for 3D materials by Cheng's and Soek's groups and exploits the solubility difference of perovskites in various solvents. [78,79] The perovskite precursors are dissolved in a solvent showing high solubility power, such as N,N-dimethylformamide (DMF), dimethylsufoxide (DMSO) or γ-butyrolactone (GBL) and an antisolvent, such as chlorobenzene, benzene or diethylether, is added in order to crystallize the perovskite. Indeed, when the perovskite nucleates, the antisolvent vapor is continuously transported to the solution, promoting the crystallization. The product size can be tailored by controlling the evaporation rate of the antisolvent. When this latter is too fast, multiple crystal nucleation sites are generated, causing a reduction of the crystal quality or leading to the powder. Instead, a too slow evaporation prolongs the growth process. The first 2D perovskite single crystal obtained through this technique was of PEA_2PbBr_4, prepared by a precursor solution in DMF as a solvent surrounded by an atmosphere of chlorobenzene as an antisolvent (Figure 19). [80]

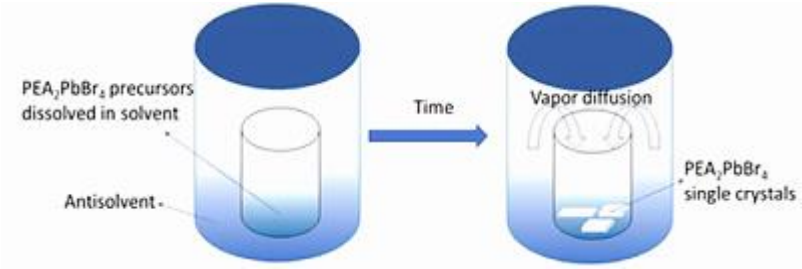

Figure 19 *Schematic representation of the growth process with AVC method of 2D PEA_2PbBr_4 single crystals. Reprinted with permission from ref. [80] Copyright © 2017 American Chemical Society.*

2.4 Controlled-evaporation method

Also known as *slowly evaporating at constant temperature technique*, it's a solution-growth method based on the principle for which the concentration of the solute gradually increases with the solvent evaporation. When the critical saturation concentration is reached, the solute begins to precipitate and its crystallization continues as long as the solvent evaporation goes on. The growth process is divided into two stages: in the first one the solvent evaporates and no crystal formation occurs; in the second stage the crystallization starts because the solution reaches the oversaturation. The first parameter to control is the solvent evaporation rate in order to produce a single nucleation seed; the second one is the growth conditions with the aim to prevent the generation of other nucleation seed. Moreover, the chosen fixed temperature is a fundamental parameter for the success of the crystallization; thus, it needs to be optimized, in order to avoid the formation of a polycrystalline product.

This technique can be used to fabricate single crystals at room temperature, as Liu et *al.* made for PEA_2PbBr_4 first at a fixed temperature of 23°C, after 20 days, from a precursors solution in DMF (Figure 20). [81]

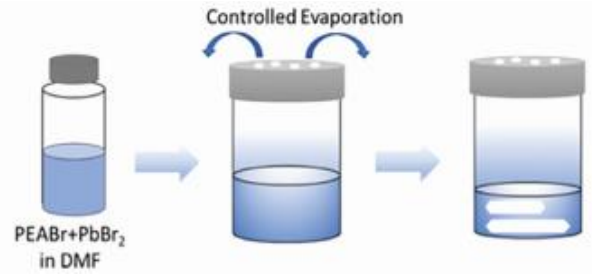

Figure 20 *Schematic diagram of the growth process of PEA_2PbBr_4 single crystals through controlled-evaporation method. Reprinted with permission from ref. [81] Copyright © 2019 Royal Society of Chemistry.*

2.5 Surface-tension-controlled crystallization

This technique is based on the surface tension control, exploiting the difference in the growth rate between the surface of the solution and the interior of the solution. Indeed, the nucleation rate at the surface is found to be higher than the rate in solution. By using the appropriate solvent, the perovskite solubility rises with increasing temperature. With a slow cooling, the solubility gradually decreases, leading to the crystal growth on the surface of the solution due to the rapid transfer to the surface. When the temperature reaches an enough low value, the weight of the crystal becomes excessive and induce its deposition at the bottom of the solution. The resulting crystal will be a large block of regular shape. [82] The authors of ref. 82 have used this method to produce single crystals of PEA_2PbI_4 in γ-butyrolactone with a cooling rate of 0.5°C/h, yielding orange regular crystal blocks as shown in Figure 21.

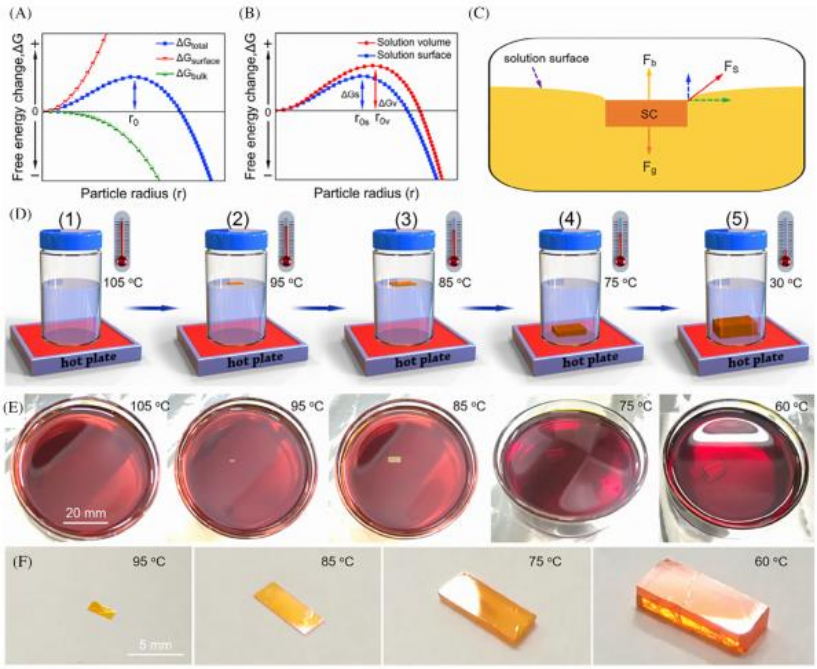

Figure 21 *Crystallization of PEA_2PbI_4 perovskite. A) Gibbs free energy change ΔG_{total} as a function of particle radius. ΔG_{total} consists of a surface term ΔG_s and a bulk term ΔG_b. B) Graph illustrating the lower nucleation barrier for the solution surface with that in the solution volume. C) Schematic of the single crystal staying afloat on the solution surface. D) Schematic of the surface tension-controlled crystallization process. E) Photographs of the PEA_2PbI_4 perovskite single crystals grown at different temperatures. F) Corresponding images of PEA_2PbI_4 single crystals completed at different temperatures. Reprinted with permission from ref. [82] Copyright © 2019 Elsevier.*

CHAPTER 3.

LINEAR ALIPHATIC CHAIN SPACERS

In the last few years there has been a growing interest around 2D MHPs for their superior moisture and air stability, which found application in photovoltaics to design 2D/3D solar cells architectures. [13] Lead-based members with n=1 of the RP family, *i.e*. A_2PbX_4, have been thoroughly studied thanks to the extremely rich variety of organic spacers which can be incorporated into the layered structure giving origin to an impressive modulation of their optical, structural and moisture-resistance properties. [6,18] 2D RP perovskites containing linear monoammonium cations of general formula $(C_nH_{2n+1}NH_3)_2PbX_4$, have been among the first to be explored, even before the advent of MHPs photovoltaics. [22,26,27] These early studies mostly focused on the elucidation of the crystal structure as a function of the number of carbon atoms in the aliphatic chain as well as on the understanding of the phase transition commonly found in these compounds. While the early investigation of the optical properties is quite limited, this important group of publications provides a very accurate and solid structural basis for current research. [22,26,27,83]

Billing reported the crystal structure and phase transition behaviour of the $(C_nH_{2n+1}NH_3)_2PbI_4$ perovskites for $4 \leq n \leq 16$ showing, in general, the presence of multiple reversible phase transitions due to changes in the hydrocarbon chains and the relative arrangement of the inorganic layers. [22,26,27] Some of these compositions, in the form of single crystals, have been also characterized in terms of their optical properties indicating that the photoluminescence (PL) spectra for $4 \leq n \leq 12$ are very similar without providing detailed quantitative data and putting emphasis on the temperature dependence of the optical transitions. [84] More recently, thin films of the $(C_nH_{2n+1}NH_3)_2PbI_4$ family for n=4, 5, 7, 8 and 9 have been characterized by low-temperature PL reporting a variation of the excitonic

structure along with the number of carbon atoms and showing the formation of a fine structure made of three levels for temperatures below 100 K. [85] Recently, the optical properties as a function of the number of carbon atoms in $(C_nH_{2n+1}NH_3)_2PbI_4$ perovskites for $4 \leq n \leq 18$, in the form of thin films, have been reported and the trend of the optical band-gap systematically correlated to structural effects induced by the variation of the chain length on the PbI_6 octahedra. [86]

A limited amount of works has been carried out on the analogous system containing Br instead of I, namely the $(C_nH_{2n+1}NH_3)_2PbBr_4$ perovskites. To the best of our knowledge, only the crystal structure of $(C_4H_9NH_3)_2BrI_4$, together with room-temperature optical properties characterization, has been recently reported. [87] A partial systematic exploration of the effect of hydrocarbon chain length in the $(C_nH_{2n+1}NH_3)_2BrI_4$ systems has been carried out for n=4, 5, 7, and 12, providing a general evidence of the role of n on the excitonic structure. [88]

One of the most appealing aspects of 2D MHPs is their improved air and moisture resistance compared to 3D perovskites. This specific aspect has been considered only in one recent publication where the hydrophobicity of the $(C_{16}H_{33}NH_3)_2PbI_4$ phase has been not only demonstrated by collecting x-ray diffraction (XRD) data before and after water treatment, but also effectively employed in photo-redox catalysis. [89]

3.1 Role of chain length on $(C_nH_{2n+1}NH_3)_2PbX_4$ (n=6, 8, 10, 12, 14, 16; X=Br and I) 2D metal halide perovskites physical properties and hydrophobicity

Purpose and scope

Considering the relevance of 2D MHPs in the current research, particularly for their improved moisture resistance, the lack of systematic and complete

studies of their structural and optical properties, phase transition behaviour, especially for the Br-containing systems, and stability investigation as a function of hydrocarbon chain length, in the present work we address these issues by studying the $(C_nH_{2n+1}NH_3)_2PbX_4$ systems for X=Br, and I and *n*=4, 6, 8, 10, 12, 14 and 16. This work provides the first detailed investigation on the $(C_nH_{2n+1}NH_3)_2PbBr_4$ series and a comparative study of the impact of the number of carbon atoms on two analogous systems characterized by a different halide (Br and I). The results presented below allowed to define a complete picture of the effect of the hydrocarbon chain length on the properties of 2D MHPs containing linear monoammonium cations which can be of relevance to other analogous organic spacers and help in the further design of layered perovskites with tailored properties.

Experimental methods

$(C_nH_{2n+1}NH_3)_2PbX_4$ (X = Br, I) preparation

$(C_nH_{2n+1}NH_3)_2PbBr_4$ powder is prepared by a wet-chemistry route. The followed procedure consisted in the dissolution of a proper amount of Pb(II) acetate powder in a large excess of 48% w/w aqueous HBr. The solution is gradually heated to 100°C under continuous stirring. After the solid dissolution, a stoichiometric amount of the liquid or solid amine is added. Subsequently, the reaction mixture is cooled down to room temperature obtaining the formation of the precipitate. The latter is filtered and dried under vacuum overnight at 65°C.

$(C_nH_{2n+1}NH_3)_2PbI_4$ powder is synthetized by a wet-chemistry route. A stoichiometric amount of Pb(II) acetate powder is dissolved in a large excess of 57% w/w aqueous HI at 100 °C under magnetic stirring. After the solid dissolution, the stoichiometric quantity of the liquid or solid amine is added. Then, the solution is cooled down to room temperature promoting the precipitation of the product. The precipitate is filtered and dried under vacuum overnight at 65°C.

Results and discussion

The room temperature x-ray diffraction (XRD) patterns of the $(C_nH_{2n+1}NH_3)_2PbI_4$ and $(C_nH_{2n+1}NH_3)_2PbBr_4$ systems (*n*= 6, 8, 10, 12, 14 and 16) are reported in Figures 22a and 22b, respectively. The patterns of both series are dominated by the (00*l*) reflections of the long axis typical of the low-dimensional perovskites and related to their plate-like morphology.

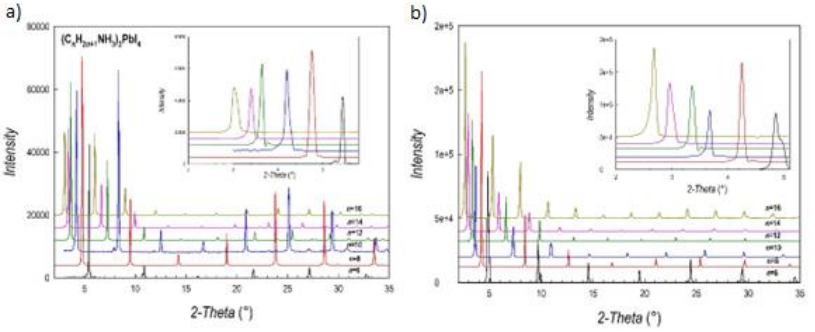

Figure 22 *XRD patterns of (a) $(C_nH_{2n+1}NH_3)_2PbI_4$ and (b) $(C_nH_{2n+1}NH_3)_2PbBr_4$ (n= 6, 8, 10, 12, 14 and 16). Inset: enlargement of low-angle part of the patterns highlighting the first peak.*

The crystal structures of the $(C_nH_{2n+1}NH_3)_2PbI_4$ (*n*= 6, 8, 10, 12, 14 and 16) compositions are known in the current literature and match with the present diffraction patterns of Figure 22a.[1-3] The patterns of the analogous bromide series have been treated through Le Bail method starting from the same crystal structures, providing good fits of the data. From the patterns of Figures 22a and 22b it is evident a progressive shift of the main peaks ((00*l*) reflections) of the patterns to lower angles by increasing the length of the organic ligand, indicating the progressive expansion of the unit cell. The trend of the *c*-axis dimension *vs*. the number of carbon atoms of the amine ligand (*n*= 6, 8, 10, 12, 14 and 16), is reported in Figure 23 for the two series of samples.

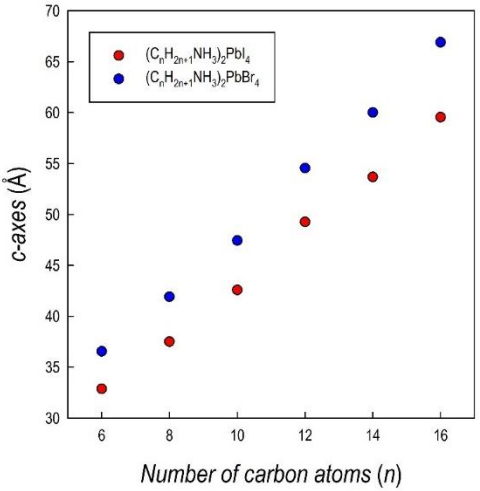

Figure 23 *Trend of the c-axis as a function of the number of carbon atoms of the amine for* $(C_nH_{2n+1}NH_3)_2PbI_4$ *(red dots) and* $(C_nH_{2n+1}NH_3)_2PbBr_4$ *(blue dots).*

The expansion of *c* lattice parameter for both series of 2D perovskites is roughly linear with an increase of the long axis with the number of carbon atoms of about 5 Å in the range $6 \leq n \leq 10$, while a jump of ~7 Å is found in both series when passing from 10 to 12, and then the difference returns to be around 5.5 Å. Such behaviour can be explained based on the room temperature crystal structure as a function of *n*. In the $(C_nH_{2n+1}NH_3)_2PbI_4$ system, for n = 6, 8, and 10, the stable unit cell is the orthorhombic *Pbca*. According to previous works, in this phase (named by Billing *et al*. as Phase II), a bidimensional arrangement of two layers of interdigitated ammonium cations are embedded between two consecutive inorganic $[PbI_6]$ sheets, forming an alternated inorganic–organic layered structure.[3] On the other hand, according to the sequence of phase transition found in these 2D perovskites, when moving to n = 12, the stable phase at RT, still orthorhombic *Pbca*, is Phase III.[1,2] In this case, while the change in the inorganic layer is minimal, there is a change in the tilt angle of the

ammonium group which may account for the observed increase of about ~7 Å.[1-3] As a matter of fact, the transition from Phase II to Phase III leads to an increase, for example in $(C_{10}H_{21}NH_3)_2PbI_4$ of about 1.5 Å. Phase III is then the stable RT arrangement for the *n* = 14 and 16 members of the $(C_nH_{2n+1}NH_3)_2PbI_4$ series, thus further keeping the change in the *c*-axis around 5 Å. Interestingly, such behaviour is also found for the $(C_nH_{2n+1}NH_3)_2PbBr_4$ series where the sequence of phase transitions is analogous to that of the iodide-counterpart even though slightly shifted to lower temperatures, as determined by Differential Scanning Calorimetry. This result will be discussed later when presenting the results of the optical properties of the investigated samples.

Interestingly, the *c*-axis is always longer for the $(C_nH_{2n+1}NH_3)_2PbBr_4$ series, notwithstanding a smaller ionic radius of bromide ion with respect to iodide, and an average size of the inorganic slab of about 6.5 Å for lead iodide perovskites and of about 6 Å for the lead bromides (as determined from the available crystal structures). However, such an effect has been already observed in other series of 2D perovskites where, moving from the iodide to the bromide ion, by keeping the same ligand, leads to an expansion of the long axis (of about 5-6 Å, depending on the amine) as a result of a change in the staggering of the organic cations, which move apart from the halides, thus reducing the tilting of the organic cations. Origin of this effect is mostly related to the strength of the hydrogen bonding of the protonated amine with the apical halides which is well known and discussed in many recent papers.[4-7]

The optical properties of the $(C_nH_{2n+1}NH_3)_2PbBr_4$ and $(C_nH_{2n+1}NH_3)_2PbI_4$ samples have been investigated by UV-Vis absorption and photoluminescence spectroscopies. Figures 24a and 24b report the UV-Vis spectra of the two series, while the Tauc plots, used to extract the bandgap values, are reported in Figure 25.

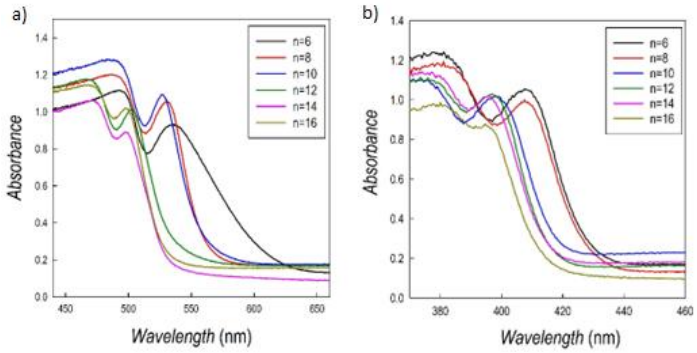

Figure 24 *Absorption spectra for (a) $(C_nH_{2n+1}NH_3)_2PbI_4$ and (b) $(C_nH_{2n+1}NH_3)_2PbBr_4$.*

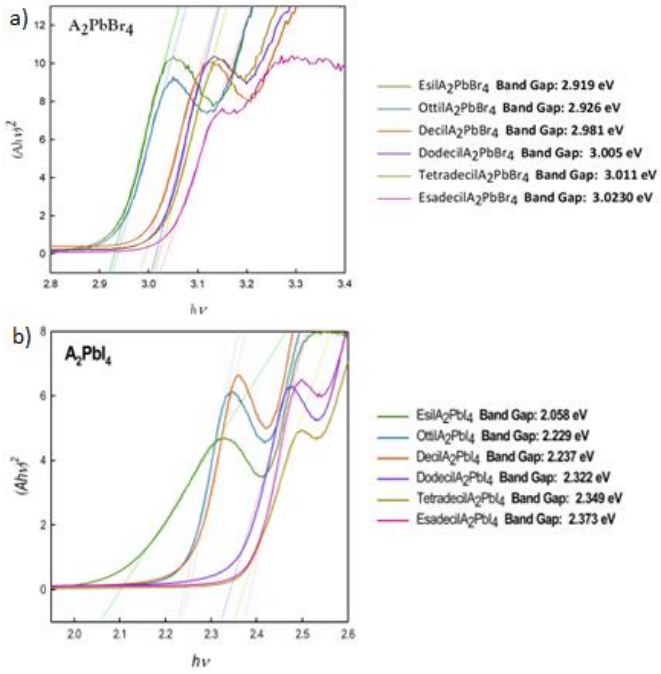

Figure 25 *Tauc Plots and extracted band gap values for a) $(C_nH_{2n+1}NH_3)_2PbBr_4$ series and b) $(C_nH_{2n+1}NH_3)_2PbI_4$ series.*

The spectra are characterized by narrow absorption peaks on top of the band edge, consistent with stable excitonic population, typical of quantum confinement effect.[8] In both cases a general blue shift is observed by increasing the chain length of the organic cation. The corresponding PL spectra are shown in Figures 26a and 26b. The PL spectra well reflect the absorption features, as they show a structured emission involving two main contributions.

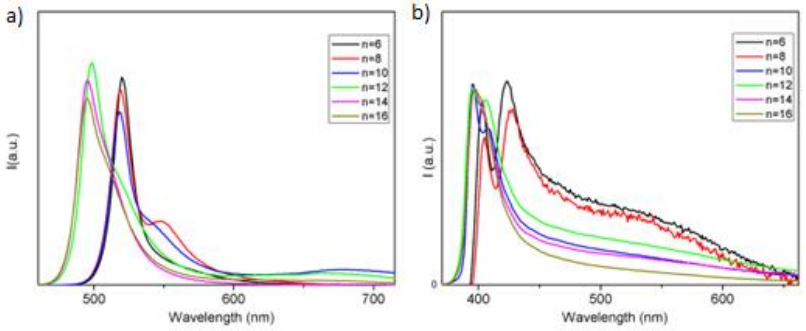

Figure 26 *PL spectra for (a) $(C_nH_{2n+1}NH_3)_2PbI_4$ and (b) $(C_nH_{2n+1}NH_3)_2PbBr_4$.*

The structuring of the 2D MHPs emission in 2 main contributions (S1 and S2) has been debated and, with fluence and temperature experiments, most likely attributed to phonon replica of the main line.[9] Additionally in our samples this band structuring is more evident for the specimens embedding small alkyl chains. As we introduce longer chains, we also observe an abrupt blue shift of the emissions, of about 120 meV for the main peak passing from n=10 to n=12 in iodide samples and about 60 meV moving from n=8 to n=10 in bromide samples. The shift is therefore more pronounced in iodide-based samples. In the past, several studies have shown experimentally and theoretically that, in 2D perovskites, the quantum confinement of the electron and hole and thus the emission wavelength can be tuned by varying the thickness of the inorganic part, so effectively the quantum well thickness.[10,11] It is evident that in our case is not the length of the alkyl chain

variation inducing the abrupt emission blue shift, along the sample series, as this length linearly varies across the series (Figure 23). The transition from Phase II to Phase III in our iodine samples is accompanied to a relatively large abrupt change in the I-Pb-I angle, form around 156° for n $\leq$10 to around 150° for n$\geq$ 12; this, as already observed also by some of us, lead to a decrease of the contributions of Pb orbitals to the CBM and to a band-gap increase and a concomitant blue shift of the PL.[12,13] We prove therefore the reason of the thermochromism observed in these materials, which is induced by a polymorphic transition involving a diverse coordination of the methylammonium cation impacting on the halogen/lead coordination sphere. Very interestingly, these systems possess two distinct variation paths for their excitonic emission behaviour, one directly related the chain length influencing the interplane interaction between inorganic layers, and another one depending on the ammonium coordination to the halogen atoms (polymorphism) with direct dependence on the temperature of the system.

As mentioned in the introduction, a peculiar characteristic of 2D perovskites is their enhanced moisture and even water stability.[14-19] To date, no studies on the effect of the alkyl chain length on such phenomenon has been performed. To address this issue, we subjected three selected members of the $(C_nH_{2n+1}NH_3)_2PbBr_4$ and $(C_nH_{2n+1}NH_3)_2PbI_4$ series, namely with *n* = 6, 10, and 16, to two kind of tests. In the first experiment we put the perovskite powdered sample directly in deionized water and we left it for 4 hours under stirring and recovered the material after this time following water evaporation under the hood. On these samples we collected XRD patterns and compare them to the pristine, as-prepared materials. The second test was the determination of the contact angle by using water as solvent as a function of time on thin films samples. Figures 27a-f show the patterns of the lead bromide and iodide 2D perovskites with *n* = 6, 10, and 16 perovskites after water treatment, compared to as-prepared batches.

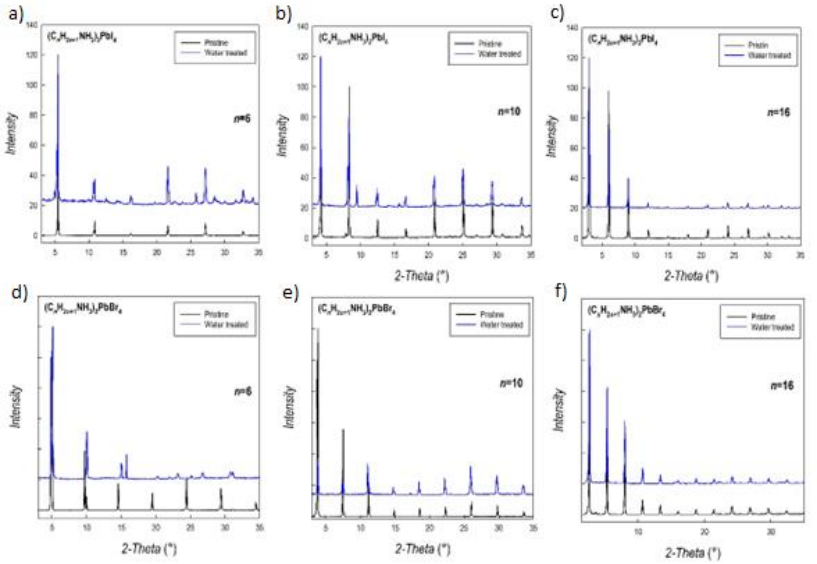

Figure 27 *XRD patterns before (black line) and after (blue line) water treatment for the $(C_nH_{2n+1}NH_3)_2PbI_4$ (a-c) and for the (b) $(C_nH_{2n+1}NH_3)_2PbBr_4$ (d-f) perovskites.*

In general, for both series of samples, complete degradation of the materials is not found even after the immersion in water and sample recovery. However, the patterns show an improvement of structural stability by increasing the length of the hydrocarbon chain. In more detail, for the $(C_nH_{2n+1}NH_3)_2PbI_4$ series, extra peaks are found for n=6 and 10, while the patterns before and after the water treatment are superimposable when n=16. For the bromide analogues, while significant differences are found when n=6, a nearly impressive similarity between the patterns before and after the water treatment is found when n=10 and 16. This difference in the water-resistance between the two series of samples could be ascribed to the more polar nature of the inorganic framework when iodide anion is present in the perovskite.

Further insight into the hydrophobic characteristics of the 2D perovskites has been achieved through the measurement of the contact angle of the same samples reported above. For the measurements, films of about 500 nm have been prepared on quartz substrate through spin-coating method. Figures 28a and 28b report the trend of the contact angle as a function of time for the $(C_nH_{2n+1}NH_3)_2PbI_4$ and $(C_nH_{2n+1}NH_3)_2PbBr_4$ samples, respectively, for *n*=6, 10, and 16.

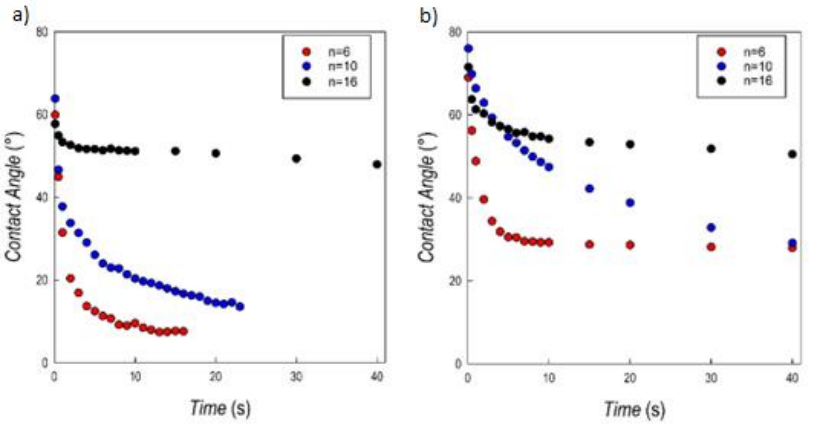

Figure 28 *Contact angle values as a function of time for the (a) $(C_nH_{2n+1}NH_3)_2PbI_4$ and (b) $(C_nH_{2n+1}NH_3)_2PbBr_4$ samples.*

For the $(C_nH_{2n+1}NH_3)_2PbI_4$ series, the starting value of the contact angle is roughly around 60°, without relevant differences as a function of *n*. For *n*=6 and 10, the angle value rapidly drops within the first seconds of the measurements and after about 20 seconds it is not possible to measure any value. On the opposite, for *n*=16, after an initial slight reduction of the angle, the value remains constant around 50°. This result confirms the evidence of a high hydrophobicity for the $(C_{16}H_{33}NH_3)_2PbI_4$ composition as reported recently in ref. 20 where the perovskite has been used in photocatalytic applications.[20] For the $(C_nH_{2n+1}NH_3)_2PbBr_4$ series the starting values of the

contact angles are higher with respect to the iodide analogues (Fig. 28a and 28b). In this case, the most relevant initial drop was observed for *n*=6 as for the other series, but in this case it was possible to measure the sample up to 40 seconds. The drop for the *n*=10 composition was less pronounced, but a significant reduction of the contact angle was observed during the measurement. Also in this case, differently with respect to the $(C_nH_{2n+1}NH_3)_2PbI_4$ series, the measurement could be performed up to the maximum time interval selected. Finally, for *n*=16, the value of the contact angle remains constant, around 60°, for the whole measurement, confirming the strong hydrophobicity also for the $(C_{16}H_{33}NH_3)_2PbBr_4$ composition. The contact angle measurements well correlate to the results of the tests reported in Figures 27a-f, indicating a general improved hydrophobicity by extending the hydrocarbon chain length but also moving from the iodide to the bromide anion.

Conclusions

In the present work we investigated the new systems $(C_nH_{2n+1}NH_3)_2PbBr_4$, focusing on the effect of the number of carbon atoms in the organic chain on structural, optical properties and improved hydrophobicity, providing a comparison with the analogue iodide systems reported in literature. The expansion of the chain length causes the expected rise of the perovskite cell, but an anomalous outcome concerns the longer c-axis for the bromide series with respect to the iodine counterparts. Moreover, the elongation of the organic chain induces a blue shift in both the optical absorption and photoluminescence spectra, which is more pronounced for the iodine series. In addition, the bromide-based compounds result more water-resistant than the corresponding iodine ones and the hydrophobicity increases along with the rise of the organic chain length.

References

1. Billing, D. G.; Lemmerer, A. Synthesis, characterization and phase transitions in the inorganic–organic layered perovskite-type hybrids $[(C_nH_{2n+1}NH_3)_2PbI_4]$, n = 4, 5 and 6. *Acta Crystallogr B Struct Sci* 2007, *63* (5), 735–747.
2. Billing, D. G.; Lemmerer, A. Synthesis, characterization and phase transitions of the inorganic–organic layered perovskite-type hybrids $[(C_nH_{2n+1}NH_3)_2PbI_4]$ (n = 12, 14, 16 and 18). *New J. Chem.* 2008, *32* (10), 1736.
3. Lemmerer, A.; Billing, D. G. Synthesis, characterization and phase transitions of the inorganic–organic layered perovskite-type hybrids $[(C_nH_{2n+1}NH_3)_2PbI_4]$, n = 7, 8, 9 and 10. *Dalton Trans.* 2012, *41* (4), 1146–1157.
4. Pisanu, A.; Coduri, M.; Morana, M.; Ciftci, Y. O.; Rizzo, A.; Listorti, A.; Gaboardi, M.; Bindi, L.; Queloz, V. I. E.; Milanese, C.; Grancini, G.; Malavasi, L. Exploring the role of halide mixing in lead-free BZA_2SnX_4 two-dimensional hybrid perovskites. *J. Mater. Chem. A* 2020, *8* (4), 1875–1886.
5. Tan, L. Z.; Zheng, F.; Rappe, A. M. Intermolecular interactions in hybrid perovskites understood from a combined density functional theory and effective Hamiltonian approach. *ACS Energy Lett.* 2017, *2* (4), 937–942.
6. El-Mellouhi, F.; Marzouk, A.; Bentria, E. T.; Rashkeev, S. N.; Kais, S.; Alharbi, F. H. Hydrogen bonding and stability of hybrid organic-inorganic perovskites. *ChemSusChem* 2016, *9* (18), 2648–2655.
7. Svane, K. L.; Forse, A. C.; Grey, C. P.; Kieslich, G.; Cheetham, A. K.; Walsh, A.; Butler, K. T. How strong is the hydrogen bond in hybrid perovskites? *J. Phys. Chem. Lett.* 2017, *8* (24), 6154–6159.
8. Li, X.; Lian, X.; Pang, J.; Luo, B.; Xiao, Y.; Li, M.-D.; Huang, X.-C.; Zhang, J. Z. Defect-related broadband emission in two-dimensional lead bromide perovskite microsheets. *J. Phys. Chem. Lett.* 2020, *11* (19), 8157–8163.

9. Gauthron, K.; Lauret, J-S.; Doyennette, L.; Lanty, G.; Al Choueiry, A.; Zhang, S.J.; Brehier, A.; Largeau, L.; Mauguin, O.; Bloch, J.; Deleporte, E. Optical spectroscopy of two-dimensional layered $(C_6H_5C_2H_4\text{-}NH_3)_2\text{-}PbI_4$ perovskite. *Optics Express*, Vol. 18, Issue 6, pp. 5912-5919 (2010).
10. Hintermayr, V. A.; Richter, A. F.; Ehrat, F.; Doblinger, M.; Vanderlinder, W; Sichert, J. A.; Tong, Y.; Polavarapu, L.; Feldmann, J.; Urban, A. S. Tuning the optical properties of perovskite nanoplatelets through composition and thickness by ligand-assisted exfoliation. *Adv. Mater.* 2016, 28, 9478-9485.
11. Sichert, J. A.; Tong, Y; Mutz, N; Vollmer, M.; Fischer, S.; Milowska, K. Z.; Cortadella, R. G.; Nickel, B.; Cardenas-Daw, C.; Stolarczyk, J. K.; Urban, A. S.; Feldmann, J. Quantum size effect in organometal halide perovskite nanoplatelets. *Nano Lett.* 2015, 15, 10, 6521-6527.
12. Bonomi, S; Tredici, I.; Albini, B.; Galinetto, P.; Rizzo, A.; Listorti, A.; Anselmi Tamburini, U.; Malavasi, L. Ambient condition retention of band-gap tuning in $MAPbI_3$ induced by high pressure quenching. *Chem. Commun.* 2018, 54, 13212-13215.
13. Filip, M. R.; Eperon, G. E.; Snaith, H. J.; Giustino, F. Steric engineering of metal-halide perovskites with tunable optical band gaps. *Nat. Commun.* 5:5757 doi: 10.1038/ncomms6757 (2014).
14. Li, X.; Hoffman, J. M.; Kanatzidis, M. G. The 2D halide perovskite rulebook: how the spacer influences everything from the structure to optoelectronic device efficiency. *Chem. Rev.* 2021, *121* (4), 2230–2291.
15. Aamir, M.; Shah, Z. H.; Sher, M.; Iqbal, A.; Revaprasadu, N.; Malik, M. A.; Akhtar, J. Enhanced photocatalytic activity of water stable hydroxyl ammonium lead halide perovskites. *Materials Science in Semiconductor Processing* 2017, *63*, 6–11.
16. Latini, A.; Quaranta, S.; Menchini, F.; Lisi, N.; Di Girolamo, D.; Tarquini, O.; Colapietro, M.; Barba, L.; Demitri, N.; Cassetta, A. A novel water-resistant and thermally stable black lead halide

perovskite, Phenyl Viologen Lead Iodide $C_{22}H_{18}N_2(PbI_3)_2$. *Dalton Trans.* 2020, *49* (8), 2616–2627.

17. Ricciarelli, D.; Kaiser, W.; Mosconi, E.; Wiktor, J.; Ashraf, M. W.; Malavasi, L.; Ambrosio, F.; De Angelis, F. Reaction mechanism of photocatalytic hydrogen production at water/tin halide perovskite interfaces. *ACS Energy Lett.* 2022, 1308–1315.
18. Romani, L.; Bala, A.; Kumar, V.; Speltini, A.; Milella, A.; Fracassi, F.; Listorti, A.; Profumo, A.; Malavasi, L. PEA2SnBr4: A water-stable lead-free two-dimensional perovskite and demonstration of its use as a co-catalyst in hydrogen photogeneration and organic-dye degradation. *J. Mater. Chem. C* **2020**, *8* (27), 9189–9194.
19. Romani, L.; Speltini, A.; Ambrosio, F.; Mosconi, E.; Profumo, A.; Marelli, M.; Margadonna, S.; Milella, A.; Fracassi, F.; Listorti, A.; De Angelis, F.; Malavasi, L. Water-stable $DMASnBr_3$ lead-free perovskite for effective solar-driven photocatalysis. *Angewandte Chemie International Edition* 2021, *60* (7), 3611–3618.
20. Hong, Z.; Chong, W. K.; Ng, A. Y. R.; Li, M.; Ganguly, R.; Sum, T. C.; Soo, H. S. Hydrophobic metal halide perovskites for visible-light photoredox C−C bond cleavage and dehydrogenation catalysis. *Angewandte Chemie International Edition* 2019, *58* (11), 3456–3460.

3.2 Decylammonium cation

After investigating the role of the number of carbon atoms in the aliphatic chain and its effect on structural and optical properties, as well as on the perovskite stability and hydrophobicity, we focused on decylammonium as organic spacer. We prepared the same 2D bromine- and iodine-based systems, expanding our research on germanium and tin, scarcely investigated in literature in 2D MHPs, and studying the role of the metallic cation. In order to modulate the physical properties, we also adopted a chemical tuning strategy on the decylammonium-germanium perovskite, by synthetizing the solid solution $DA_2Ge(Br_{1-x}I_x)_4$ with x = 0, 0.15, 0.25, 0.5, 0.75, 0.85, 1. In the absence of crystal structure of these compounds, only a qualitative analysis has been performed to date.

3.2.1 Solid solution $DA_2Ge(Br_{1-x}I_x)_4$

The obtained seven samples appeared as shown in Figure 29. The white powder corresponds to x = 0 composition, DA_2GeBr_4, while the dark orange powder is DA_2GeI_4 with x = 1. Several techniques for the single crystals synthesis have been experimented with these compounds, such as acid precipitation, AVC method, controlled evaporation, but all of them failed in providing good quality crystals.

Figure 29 *Samples of the solid solution $DA_2Ge(Br_{1-x}I_x)_4$ from x=0 (white on the left) to x=1 (dark orange on the right).*

The XRD patterns (Figures 30a and 30b) clearly show a phase transition in correspondence of the x = 0.5 composition, where a sudden change of the *c*-axis occurs. This latter is longer for the pure Br compound with respect to the pure I sample, as already found for the other aliphatic spacers previously reported, despite of a higher ionic radius of iodide as compared to bromide. The DA_2GeI_4 structural data are not catalogued, although they have been calculated from structural refinement of DA_2PbI_4 crystallographic data[1] resulting in orthorhombic space group for x=1, x=0.85, x=0.75 and x=0.5 compositions, with a similar dimension of the *c*-axis. From the x=0.25 composition, a gap is observed with a pronounced elongation of the c-axis, corresponding to a possible phase transition. However, we were not able to index the obtained symmetry. The evolution of the *c*-axis along with the increase of iodine content is presented in Figure 30c; before and after the symmetry change, a slight expansion of the long axis occurs, induced by the different size of the anions.

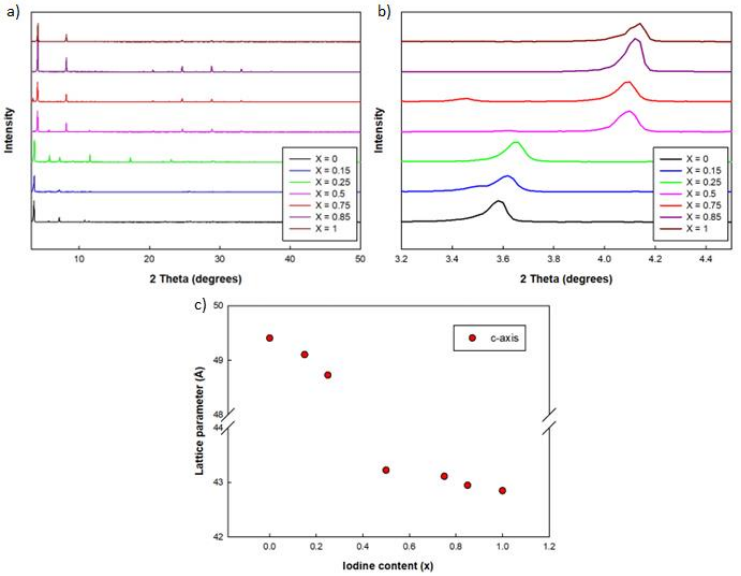

Figure 30 *a) X-Ray diffraction patterns of the seven samples from x=0 to x=1 of the solid solution $DA_2Ge(Br_{1-x}I_x)_4$.; b) enlargement of the first XRD peak; c) evolution of the c-axis vs. iodine content in the solid solution $DA_2Ge(Br_{1-x}I_x)_4$.*

While comparing the optical absorption measurements, narrow and well-defined curves are displayed; a general red shift can be also observed by increasing the iodine content in the solid solution (Figure 31a). The modulation of the band gap from x=0 to x=1, calculated from the Tauc Plots, is the following: 2.74 eV, 2.40 eV, 2.34 eV, 2.21 eV, 2.18 eV, 2.175 eV, 2.17 eV. By investigating the change of the band gap value along with the iodine content increase, an important change of 0.6 eV is evident moving from the pure bromine to the pure iodine compound, as Figure 31b shows. This anomalous trend seems to be parabolic, however it presumably consists in two ranges of the gap variation due to the phase transition, assumed on the basis of the diffraction patterns.

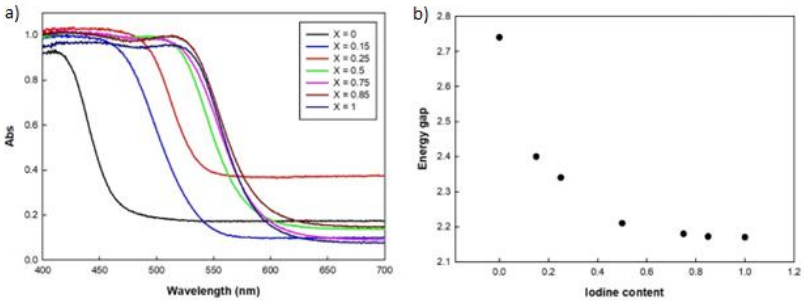

Figure 31 *a) Comparison of the optical absorption curves of the seven compounds of the solid solution $DA_2Ge(Br_{1-x}I_x)_4$. b) Trend of the band gap versus iodine content.*

The photoluminescence (PL) of these Ge-based solid solutions reveals very broad emission spectra (Figure 32a), probably as a consequence of the existence of defect states and of the more pronounced distortion induced by the presence of Ge in comparison to 2D Pb-based perovskites, as already demonstrated in one of our previous works[2].

We also observed that the room-temperature PL shape remains constant with the halogen variation and a progressive reduction of the emission intensity is evident as long as the Br amount increases, resulting in a total absence of the emission at room temperature in the case of DA_2GeBr_4. This progressive decrease correlates to the lifetimes trend (τ) reducing from τ =

1.6 to τ = 0.2 ns along with the rise of bromine content in the solid solution (Figure 32b). On the contrary, low-temperature PL measurements (77 K) show an intensity increase with shape and width, similar to room-temperature DA_2GeI_4 curve (Figure 32c-e).

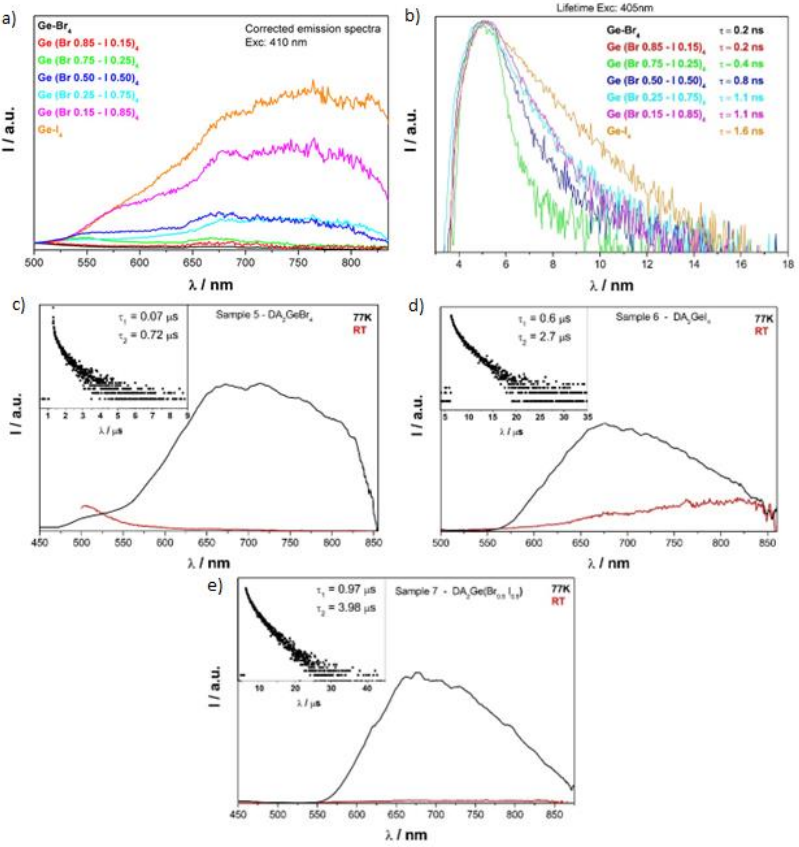

Figure 32 *a) Comparison of the room-temperature photoluminescence spectra of the seven compounds of the solid solution $DA_2Ge(Br_{1-x}I_x)_4$. b) Lifetimes for the seven samples. c) Low-temperature (77 K) PL spectrum of DA_2GeBr_4. d) Low-temperature (77 K) PL spectrum of DA_2GeI_4. e) Low-temperature (77 K) PL spectrum of $DA_2Ge(Br_{0.5}I_{0.5})_4$.*

Therefore, we can affirm that the PL spectra of these materials are not affected by the halogen nature in terms of curve shape but there is a strong dependence on temperature. On the other hand, the halogen type deeply influences the emission intensity. Moreover, at low temperature, lifetimes become significantly longer, by the order of μs. DA_2GeBr_4 sample, not emissive at room temperature, shows very broad PL at 77 K, while DA_2GeI_4 and the x=0.5 composition, presenting broad room-temperature spectra, exhibit a narrowing in the emission width at the same low temperature. The presumed origin of this broad-emission is still under investigation, even though previous works focused on Ge described the presence of this metal accounting for a significant distortion within the inorganic octahedra[2], the related reason could thus be sought in the generation of self-trapped excitons due to lattice distortion.

3.2.2 Comparison among Pb/Ge/Sn decylammonium systems

We investigated the effect on structural and optical properties due to the replacement of germanium with other 14th group metals such as tin and lead. The appearance of the prepared samples is shown in Figure 33.

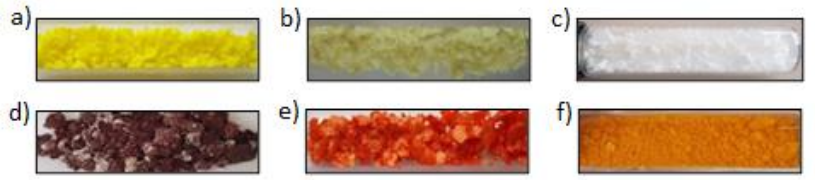

Figure 33 *Images of the prepared samples a) DA_2SnBr_4, b) DA_2GeBr_4, c) DA_2PbBr_4, d) DA_2SnI_4, e) DA_2GeI_4, and f) DA_2PbI_4.*

In the XRD patterns for both the I- (Figure 34a) and Br-based perovskites (Figure 34b), we noticed a shift of the main peaks towards higher angles moving from Ge to Sn to Pb, probably caused by an increase of the organic

spacer distortion, related to the different interaction with the inorganic framework. Interestingly, it should be noted that the c-axis seems to be longer for the bromide compounds with respect to the iodine, despite the bromide ion has a smaller ionic radius with respect to the iodide. The diffraction patterns show a predominance of the long axis reflexes, hindering a detailed investigation of the crystal structure.

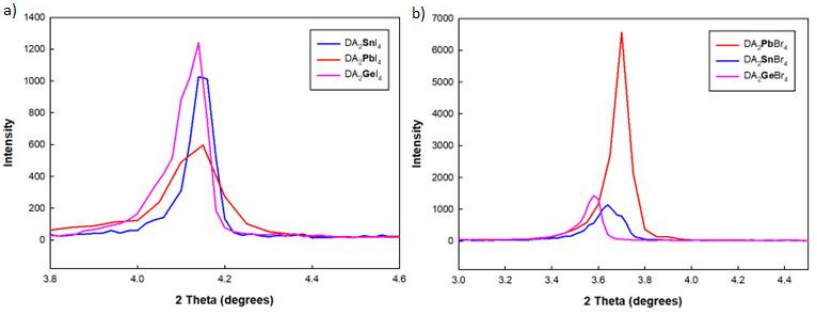

Figure 34 *Comparison of the first peak of X-Ray diffraction patterns for a) iodine-based compounds: DA_2PbI_4, DA_2SnI_4, DA_2GeI_4, and b) bromine-based samples: DA_2PbBr_4, DA_2SnBr_4, DA_2GeBr_4.*

By the substitution of Ge, the optical absorption spectra (Figure 35) present a significant red-shift for Sn and a blue-shift for Pb in both bromine and iodine systems; the classical effect of 0.5 eV difference in the band gap also occurs owing to the change from bromine to iodine, already found in the 3D perovskites. The values of the experimental band gap, calculated from the Tauc Plot, are the following:

- DA_2**Sn**Br_4 = 2.54 eV, DA_2**Ge**Br_4 = 2.74 eV, DA_2**Pb**Br_4 = 3.04 eV;

- DA_2**Sn**I_4 = 1.87 eV, DA_2**Ge**I_4 = 2.17 eV, DA_2**Pb**I_4 = 2.29 eV.

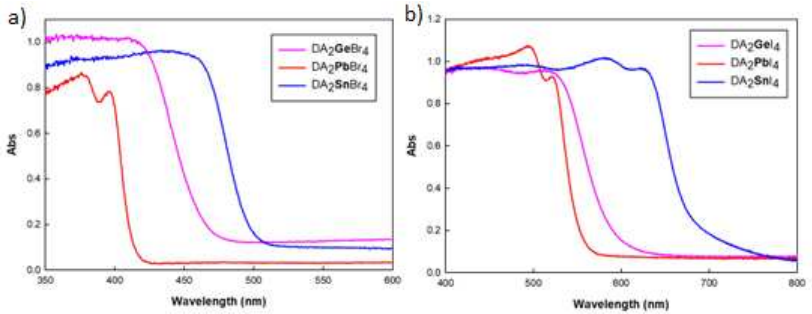

Figure 35 *Comparison of the optical absorption measurements for a) bromine-based and b) iodine-based systems.*

Figure 36 displays the photoluminescence spectra at room temperature for the Pb- and Sn-based compounds and, in the case of DA_2PbI_4, also the low-temperature measurements (77 K). DA_2SnBr_4 does not emit, while the other three perovskites at room temperature show very narrow PL spectra in comparison to the same Ge-based compound (see spectra in Figure 32): this is probably due to the reduced octahedral distortion induced by Pb and Sn and to the presence of a lower amount of defect states.[2] Actually, DA_2PbBr_4 exhibits one single emission peak, whereas DA_2PbI_4 presents two PL components, and DA_2SnI_4 shows even three contributions. In the case of DA_2PbI_4, we can observe a quite narrow emission centered at ~550 nm with a shoulder at ~520 nm: these two components are better resolved reducing the temperature at 77 K, also resulting in a shift to lower wavelengths and promoting the appearance of a broad-emission peak centered at ~700 nm. This temperature-dependent change could be motivated with the formation of defect states or something happening in the organic framework.[3] However, further structural investigations would be necessary in order to explain such phenomena.

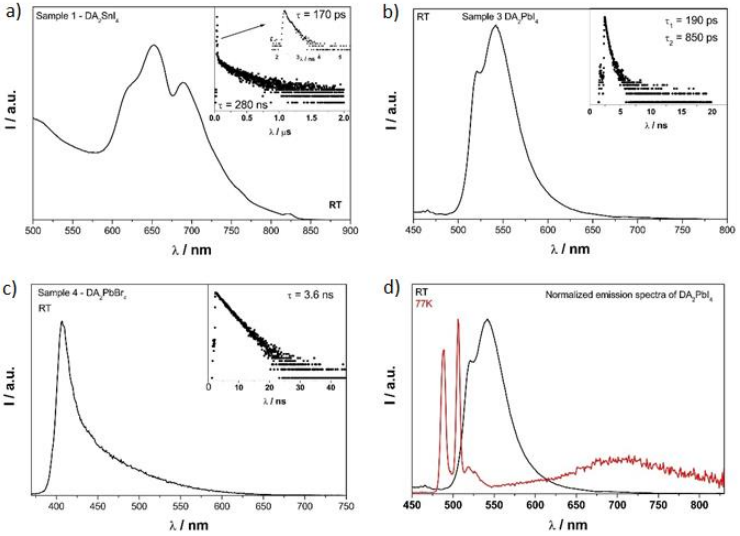

Figure 36 *Photoluminescence spectra of a) DA_2SnI_4 at room temperature, b) DA_2PbI_4 at room temperature, c) DA_2PbBr_4 at room temperature and d) DA_2PbI_4 at low temperature (77 K).*

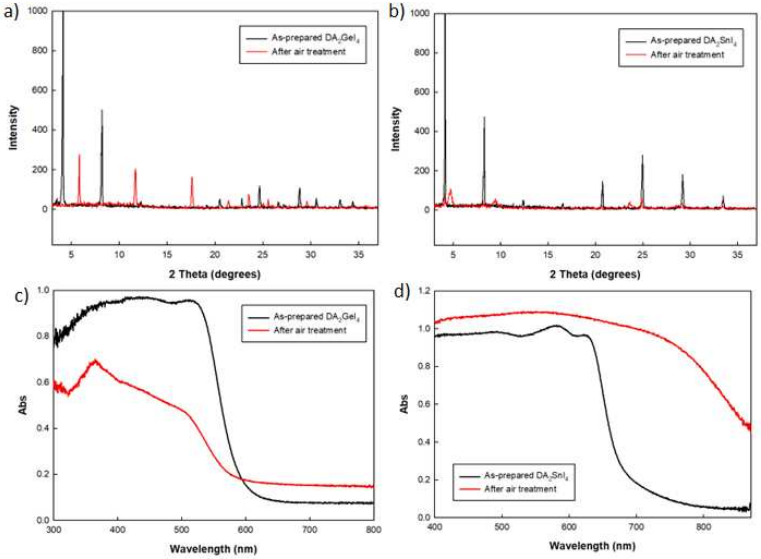

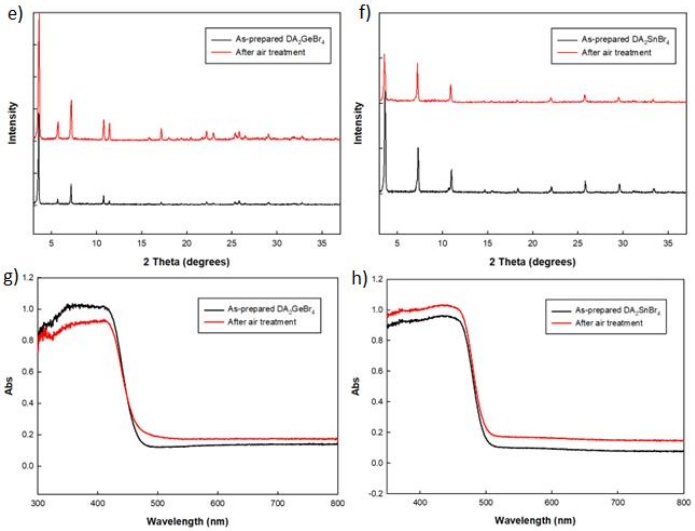

Figure 37 *a) XRD diffraction pattern of the as-prepared DA_2GeI_4 (black) and after the air treatment (red); b) XRD diffraction pattern of the as-prepared DA_2SnI_4 (black) and after the air treatment; c) comparison of the absorption spectra of the as-prepared DA_2GeI_4 (black) and after the air treatment (red); d) comparison of the absorption spectra of the as-prepared DA_2SnI_4 (black) and after the air treatment (red); e) XRD diffraction pattern of the as-prepared DA_2GeBr_4 (black) and after the air treatment (red); f) XRD diffraction pattern of the as-prepared DA_2SnBr_4 (black) and after the air treatment; g) comparison of the absorption spectra of the as-prepared DA_2GeBr_4 (black) and after the air treatment (red); h) comparison of the absorption spectra of the as-prepared DA_2SnBr_4 (black) and after the air treatment (red).*

For the four Pb-free compounds, stability tests were performed by exposing materials to air for one month, then collecting XRD patterns and absorption spectra after the treatment. While the bromine-based samples seem to be stable in air (Figure 37e-h), the iodine compounds present different patterns and spectra related to their decomposition, as shown in Figure 37a-d.

Low-temperature diffraction on DA_2PbI_4

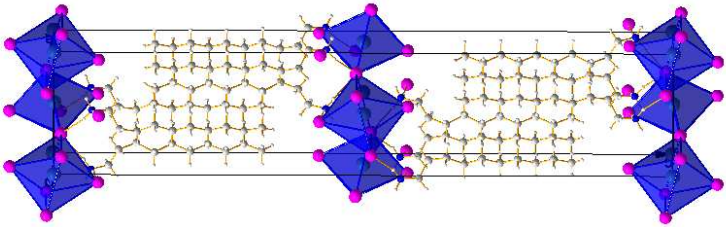

Figure 38 *Sketch of the crystal structure of DA_2PbI_4 at room temperature.*

DA_2PbI_4 at room temperature is orthorhombic, with space group *Pbca*, lattice parameters 9.01 Å x 8.69 Å x 42.61 Å (see Figure 38).[1]
The powder was loaded in a camera, which was evacuated and filled with 500 Torr of Helium. XRD patterns were collected from 3 to 40 deg. 2theta, 20 minutes in total. The crystals are oriented so that they show preferentially (00*l*) and, to a minor extent, (*hhl*) reflections. A minor amount of a secondary phase with a longer *c* lattice parameter was also observed. Room-temperature patterns are shown in Figure 39:

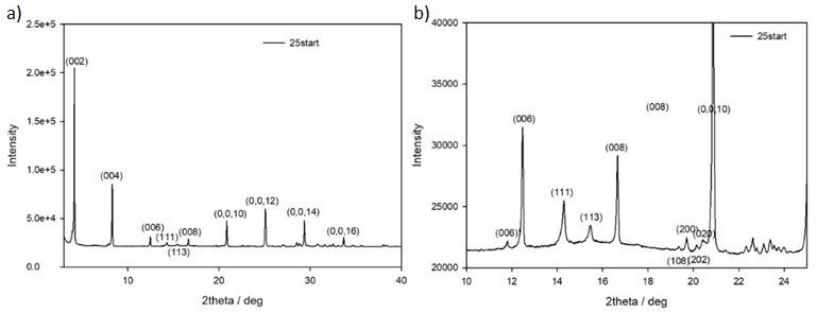

Figure 39 *a) Room-temperature pattern of DA_2PbI_4; b) Enlargement between 10° and 25° of the room-temperature pattern of DA_2PbI_4.*

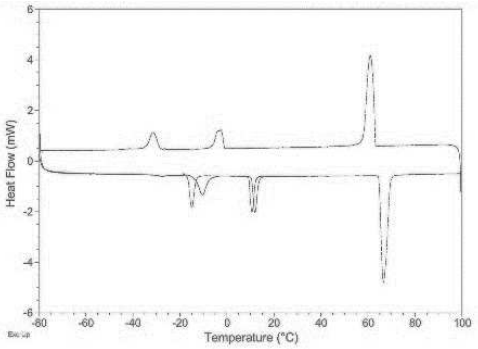

Figure 40 *DSC measurement of DA_2PbI_4.*

Patterns were collected upon cooling at 0, -20, -40, -60 and -80 °C, as presented in Figure 41, in order to cover the transformations revealed by DSC (Figure 40).

At 0°C two phases are observed, the second one corresponding to the traces revealed at room temperature, becoming the main phase at -20 °C. No further peaks were observed, the pattern is thus consistent with a single orthorhombic phase *Pbca* with shorter *a* and *b* lattice parameters, and a much longer *c* axis (44.0 Å). This is likely in line with the different orientation of the ammonium ions. Indeed, in our previous work on BZA_2SnX_4, the elongation of the *c* axis correlates with the tilt of the organic molecule with respect to the long axis.[4] Further cooling surprisingly leads to a similar unit cell like that occurring at ambient temperature, as testified by the shift of the (*00l*) reflections. However, a closer look at the background reveals a set of low intensity peaks not compatible with an orthorhombic cell. The indexing suggests a monoclinic cell, with halving of the long axis *c* and beta ~95°. This appears very similar to the room-temperature structure of the dodecylammonium lead iodide, space group $P2_1/c$.[1]

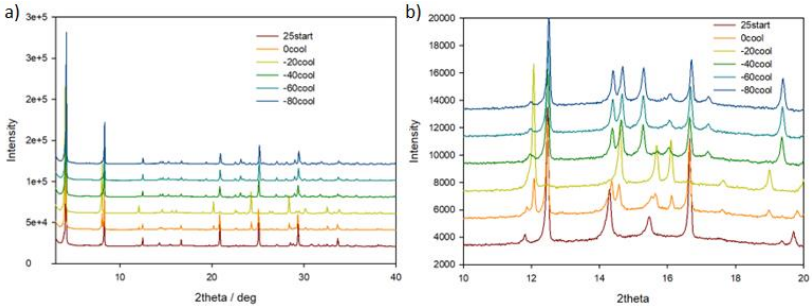

Figure 41 *a) Comparison of DA_2PbI_4 low-temperature diffraction patterns collected at 25°C (red), 0°C (orange), -20°C (yellow), -40°C (green), -60°C (light blue) and -80°C (blue); b) enlargement of the same patterns in the range 10-20°.*

By heating back the sample, we notice again both transformations (Figure 42). In addition, heating at 80°C induces an important expansion of *c* up to ~48 Å. A good fit is obtained with a tetragonal cell, already used to model the room temperature data.

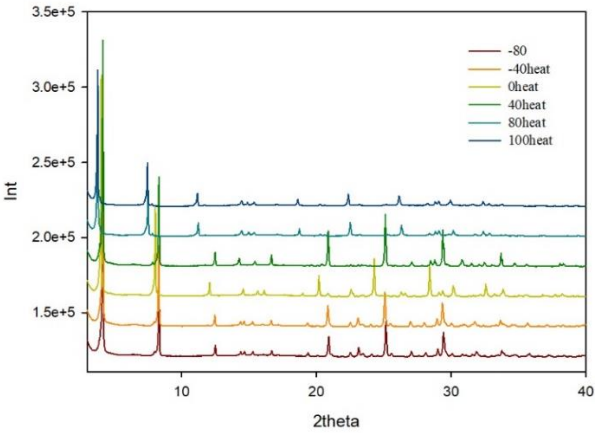

Figure 42 *X-Ray diffraction patterns of DA_2PbI_4 collected by heating from -80°C (red) to 100°C (blue).*

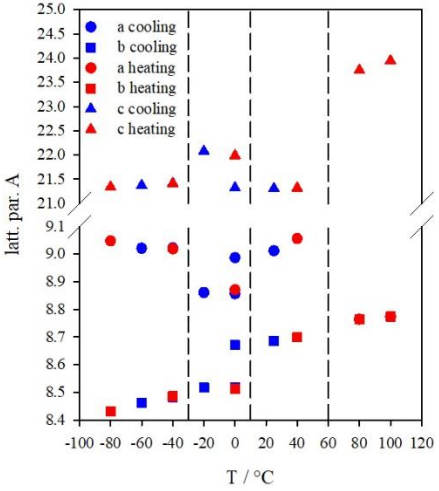

Figure 43 *Evolution of lattice parameters of DA_2PbI_4 upon cooling (blue) and heating (red).*

An overview of the lattice parameters, normalized through halving *c* of the orthorhombic and tetragonal structures, is given in Figure 43. The evolution of these parameters of DA_2PbI_4 are presented upon cooling (blue) and heating (red). An anomalous trend of the *c*-axis can be observed: starting from room temperature and heating, a significant expansion occurs, although the phenomenon also happens in correspondence of the first transition as a result of cooling, then followed by a contraction.

Low-temperature diffraction on DA_2SnI_4

DA_2SnI_4 diffraction patterns show a strong orientation of the sample, which preferentially reveals the *(00l)* reflections along the *c*-axis (Figure 44). In order to select the appropriate temperatures covering the transformations, DSC measurements have been performed revealing three reversible phase transitions and the existence of four different phases in a range between -60 °C and 80 °C (Figure 45). Starting from these results, patterns were

collected upon cooling at -20 °C and -60 °C and heating at 40 °C and 80 °C from room temperature.

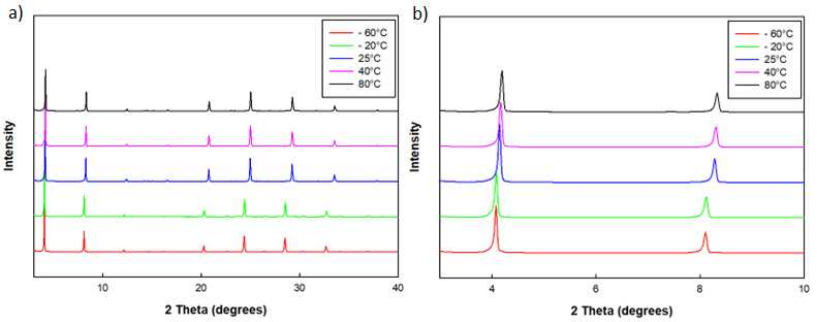

Figure 44 *a) Comparison of DA_2SnI_4 diffraction patterns collected at -60 °C (red), -20 °C (green), 25 °C (blue), 40 °C (pink), and 80 °C (black); b) enlargement of the same patterns in the range 3-20°.*

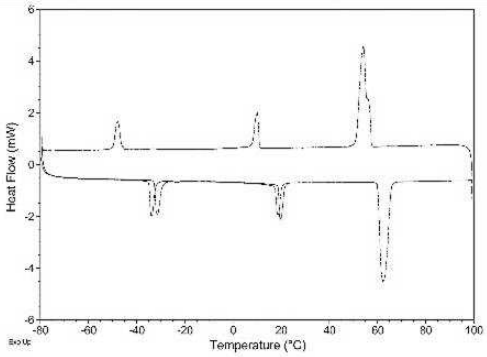

Figure 45 *DSC measurement of DA_2SnI_4.*

The sample crystal structure is still unknown either at room or at higher and lower temperatures, nevertheless it can be reasonable supposed, on the basis of previous findings, that these structural phase transitions could be

related to the change of the orientation and disposition of the alkylammonium chains in the interlayer spacing.[1]

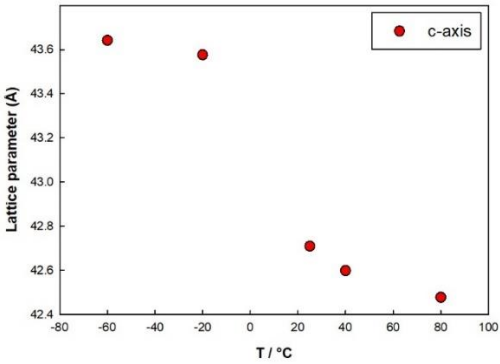

Figure 46 *Evolution of the c lattice parameter vs. temperature in DA_2SnI_4 sample.*

In particular, by analyzing the trend of the c axes as a function of the temperature (see Figure 46), we can observe its progressive decrease upon heating, while an elongation of the same axis occurs with cooling. This behaviour, looking different from the case of DA_2PbI_4, suggests a more straightened disposition of organic chains when the sample is cooled, while a tilt and a probably higher disorder of the decylammonium chains seem to be induced by heating.

Low-temperature diffraction on DA_2GeI_4

For DA_2GeI_4 sample, DSC thermogram reveals a first phase transition just under 0 °C and other two transitions in the temperature range of 40-60 °C (Figure 47). In this case diffraction patterns have been collected upon cooling at -20 °C and -60 °C and by heating at 50 °C and 80 °C, highlighting how, also these crystals, are strongly oriented, preferentially showing the (*00l*) reflections along the *c*-axis (Figure 48).

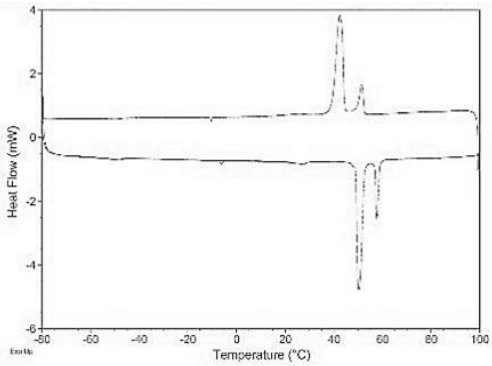

Figure 47 *DSC thermogram of DA_2GeI_4.*

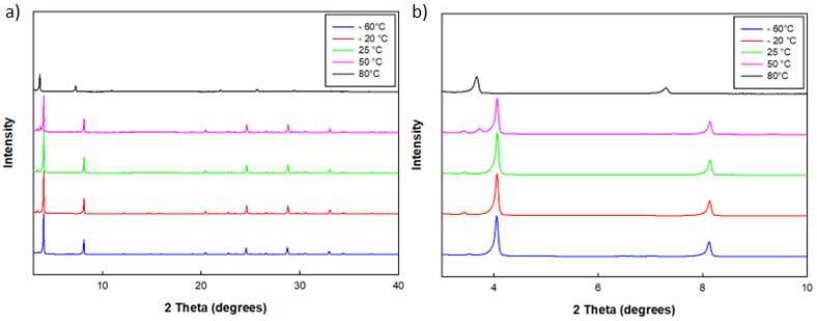

Figure 48 *a) Comparison of DA_2GeI_4 diffraction patterns collected at -60 °C (blue), -20 °C (red), 25 °C (green), 50 °C (pink), and 80 °C (black); b) enlargement of the same patterns in the range 3-20°.*

We can observe a similar anomalous behaviour to DA_2PbI_4, emerging in the trend overview of the *c* parameter (Figure 49). Starting from room temperature and cooling, a slight elongation of the *c*-axis occurs, only due to a straightening of the organic spacers induced by the effect of temperature without a phase transition, as shown by DSC. A little increase of *c* lattice parameter is also detected in correspondence of the first

transition, through heating from room temperature, then followed by a subsequent relevant elongation through the second and third transitions.[1]

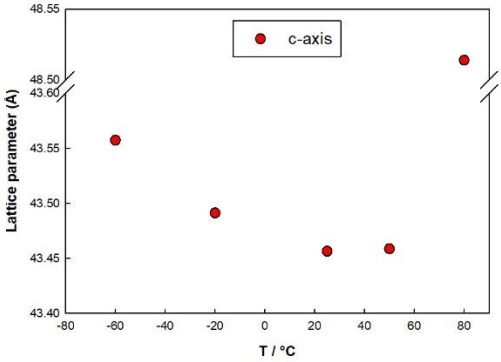

Figure 49 *Trend of the c lattice parameter vs. temperature in DA_2GeI_4 sample.*

Conclusions

In this study we explored novel lead-free MHPs compounds containing a linear aliphatic chain spacer, namely decylammonium. We prepared and characterized both germanium- and tin-based pure systems, as well as germanium-based Br/I solid solutions, with the purpose of providing a rational comparison to the analogous lead-based samples. The key role the central atom imparts on structural and, consequently, on optical behaviour has been also proved. Moreover, we investigated the structural stability and phase transitions occurring in these compounds as a function of temperature, providing the evidence of temperature-induced phenomena in the alkyl chain orientation and disposition.

Further experimental and computational investigations are underway in order to consolidate the knowledge of these new systems, with the aim of understanding the actual distortion level of the inorganic framework induced by the organic spacer.

References

1. Lemmerer, A.; Billing, D. G. Synthesis, characterization and phase transitions of the inorganic-organic layered perovskite-type hybrids $[(C_nH_{2n+1}NH_3)_2PbI_4]$, *n* = 7, 8, 9 and 10. *Dalton Trans*, 2012, 41,1146-1157.
2. Chiara, R.; Morana, M.; Boiocchi, M.; Coduri, M.; Striccoli, M.; Fracassi, F.; Listorti, A.; Mahata, A.; Quadrelli, P; Gaboardi, M.; Milanese, C.; Bindi, L.; De Angelis, F.; Malavasi, L. Role of Spacer Cations and Structural Distortion in Two-Dimensional Germanium Halide Perovskites. *J. Mater. Chem. C,* 2021**,** 9, 9899-9906.
3. Chiara, R.; Morana, M.; Folpini, G.; Olivati, A.; Albini, B.; Galinetto, P.; Chelazzi, L.; Ciattini, S.; Fantechi, E.; Serapian, S. A.; Petrozza, A.; Malavasi, L. The templating effect of diammonium cations on structural and optical properties of lead bromide perovskites: a guide to design broad light emitters. *J. Mater. Chem. C.* 2022, 10, 12367-12376
4. Pisanu, A.; Coduri, M.; Morana, M.; Ciftci, Y. O.; Rizzo, A.; Listorti, A.; Gaboardi, M.; Bindi, L.; Queloz, V. I. E.; Milanese, C.; Grancini, G.; Malavasi, L. Exploring the role of halide mixing in lead-free BZA_2SnX_4 two dimensional hybrid perovskites. *J. Mater Chem. A.* 2020, 8, 1875-1886

CHAPTER 4.

PHENYL-BASED MONOAMMONIUM SPACERS

As already pointed out, 2D MHPs are attracting increasing interest in the science community thanks to their vast structural/compositional diversity, which allows tuning of their properties by playing with the cage and spacer cations. [6,18,90,91] The vast chemical tunability of 2D MHPs has triggered significant interest in the elucidation of the role of crystal structure, the nature of the organic cation, and structural deformations on the optical properties of these materials. [6,18,31,92–95] This aim, together with the desire for playing with the chemical and structural degrees of freedom of 2D perovskites, has led to the continuous preparation and characterization of novel materials, thus enlarging the material records and providing reliable correlations. The modulation of the organic spacer can significantly tune the PL emission to broadband as a consequence of the octahedral distortion induced by hydrogen bonding, thus modifying the tendency for charge trapping. [92,96–100] Analogously, the band gap (E_g) of 2D perovskites can be modified by adjusting the angular distortion between adjacent metal-halide octahedra, with an increase of the E_g as the angle deviates progressively from 180°. [93–95] By playing with the size of the organic ammonium cation, the extent and direction of the inorganic octahedral framework distortion can be modulated, having a different impact on band structure and therefore on the band gap. [93] Coming to the cage cation, *i.e.* the metal ion, nearly all of the available reports on 2D perovskites have focused on lead-based and more recently tin-based phases. So far, the correlation between structural distortion and the band gap in 2D lead- and tin-containing perovskites has proved to be solid, thanks to the high and diverse number of prepared compositions, highlighting the impact of the interlayer metal (M) distance (or squared value), the average X-M-X (X =

halogen) bond angle, average M-X bond length, as well as the octahedral volume. [93,95] Much less has been done for alternative lead-free MHPs that incorporate other suitable metals, such as Ge, Bi, and Sb. [43,44]
With respect to 2D Ge-containing halide perovskites with n =1, just a couple of experimental reports are available in the current literature, namely, on BA_2GeBr_4 and PEA_2GeI_4. [69–71] However, the very limited number of available phases, containing also different halides, hinders any possible correlation between structural distortions and the optical properties.

4.1 Role of spacer cations and structural distortion in two-dimensional germanium halide perovskites

Purpose and scope

The elucidation of the structure–property correlation in 2D metal halide perovskite is a key issue to understand the dependence of optical properties on structural distortions and to design novel tailored materials. To extend the actual knowledge on this kind of correlation for lead-free materials, we synthesized and characterized four novel RP 2D germanium bromide perovskites (*n*=1), namely A_2GeBr_4 with $A=C_6H_4CH_2CH_2NH_3$ (phenylethylammonium, PEA), $BrC_6H_4CH_2CH_2NH_3$ (Br-phenylethylammonium, BrPEA), $FC_6H_4CH_2CH_2NH_3$ (F-phenylethylammonium, FPEA), and $C_6H_4CH_2NH_3$ (benzylammonium BZA), with the aim to investigate 2D systems based on aromatic cations. The chemical formula of the four organic cations is reported in Figure 50.

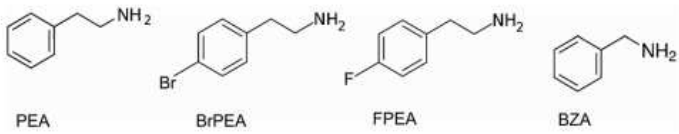

Figure 50 *Chemical formulae of the four amines used to prepare the Ge-based 2D perovskites: PEA, BrPEA, FPEA, and BZA.*

The crystal structure and phase behaviour of these novel compounds were determined using single-crystal X-ray diffraction (SCXRD) and variable temperature synchrotron X-ray powder diffraction (SXRPD) techniques, while the optical properties were investigated by absorption spectroscopy and steady-state and time-resolved PL in an effort to unveil a possible correlation between the band gap and emission properties with structural features, as already done for Pb and Sn analogues.[2,3] A dependence of the band gap value and emission characteristics in terms of Stokes shift and peak width has been highlighted and correlated with the octahedral distortion parameters. In addition, by comparing the actual results with previous data on analogous Sn- and Pb-based materials, we observed an intrinsic increased distortion induced by germanium, particularly on the octahedral bond elongation.

Experimental methods

Materials preparation

Single crystals were prepared by a solution method under inert atmosphere. The general procedure consisted in the dissolution of a proper amount of GeO_2 powder in a large excess of 48% w/w aqueous HBr in the presence of hypophosphorous acid (50% w/w aqueous H_3PO_2), in order to reduce Ge (IV) to Ge (II) and to stabilize the reduced oxidation state of germanium. The solution was maintained under continuous stirring and nitrogen atmosphere in order to prevent Ge oxidation. Then, the solution was gradually heated in

an oil bath to 130 °C until the solid dissolution and the stoichiometric amount of the amine (PEA, BZA, BrPEA, or FPEA) was added dropwise. Subsequently, a slow cooling down to room temperature at 1°C/5 min followed until the formation of a lamellar-shape bright pale-yellow product (for all the four perovskites). The precipitate was immediately filtered and dried at 65 °C under vacuum overnight. Samples have been stored in glovebox under argon atmosphere. The photos of the crystals are reported in Figure 51.

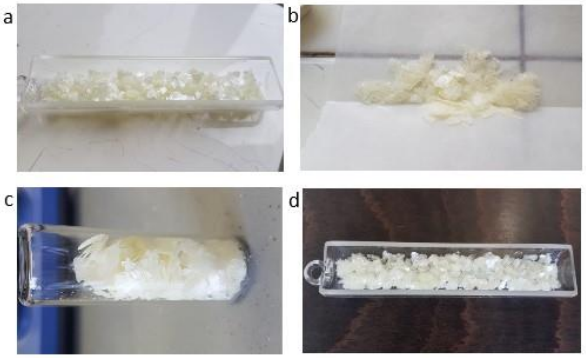

Figure 51 *Images of single crystals of a) PEA_2GeBr_4, b) BZA_2GeBr_4 c) $BrPEA_2GeBr_4$, and d) $FPEA_2GeBr_4$.*

Single crystal X-ray diffraction

Data at room temperature (λ = 0.71073 Å) for PEA_2GeBr_4 (CCDC 2084583), BZA_2GeBr_4 (CCDC 2084582) and $BrPEA_2GeBr_4$ (CCDC 2084581) were collected on a Bruker-Axs three-axis diffractometer equipped with the Smart-Apex CCD detector. Samples were quickly mounted and measured under nitrogen flux to avoid any sample oxidation. Omega-rotation frames were integrated with the SAINT software. The absorption correction was performed with SADABS-2016/2. Crystal structure was solved by direct methods as implemented in SIR 97 and refined using SHELXL-2018/3. Anisotropic displacement parameters were refined for all non-hydrogen

atoms. Hydrogens were placed at calculated positions with the appropriate AFIX instructions and refined using a riding model.

Crystal of PEA_2GeBr_4 appeared affected by twinning and the triclinic crystal structure was refined as a 2-component twin, with the twin law corresponding to a 180° rotation around the direction of the b unit cell edge. The PEA_2GeBr_4 compound was isostructural to the PEA_2SnBr_4 compound orientation of the triclinic unit cell adopted in literature and it was also used in our study.

Also the triclinic crystal of the BZA_2GeBr_4 was proven twinned and the crystal structure was refined as a 2-component twin, with the twin law defined as a 180° rotation around the [001] reciprocal-axis direction. Some of the C atoms of the eight independent organic moieties showed large and elongated atom displacement parameters, which produced inaccuracy on the C atom positions and short C_{ar}-C_{ar} bond distances. Therefore, soft anti-bumping restraints (DFIX) were applied in the final refinement cycles, in order to obtain C_{ar}-C_{ar} bond distances of 1.39 ± 0.01 Å.

The orthorhombic non-centrosymmetric crystal structure of the $BrPEA_2GeBr_4$ compound was refined as a 2-component inversion twin. Moreover, extensive positional disorder affected the $GeBr_6$ octahedron, which appeared placed over alternative positions, mutually exclusive and occurring with the same statistical probability. The positional disorder was refined splitting both the atom site populated by the Ge species and two of the four independent atom sites populated by the Br species into two alternative and half populated positions.

Data collections at room temperature for $FPEA_2GeBr_4$ (CCDC 2084735) were performed using a Rigaku Oxford Diffraction SuperNova diffractometer equipped with a Dectris PILATUS3 R200K-A detector and a micro-focus sealed X-ray tube (λ=0.71073 Å) X-ray diffraction intensity data were integrated with the CrysAlisPro package, while ABSPACK in CrysAlis RED was used for the absorption correction. The structure was initially solved in the space group $P2_1/m$. However, no reasonable models were obtained in this centric space group mainly because of the presence of overlapping positions and structural disorder. Most of the atomic positions seemed to agree with

the $P2_1/n$ space group requirements. At this stage, a careful analysis of the collected data showed that the *h0l* reflections with con *h+l = 2n+1* were present (due to a non-merohedric twinning) thus simulating the absence of the *n* glide. The structure was then solved and refined in the space group $P2_1/n$ using the program JANA2006. For details on the averaging of equivalent reflections for twins in JANA2006, see for instance the appendix in Gaudin *et al*. After location of the heavy metal positions, the crystal structure was completed through successive difference-Fourier maps using SHELXL 2018/3.

Data collections (λ=0.71073 Å) at 100 K were performed using a Bruker Apex-II CCD diffractometer with the Bruker APEX2 program. The Bruker SAINT software was used for integration and data reduction, while absorption correction was performed using SADABS-2016/2. Crystal structures (CCDC 2084734, 2084736, 2084737) were solved and refined using SHELXT 2014/5 and SHELXL 2018/3.

Synchrotron X-ray Powder Diffraction

S-XRPD data were collected at 17 keV (λ=0.72932 Å) on the high-resolution MCX beamline at the Elettra synchrotron light-source (Trieste, Italy) [doi:10.1002/zaac.201400163]. Finely ground powders were filled in 0.3 mm diameter borosilicate capillaries under moisture-free atmosphere (N_2 glove box with less than 1 ppm O_2 and H_2O) and sealed using a cutting torch. Capillaries were spun at 300 rpm and measured in Debye-Scherrer geometry on the 4-circles Huber goniometer using a scintillator detector. Measurements at low temperature (100-300 K) were carried out by blowing a cold nitrogen stream using an Oxford Instruments cryojet, while temperatures above 300 K were achieved using a hot-air gas-blower (Oxford Danfysik DGB-0002). A minimum of 5 minutes stabilization time was allowed before each measurement. Instrument profile was calculated using a silicon NIST standard (SRM 640c) and refining the peaks shape with the pseudo-Voigt (PV) function. Data were then analyzed by means of Rietveld refinement using the structural models reported in the main text.

DSC measurements

Differential scanning calorimetry (DSC) analyses were performed by a Q2000 apparatus (TA Instruments, New Castle, DE, USA) by heating about 6 mg of powder in a close aluminum crucible from −80 °C to 80 °C (heating rate 5 K/min) and subsequent cooling down to -80°C under nitrogen flux (50 mL/min). Three independent measurements were taken on each sample. Crucibles have been prepared in the glovebox.

PL measurements

A Fluorolog 3 spectrofluorimeter (HORIBA Jobin-Yvon), equipped with a 450 W xenon lamp as exciting source and double grating excitation and emission monochromators was used for the PL measurements. All steady state optical measurements were performed at room temperature, at λ_{exc}=370 nm and detected by a picosecond photon counter (TBX ps Photon Detection Module, HORIBA Jobin-Yvon). The PL recombination dynamics were obtained by Time-Correlated Single Photon Counting (TCSPC) using a FluoroHub (HORIBA Jobin-Yvon) module and a laser diode emitting at 375 nm (NanoLED N375L, pulse width < 200 ps, average power of 11pJ/pulse) with a repetition rate of 250 KHz as pulsed excitation source. Samples have been placed between two microscope slides and sealed with Kapton tape to protect them from air.

Computational method

First-principles calculations based on density functional theory (DFT) are carried out as implemented in the PWSCF Quantum-Espresso package. Geometry optimization is performed using GGA-PBE level of theory and the electrons-ions interactions were described by ultrasoft pseudo-potentials with electrons from Br 4s, 4p; F 2s, 2p; N, C 2s, 2p; H 1s; Ge 4s, 4p, 3d; shells explicitly included in calculations. Band structures have been calculated using GGA-PBE level of theory. DOS calculations have been performed by a single point hybrid calculations including SOC using the modified version of the HSE06 functional including 43% Hartree-Fock exchange with norm-

conserving pseudo potentials with electrons from Br 4s, 4p; N, C 2s, 2p; H 1s; Sn 4s, 4p, 5s, 5p, 4d; shells explicitly included in calculations.
The experimental cell parameters have been used in all the cases. Geometry optimizations are performed with a k-point sampling of 4×4×1 along with plane-wave basis set cutoffs for the smooth part of the wave functions and augmented electronic density expansions of 25 and 200Ry, respectively. HSE06-SOC calculation has been performed 1×1×1 k-point sampling with planewave basis set cutoffs for the smooth part of the wave functions and augmented electronic density expansions of 40 and 80Ry, respectively.

Results and discussion

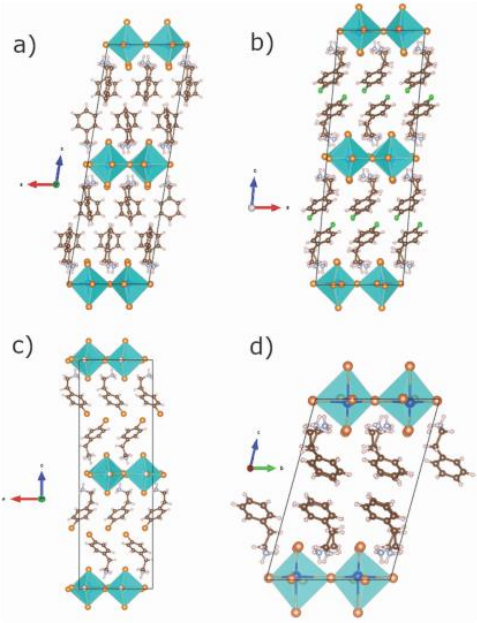

Figure 52 *Structural sketches of (a) PEA_2GeBr_4, (b) $FPEA_2GeBr_4$, (c) $BrPEA_2GeBr_4$ and (d) BZA_2GeBr_4.*

SCXRD revealed that the four investigated structures consist of a single {100}-oriented layer of $GeBr_6$ octahedra alternating with organic cation bilayers, and the corresponding structural sketches are reported in Figure 52.[1]

The crystal symmetry ranges from triclinic to orthorhombic, as reported in Table 1, with PEA_2GeBr_4 and BZA_2GeBr_4 crystallizing in space group P-1, and $FPEA_2GeBr_4$ and $BrPEA_2GeBr_4$ crystallizing in $P2_1/n$ and $Pna2_1$, respectively.

Table 1 *Structural parameters of PEA_2GeBr_4, $FPEA_2GeBr_4$, $BrPEA_2GeBr_4$ and BZA_2GeBr_4.*

Sample	Chemical formula	Space group and lattice volume (Å^3)	Lattice parameters (Å)	Bond angles (°)
PEA_2GeBr_4	$(C_6H_4CH_2CH_2NH_3)_2GeBr_4$	$P\bar{1}$	11.4059(12)	80.5161(14)
		2181.4(4)	11.5242(12)	74.9498(14)
			17.4408(19)	90.0119(14)
$BrPEA_2GeBr_4$	$(BrC_6H_4CH_2CH_2NH_3)_2GeBr_4$	$Pna2_1$	11.3957(12)	90
		2347.1(4)	5.7978(6)	90
			35.524(4)	90
$FPEA_2GeBr_4$	$(FC_6H_4CH_2CH_2NH_3)_2GeBr_4$	$P2_1/n$	33.5176(12)	90
		4375.9(2)	11.5028(3)	94.990(3)
			11.3930(3)	90
BZA_2GeBr_4	$(C_6H_4CH_2NH_3)_2GeBr_4$	$P\bar{1}$	11.1707(16)	99.569(4)
		4245.0(10)	11.4313(16)	99.275(2)
			34.172(5)	90.012(2)

According to the above discussion, we used the structural data obtained to extract some relevant parameters correlating with the structural distortions.[2,3,4] The distortion of the octahedra themselves can be quantified in terms of the average octahedral elongation length ($\{\lambda_{oct}\}$) and their bond angle variance (σ_{oct}^2), as defined by Robinson et *al.*, and is usually related to a broadened photoluminescence.[2,5] The distortion increases from BZA_2GeBr_4 to the PEA-containing samples, reaching a maximum for $BrPEA_2GeBr_4$ (Figure 53); it is worth noting that $BrPEA_2GeBr_4$ shows the splitting of the Ge and of two Br crystallographic sites, which might cause a larger distortion.

This trend is consistent with previous examples referring to Sn- and Pb-based 2D perovskites reported in the literature (Figure 54), where BZA_2MBr_4 compounds (M = Pb, Sn) show small distortion parameters, and PEA_2PbBr_4 has a larger structural strain.

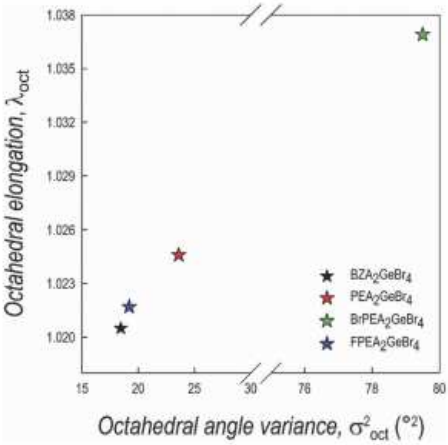

Figure 53 *Octahedral distortion parameters for PEA_2GeBr_4, $BrPEA_2GeBr_4$, $FPEA_2GeBr_4$ and BZA_2GeBr_4.*

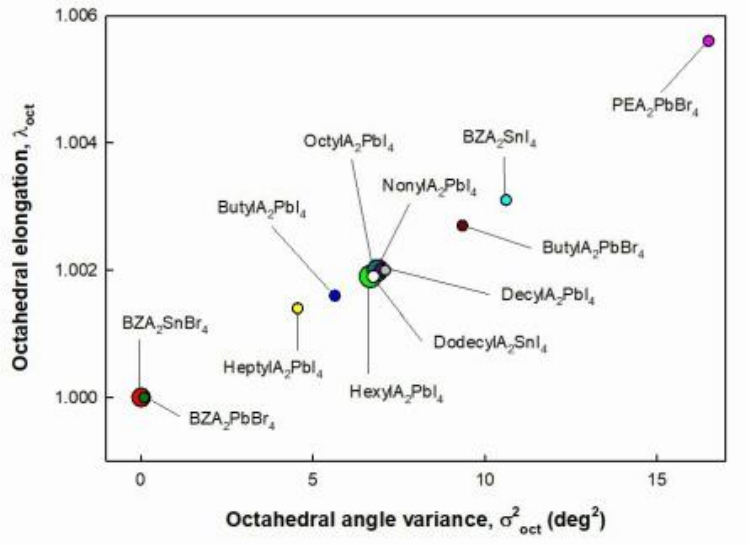

Figure 54 *Octahedral distortion parameters for different hybrid perovskites compositions.*

The presence of Ge seems to deeply affect the distortion within the octahedra. For example, in the case of the BZA organic spacer, the Ge-Br bond length varies from 2.5555(12) to 3.3279(15) Å, while the M-Br length ranges from 2.972(3) to 2.9959(11) Å in BZA_2PbBr_4 and from 2.940(4) to 2.977(1) Å in BZA_2SnBr_4.[4,6] Furthermore, a distortion index of the bond length of 0.1185 is larger than the values of 0.0039 and 0.0031 reported for BZA_2SnBr_4 and BZA_2PbBr_4, respectively, and, consistently, the octahedral elongation increases from the value of 1.000 of BZA_2SnBr_4 and BZA_2PbBr_4 to 1.0202.[4,6] Analogously, the octahedral angle variance of BZA_2GeBr_4 is two orders of magnitude larger with respect to BZA_2SnBr_4 and BZA_2PbBr_4.[6] Considering the compounds containing PEA, which generally show the largest distortion, we observe a similar structural strain induced by Ge. In fact, the Pb-containing analogue has the mean equatorial and axial bond lengths of 3.0018 and 3.0372 Å, respectively, a quadratic elongation of 1.0056 and an octahedral angle variance of 16.3496, while the Sn-containing sample has an average bond length of 3.0070 Å, from 2.8515(9) to 3.1744(9) Å, a quadratic elongation of 1.0058 and an angle variance of 17.3527.[4,7] Comparing these parameters with the respective values of 2.9365 Å, ranging from 2.5377(12) to 3.3532(14) Å, 1.0245 and 23.5846 in the Ge samples, it is clear that the octahedra are less regular and more distorted.

On the other hand, the presence of Ge has a smaller effect on the distortion between adjacent octahedra, which can be quantified as the deviation of the angle between the octahedra from 180°. In fact, for BZA the M-Br-M angle increases from 149.96° for Pb to 152° for Sn and 155.27° for Ge.[4,6] Analogously, for samples containing PEA, the angle increases from 151.46° for Pb to 152.54° for Sn and 157.82° for Ge.[4,6] Notably, the reported Ge-I-Ge angle in PEA_2GeI_4 is 158.34°, suggesting that the presence of Ge might induce a smaller distortion of the inorganic layers.[8] The distortion parameters for the four novel Ge-based 2D perovskites are summarized in Table 2 and will in the following be used to discuss a possible correlation with the optical properties presented below.

Table 2 *Distortion parameters for PEA_2GeBr_4, $BrPEA_2GeBr_4$, $FPEA_2GeBr_4$, and BZA_2GeBr_4 at room temperature*

	Average bond length Å	Polyhedral Volume Å^3	Distortion index	Quadratic elongation	Bond angle variance degrees^2	Ge-Br-Ge Angle degrees
PEA_2GeBr_4	2.9365	33.4205	0.1326	1.0245	23.5846	157.82
$BrPEA_2GeBr_4$	2.9301	32.3641	0.1111	1.0369	79.4978	156.37
$FPEA_2GeBr_4$	2.9299	33.2686	0.1258	1.0213	18.9101	157.94
BZA_2GeBr_4	2.9123	32.6517	0.1185	1.0202	18.4717	155.27

The possible phase transitions and the phase stability of the PEA_2GeBr_4, $BrPEA_2GeBr_4$, $FPEA_2GeBr_4$, and BZA_2GeBr_4 samples have been checked by means of differential scanning calorimetry (DSC) and variable-temperature SXRPD. Figure 55a shows the DSC traces of the samples between -75 and 75 °C, and these are flat, confirming the absence of peaks related to structural transitions. The low-*T* diffraction data have been refined using the RT SCXRD data, confirming the validity of the RT crystal structures to fit the patterns in the whole temperature range. The trend of the lattice volume as a function of temperature, as determined by Rietveld refinement (representative fits in Figure 56) for the four samples, is presented in Figure 55b and shows the expected progressive contraction of *V* upon reducing the temperature.

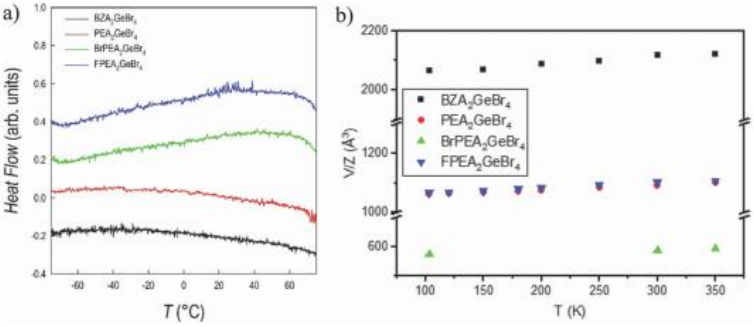

Figure 55 *(a) DSC traces and, (b) trend of lattice volume as a function of temperature for PEA_2GeBr_4, $BrPEA_2GeBr_4$, $FPEA_2GeBr_4$ and BZA_2GeBr_4.*

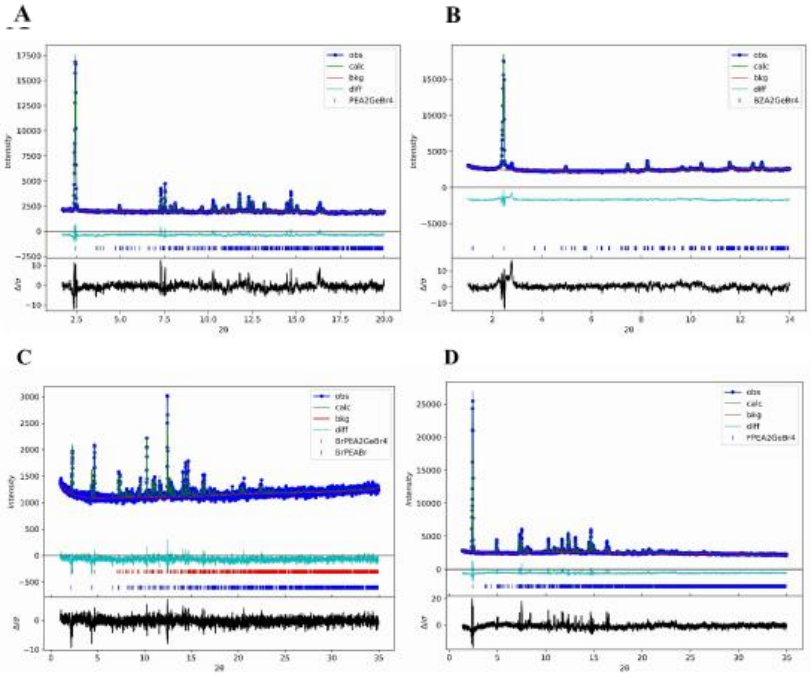

Figure 56 *Exemplary Rietveld refinements of the RT SXRD data for a) PEA_2GeBr_4, b) BZA_2GeBr_4, c) $BrPEA_2GeBr_4$, and d) $FPEA_2GeBr_4$.*

As a further test, single crystals of PEA_2GeBr_4, $FPEA_2GeBr_4$, and BZA_2GeBr_4 were selected and characterized by SCXRD at 100 K. The compounds crystallize in the same structure, owing to the expected reduction in cell parameters and contraction of the bond lengths and the distortion parameters (see Table 32).

Table 3 *Distortion parameters for PEA_2GeBr_4, $FPEA_2GeBr_4$, and BZA_2GeBr_4 at 100 K.*

	Average bond length Å	Polyhedral Volume Å^3	Distortion index	Quadratic elongation	Bond angle variance degrees^2	Ge-Br-Ge Angle degrees
PEA_2GeBr_4	2.9212	32.9271	0.1271	1.0225	21.6474	157.37
$FPEA_2GeBr_4$	2.9299	32.7452	0.1249	1.0207	17.9598	157.60
BZA_2GeBr_4	2.8999	32.2786	0.1167	1.0191	15.3505	155.02

Figures 57a and 57b report the comparison among the normalized absorption and PL spectra for PEA_2GeBr_4, $BrPEA_2GeBr_4$, $FPEA_2GeBr_4$ and BZA_2GeBr_4, while Figures 57c and 57d show the PL recombination dynamics measured by TCSPC.

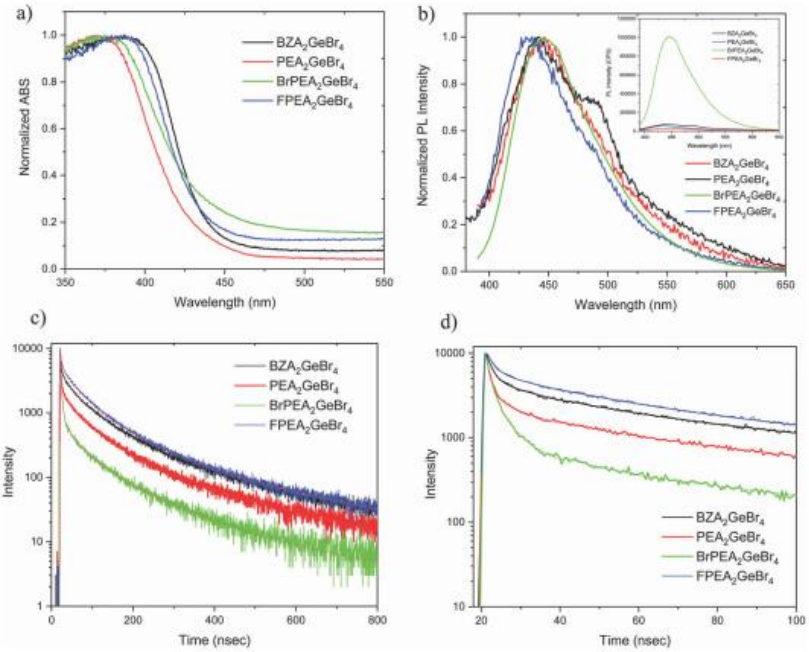

Figure 57 *(a) Normalized optical absorbance and (b) steady-state PL (λ_{exc} = 370 nm) and (c and d) TR decay profiles of PEA_2GeBr_4, $BrPEA_2GeBr_4$, $FPEA_2GeBr_4$ and BZA_2GeBr_4 (λ_{exc} = 375 nm). The fitting curves are reported as solid lines in the decay measurements. The non-normalized PL spectra are shown in the inset of (b).*

The band gap of the samples was determined from Tauc plots by considering a direct band gap nature, as determined by DFT calculations (see later in the text), and corresponds to 3.01 eV for PEA_2GeBr_4, 2.95 eV for $BrPEA_2GeBr_4$, 2.91 eV for $FPEA_2GeBr_4$, and 2.89 eV BZA_2GeBr_4. PL data confirm the variation of the band gap along with the change of the organic spacer, with

the emission band peaking at 2.78 eV for both PEA_2GeBr_4 and $BrPEA_2GeBr_4$, 2.85 eV for $FPEA_2GeBr_4$, and 2.81 eV for BZA_2GeBr_4. The Stokes shift is not uniform across the samples, with $FPEA_2GeBr_4$ and BZA_2GeBr_4 showing a smaller shift of about 0.3 eV, and PEA_2GeBr_4 and $BrPEA_2GeBr_4$ a larger one of about 0.46 eV. The comparison of the PL spectra in the inset of Figure 57b highlights the intense emission of $BrPEA_2GeBr_4$ with respect to the other $GeBr_4$ samples, generally characterized by a moderate PL intensity. The normalized PL spectra show clearly that the emission bands are relatively broad, in comparison to the 2D lead-based perovskites, due to the above discussed structural distortions, showing a full width at half maximum (FWHM) that varies from 0.5 eV for the narrower $BrPEA_2GeBr_4$, to 0.65 eV of the wider BZA_2GeBr_4, with the central member of the series having an FWHM of about 0.6 eV.[2] The BZA_2GeBr_4 emission also shows some hints of band structuring, with a weak shoulder appearing at lower energies. The time-resolved PL (TRPL) spectra in Figures 57c and 7d show the decay profiles for all the samples. While analogue recombination dynamics are observed for BZA_2GeBr_4 and $FPEA_2GeBr_4$, characterized also by very similar band gaps and Stokes shift values, the decay becomes shorter for PEA_2GeBr_4 and more significantly for $BrPEA_2GeBr_4$, the latter also being characterized by a considerable fluorescence enhancement. The average lifetimes are calculated by fitting the PL decay with multi-exponential functions, carrying out decay profile interpolations using the least squares method. A $\tau_{average}$ of about 113 ns is calculated for BZA_2GeBr_4 and of 109 ns for $FPEA_2GeBr_4$, while a slightly more rapid lifetime of 102 ns is obtained for PEA_2GeBr_4 that significantly decreases to about 68 ns for $BrPEA_2GeBr_4$. The latter shows therefore the most intense emission and the shortest lifetime.[9] From Figure 57d we note how the difference in lifetimes among the four 2D germanium bromide perovskites is mainly determined within the first 30 ns, and is therefore significantly influenced by the excitonic recombination mechanisms.

The band gap evolution of the systems was also investigated using density functional theory (DFT) calculations. The difference in absolute band gap value between theory and experiment is due to the exciton binding energy,

which is not included in our calculations. Generally, such thin quantum well two-dimensional perovskites possess a high exciton binding energy in the range of ~300-450 meV, thus considering such exciton binding energy values, our experimental and theoretical band gap converges nicely.[10,11] While looking at the bandgap evolution among PEA_2GeBr_4 and its halogen substituents, PEA_2GeBr_4 shows the highest band gap, followed by a subsequent decrease in the bandgap with Br- and F-substitution at the PEA cation, which is very similar to experiment. A direct band gap comparison between BZA_2GeBr_4 and its halogen-substituted analogues is not possible due to the presence of the halogen substituents which introduce a fundamental difference by forming better stacking in the organic layers and hydrogen bonding in the structure.[12] In fact, it has already been reported that the stacking difference and hydrogen bonding can change the electronic properties significantly in 2D and 3D perovskites.[13,14] However, BZA_2GeBr_4 shows a lower band gap compared with PEA_2GeBr_4, which possess the analogous phase and atomic species to that of BZA_2GeBr_4, thus showing a consistent trend with experiments.

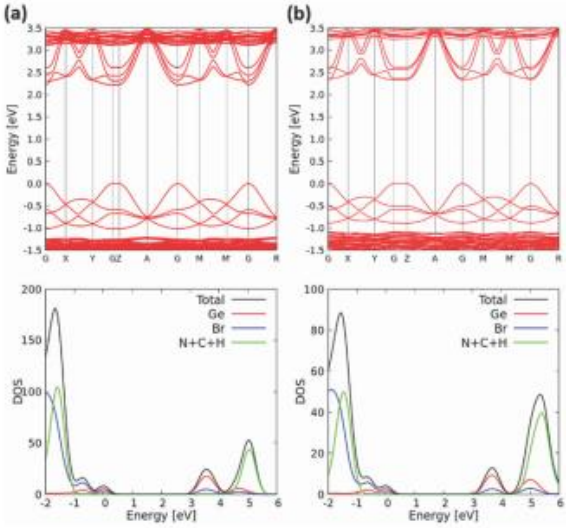

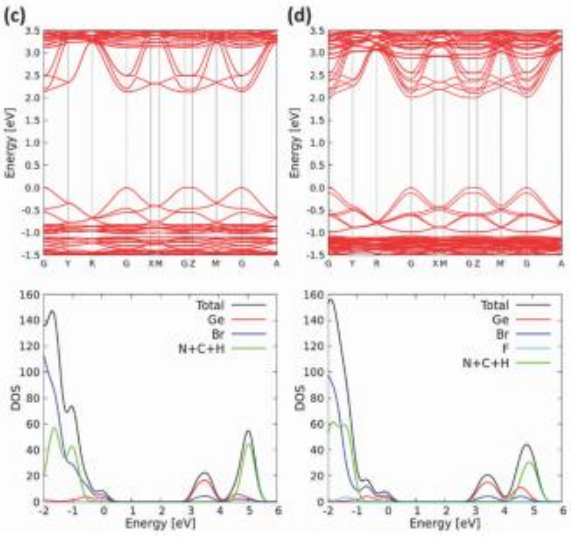

Figure 58 *Band structure (GGA-PBE level) and DOS (HSE06-SOC level) of (a) BZA_2GeBr_4, (b) PEA_2GeBr_4, (c) $BrPEA_2GeBr_4$ and (d) $FPEA_2GeBr_4$. The VBM has been set to zero in both the band structure and DOS figures.*

Calculation of the electronic band structure of the four systems (Figure 58) shows that all the structures have a direct band gap nature, which is again consistent with the experimental results of the optical measurements (Table 4).

Table 4 *Band gaps (eV) for the different structures at the HSE06-SOC level of theory.*

Composition	Experiment	Theory
BZA_2GeBr_4	2.89	3.34
PEA_2GeBr_4	3.01	3.46
$BrPEA_2GeBr_4$	2.95	3.24
$FPEA_2GeBr_4$	2.91	3.12

Taking together the structural and optical properties, it is possible to discuss their correlation considering the structural distortion of the four samples. We first consider the dependence of E_g and PL on the octahedral elongation $\{\lambda_{oct}\}$ and the bond angle variance (σ_{oct}^2). These parameters are known to affect the band gap and photoluminescence broadening, with a larger distortion correlating to larger band gaps and broadened PL. Building upon previous studies that show correlations between λ_{oct} and σ_{oct}^2 in Pb-based systems, the values reported in our investigation locate these 2D Ge perovskites in a region of substantially broad PL, accompanied by a high Stokes shift.[2,15] Looking at Figure 53, it can be seen that BZA_2GeBr_4 and $FPEA_2GeBr_4$ lie in a region of the λ_{oct} *vs.* σ_{oct}^2 where a lower Stokes shift should occur (with respect to the other samples). Indeed, this has been confirmed by PL and TRPL measurements, highlighting also for these two samples a longer $\tau_{average}$ in comparison with PEA_2GeBr_4 and $BrPEA_2GeBr_4$. Figures 59a and 59b display the trend of the band gaps for the four 2D samples as a function of λ_{oct} and σ_{oct}^2, confirming the correlation but still with the deviation of $BrPEA_2GeBr_4$, which can be ascribed to the peculiar structural disorder found in this sample, and which deserves further study.

The other key parameter affecting the band gap is the perovskite layer distortion, with its increase usually related to an increase of the bandgap.[4,16,17] This relationship holds for PEA_2GeBr_4, $BrPEA_2GeBr_4$, and $FPEA_2GeBr_4$, whereas BZA_2GeBr_4 has the largest deviation from 180° in the Br-Ge-Br angle but also the smallest bandgap (see Figure 59c). However, this compound shows the least distortion within the octahedra, which is true also for tin- and lead-containing analogues, with a small bandgap (2.4 eV) reported for BZA_2SnBr_4, too.[4,6] Thus, this behaviour might emerge from the interplay between the two main distortion mechanisms in hybrid perovskites, octahedral and layer distortion, with the former compensating the latter.

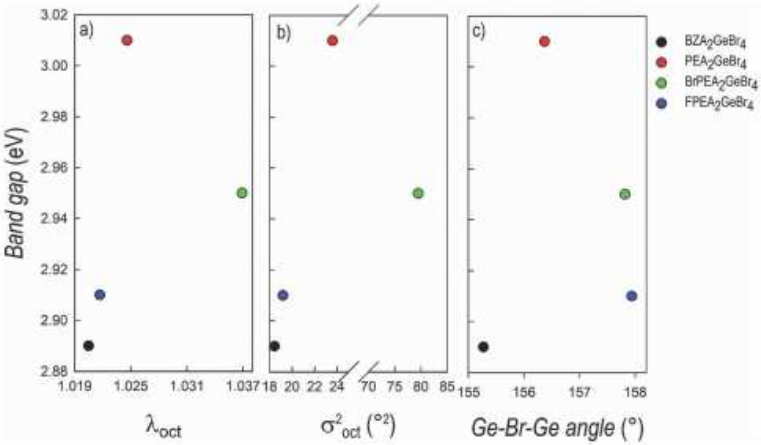

Figure 59 *Variation of the band gap as a function of the (a) octahedral elongation, (b) angle variance, and (c) Ge-Br-Ge angle for BZA_2GeBr_4, PEA_2GeBr_4, $BrPEA_2GeBr_4$ and $FPEA_2GeBr_4$.*

Finally, by taking together the present study and previous investigations on PEA_2SnBr_4, BZA_2SnBr_4, PEA_2PbBr_4, and BZA_2PbBr_4, some further correlations related to the role of the central atom in 2D metal halide perovskites, for the same organic spacers and halide, can be proposed. Figure 60 presents the plot of λ_{oct} and σ_{oct}^2 for the six samples, namely BZA_2BBr_4 and PEA_2BBr_4, B = Pb, Sn, and Ge. In the bottom left part of the plot, we find the BZA-containing samples, with Sn and Pb possessing a regular octahedral framework. By replacing BZA with PEA the distortion increases (in particular for the bond angle variance) for PEA_2PbBr_4 and PEA_2SnBr_4. On the other hand, the two Ge-containing samples show the highest level of distortion (the upper right part of the plot) for both cations, thus bringing to the fore the role of the central atom in the distortion correlation.

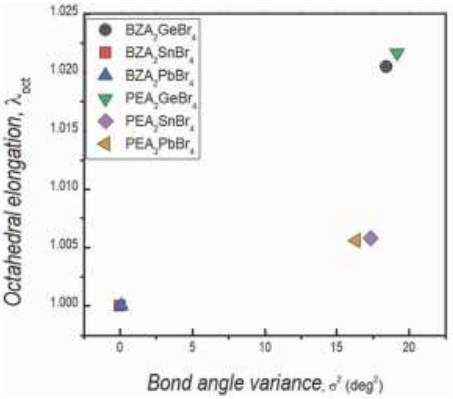

Figure 60 *Variation of the octahedral elongation vs. bond angle variance for BZA_2BBr_4 and PEA_2BBr_4, B = Pb, Sn, and Ge.*

This trend is of interest for the further design of 2D halide perovskites and in particular to look for white-emitting sample. Indeed, the central Ge atom provides, as also highlighted before, a significant degree of octahedral distortion, specifically with respect to λ_{oct} and σ_{oct}^2 angle variation. The first two parameters mostly affect the nature of the emission, providing broadened PL and relevant Stokes shifts, while the angle distortion mostly affects the band gap.[2,15-17] Even if the number of compositionally equivalent 2D metal halide perovskites available to perform correlations is modest so far (in terms of the organic spacer, central atom, and halide), based on the present and previous results we argue that a wise strategy to look for white-emitting 2D perovskites might be to use highly distorting organic spacers, such as 2,2'-(ethylenedioxy)bis(ethylammonium) (EDBE), coupled to Ge as the central atom, which already provides an intrinsically higher level of octahedral distortion with respect to Sn and Pb, but with less pronounced angular distortions affecting the band gap.

Conclusions

Four novel 2D Ge-based perovskites have been reported, namely A_2GeBr_4 with A = PEA, BrPEA, FPEA, and BZA, and characterized in terms of their crystal structure, optical properties, and computational modelling. The role of the different spacers has been demonstrated in terms of variation in the band gap and distortion, as well as Stokes shift and PL decay. Structural distortions in these layered perovskites have been highlighted by correlating the octahedral elongation length (λ_{oct}), bond angle variance (σ_{oct}^2), and Ge–Br–Ge angle variation to the mentioned optical properties. In general, some common trends with analogous parameters in Pb- and Sn-based 2D perovskites have been found; however, a peculiar role of Ge in increasing the octahedral distortion is seen in terms of elongation and bond angle variance, although this less in terms of Ge–Br–Ge deviations. BZA_2GeBr_4 and $FPEA_2GeBr_4$ were found to lie in a region of low λ_{oct} and σ_{oct}^2, which corresponds to lower band gaps and longer decay times compared with the more distorted PEA_2GeBr_4 and $BrPEA_2GeBr_4$. The range of correlations reported in this work for the 2D Ge-based perovskites and, where present, for the analogous Pb- and Sn-counterparts, sheds further on the relative role of cation-spacer-induced distortion and central atom (intrinsic) distortion on the octahedra framework. Overall, this set of results may help in predicting and designing novel germanium containing perovskites with tailored optical properties by utilizing the distortion level of the inorganic framework induced by the organic spacer, thus expanding the actual knowledge on 2D halide perovskites.

References

1. D. B. Mitzi, *J. Chem. Soc.*, Dalton Trans., 2001, 1-12.
2. D. Cortecchia, S. Neutzner, A. R. Srimath Kandada, E. Mosconi, D. Meggiolaro, F. De Angelis, C. Soci and A. Petrozza, *J. Am. Chem. Soc.*, 2017, 139, 39-42.

3. J. L. Knutson, J. D. Martin and D. B. Mitzi, *Inorg. Chem.*, 2005, 44, 4699-4705.
4. K. Du, Q. Tu, X. Zhang, Q. Han, J. Liu, S. Zauscher and D. B. Mitzi, *Inorg. Chem.*, 2017, 56, 9291-9302.
5. K. Robinson, G. V. Gibbs and P. H. Ribbe, *Science*, 1971, 172, 567-570.
6. A. Pisanu, M. Coduri, M. Morana, Y. O. Ciftci, A. Rizzo, A. Listorti, M. Gaboardi, L. Bindi, V. I. E. Queloz, C. Milanese, G. Grancini and L. Malavasi, *J. Mater. Chem. A*, 2020, 8, 1875-1886.
7. G. S. Lorena, H. Hasegawa, Y. Takahashi, J. Harada and T. Inabe, *Chem. Lett.*, 2014, 43, 1535-1537.
8. P. Cheng, T. Wu, J. Zhang, Y. Li, J. Liu, L. Jiang, X. Mao, R.-F. Lu, W.-Q. Deng and K. Han, *J. Phys. Chem. Lett.*, 2017, 8, 4402-4406.
9. J. R. Lakowicz, *Principles of fluorescence spectroscopy*, Springer, New York, NY, 3rd edn, corrected at 4. printing, 2010.
10. J.-C. Blancon, A. V. Stier, H. Tsai, W. Nie, C. C. Stoumpos, B. Traoré, L. Pedesseau, M. Kepenekian, F. Katsutani, G. T. Noe, J. Kono, S. Tretiak, S. A. Crooker, C. Katan, M. G. Kanatzidis, J. J. Crochet, J. Even and A. D. Mohite, *Nat. Commun.*, 2018, 9, 2254.
11. Y. Gao, M. Zhang, X. Zhang and G. Lu, *J. Phys. Chem. Lett.*, 2019, 10, 3820-3827.
12. F. Zhang, D. H. Kim, H. Lu, J.-S. Park, B. W. Larson, J. Hu, L. Gao, C. Xiao, O. G. Reid, X. Chen, Q. Zhao, P. F. Ndione, J. J. Berry, W. You, A. Walsh, M. C. Beard and K. Zhu, *J. Am. Chem. Soc.*, 2019, 141, 5972-5979.
13. M. Coduri, T. A. Strobel, M. Szafranski, A. Katrusiak, A. Mahata, F. Cova, S. Bonomi, E. Mosconi, F. De Angelis and L. Malavasi, *J. Phys. Chem. Lett.*, 2019, 10, 7398-7405.
14. C. Gao, R. Li, Y. Li, R. Wang, M. Wang, Z. Gan, L. Bai, Y. Liu, K. Zhao, S. F. Liu, Y. Cheng and W. Huang, *J. Phys. Chem. Lett.*, 2019, 10, 5687-5693.
15. D. Cortecchia, J. Yin, A. Petrozza and C. Soci, *J. Mater. Chem. C*, 2019, 7, 4956-4969.

16. J. L. Knutson, J. D. Martin and D. B. Mitzi, *Inorg. Chem.*, 2005, 44, 4699-4705.
17. P.-X. Wang, A. M. Najarian, Z. Hao, A. Johnston, O. Voznyy, S. Hoogland and E. H. Sargent, *J. Phys. Chem. Lett.*, 2020, 11, 10144-10149.

CHAPTER 5.

PHENYL-BASED DIAMMONIUM SPACERS

Despite the huge potential of 2D MHPs, the emissive properties of these materials have been very disappointing, an issue that can be related to a strong defect activity and a lack of knowledge and control of the structure-property relationship. The latter is strongly defined by the interconnection between the organic and the inorganic moieties driving the stiffness and distortion of the structure and thus its defectiveness. Investigating the templating action of the organic cation is thus critical. Most of the investigated organic spacers for 2D perovskites, to date, are monoammonium cations, while diammonium cations have been less explored. In the latter case, and in particular for short cations, the DJ phases are generally formed, where the inorganic layers are stacked in an eclipsed fashion on top of each other, differently from the RP phases where they are staggered. [6] In addition, 2D perovskites are not always stabilized by diammonium cations, and 1D structures, characterized by linear chains of octahedra, have been also often observed. For example, in the series of linear cations of the general formula $NH_3(CH_2)_mNH_3^{2+}$ (m = 4, 7, 8, 10, 12), the cations with even carbon-chain lengths form 2D perovskites, while those with odd carbon chain lengths form 1D structures. [22] Recently, the structural diversity of systems incorporating a diammonium cation has been further expanded towards 3D halide perovskitoids using linear cations such as 1,4-butanediamine (1,4-BDA), *N,N*-dimethyl-1,3-propanediamine (NMPA), or *N,N*-dimethylethylenediamine (DMEA), providing a structural motif comprising dimers with edge-sharing octahedra which are then connected through corner-sharing bonds to form a 3D network. [101] In these systems, the optical properties are close to traditional 3D MHPs with the bandgap being mainly influenced by standard octahedra distortion parameters. The correlation between structural distortions and optical

properties in 2D perovskites is a key topic to modulate their properties and design novel and optimized materials. Thanks to the vast work performed on perovskites including monoammonium cations, well-defined parameters have been defined and a careful materials design is now possible. [6] On the other hand, such kind of correlation is still partially missing on perovskites including diammonium cations. In this context, the most relevant studies have been carried out on some limited compositions including, for example, 2,2-(ethylenedioxy)bis(ethylammonium) (EDBE), N^1-methylethane-1,2-diammonium (*N*-MEDA), and 3-(2-ammonioethyl)anilinium (AEA) due to the interest in their very broad emission. [40,92,102,103] In (EDBE)$PbBr_4$, the strong structural distortion induced by the organic spacer closely affects its defectivity leading to the formation of V_F centers whose radiative decay ultimately leads to broadened photoluminescence (PL). [92] In the other Pb–Br perovskites, where crystal structures were solved by X-ray diffraction (XRD) on single crystals, the broadband emission was as well correlated to self-trapping of photogenerated carriers through excited-state lattice distortions. [103] The work of Smith and co-workers puts in prominence, among other structural parameters, the influence, on the relative intensity of the broad emission, of the distortion along the Pb–Br–Pb bond axis. [103] These results on diammonium cations further confirm the possibility of inducing slight distortions in the inorganic lattice by modifying the nature of the organic cation and therefore finely modulating the optical properties. However, the set of available structural data from single crystal diffraction – and their correlation with optical properties – on systems containing diammonium cations is still limited.

5.1 The templating effect of diammonium cations on the structural and optical properties of lead bromide perovskites: a guide to design broad light emitters

Purpose and scope

In the present work, we report the synthesis of four novel lead bromide MHPs (*n* = 1) investigating the templating role in the 2D structure formation by diammonium cations represented in Figure 61 (showing the corresponding amines), namely 1,3-phenylenediammonium (1,3-PDA), 1,3-xylylenediammonium (1,3-XDA), 1,4-phenylenediammonium (1,4-PDA), and 1,4-xylylenediammonium (1,4-XDA).

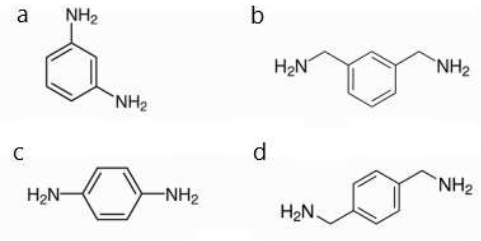

Figure 61 *Starting diamines used in the present paper for the synthesis of Pb-Br perovskites: a) 1,3-phenylenediammonium (1,3-PDA), b) 1,3-xylylenediammonium (1,3-XDA), c) 1,4-phenylenediammonium (1,4-PDA), d) 1,4-xylylenediammonium (1,4-XDA).*

The first two spacers have been recently investigated in Pb-I and Pb–Br thin films highlighting their improved moisture resistance (in particular, for 1,4-XDA), but in absence of single crystal XRD data.[1] Concerning 1,3-PDA and 1,3-XDA, the first cation has been investigated in Pb-I 2D perovskites as a function of the number of inorganic layers, *n* (providing the crystal structure), showing the formation of 2D DJ perovskites and the expected increase of the bandgap by increasing *n*.[2] These two cations have not yet been investigated in Pb-Br perovskites, and, in particular, 1,3-XDA-based lead halide systems have not been reported in the current literature.

For these new materials, we grew single crystals, solved the crystal structures, and report a detailed investigation of the optical properties, providing correlations with the bonding details and the interplay between the organic and inorganic components, which is a crucial step for the

understanding of structure property relationships in diammonium-based 2D perovskites. The novel systems reported in this work enlarge the family of broadband emitters and add further insights to develop efficient perovskite-based broadband and white light emitters.

Experimental methods

Materials preparation

$APbBr_4$ 2D perovskites (A = 1,3-phenylenediammonium (1,3-PDA), 1,3-xylylenediammonium (1,3-XDA), 1,4-phenylenediammonium (1,4-PDA), and 1,4-xylylenediammonium (1,4-XDA)) were grown by dissolving a proper amount of lead(II) acetate powder in a large excess of 48% w/w aqueous HBr and 50% w/w aqueous H_3PO_2, heating the mixture to boiling point. After the solid dissolution, the stoichiometric amount of the solid diamine (liquid for the 1,3-XDA) was added. The crystals formation was obtained by a slow cooling down to room temperature at 2°C h^{-1}.

Single crystal and powder X-ray diffraction

Single crystal data collections (λ = 0.71073 Å) were performed using a Bruker D8 Venture with Cu and Mo microfocus X-ray sources and PHOTON II detector with Bruker APEX3 program. The Bruker SAINT software was used for integration and data reduction, while absorption correction was performed using SADABS-2016/2. Crystal structures were solved and refined using SHELXT 2014/5 and SHELXL 2018/3.
XRD measurements on powdered samples were performed using a Bruker D8 Advance in Bragg-Brentano geometry under Cu Kα radiation.

Static and time-resolved photoluminescence

Powder sample preparation: the spectroscopic characterization was performed on perovskite powder samples encapsulated between 1 mm glasses.

Static Photoluminescence: Temperature and pump fluence-dependent measurements were performed under vacuum using a Linkam Stage cooled with liquid nitrogen, exciting the sample with the third harmonic (355 nm) from a Nd:YAG Picolo-AOT laser (pulse length of approximately 1000 ps, 1 kHz repetition rate) focused on the sample with a 10 cm lens. PL was detected using a Maya1000 visible spectrometer.

Time-resolved PL: The same light source as for static temperature dependent measurements (Picolo AOT at 355 nm) was used for time-resolved photoluminescence measurements on ns timescale. Measurements were performed under vacuum using a Linkam Stage cooled with liquid nitrogen. The PL was detected with an Andor iStar 320T ICCD camera coupled to a Shamrock 303i spectrograph using a temporal step size of 1 ns for sample (1,3-PDA)$PbBr_4$ and 10 ns for (1,4-PDA)$PbBr_4$ and (1,4-XDA)$PbBr_4$ with a spectral resolution of 0.55 nm.
TRPL of the excitonic feature in the ps range was performed using a Hamamatsu streak camera and a Coherent Chameleon oscillator (pulse duration 30 fs, repetition rate 80 MHz) as a pump, using a pump wavelength λ = 360 nm obtained by frequency doubling the fundamental at 780 nm in a BBO crystal. The measurements were performed using a measurement window 2000 ps long for all samples (temporal resolution 10 ps), while the fast component of 1,3-PDA was measured in a 180 ps window with the highest available temporal resolution (3.5 ps).

Results and discussion

Single crystal XRD (SC-XRD) revealed that the compounds crystallize in triclinic and monoclinic space groups, as reported in Table 5.

Table 5 *Crystal structure data for $APbBr_4$ samples (A = 1,3-PDA, 1,3-XDA, 1,4-PDA, and 1,4-PDA)*

Sample	Chemical formula	Space group and lattice volume (Å^3)	a, b, c (Å)	α, β, γ (°)
(1,3-PDA)$PbBr_4$	$(1,3\text{-}C_8H_{10}N_2)PbBr_4$	$C2/c$	21.784(7)	90
		Monoclinic	8.821(3)	107.214(9)
		1357.8(8)	7.398(3)	90
$(1,3\text{-XDA})_2PbBr_6$	$(1,3\text{-}C_8H_{14}N_2)_2PbBr_6$	$P2_1/c$	10.7571(18)	90
		Monoclinic	14.525(3)	103.540(4)
		1299.4(4)	8.5545(10)	90
(1,4-PDA)$PbBr_4$	$(1,4\text{-}C_8H_{10}N_2)PbBr_4$	$P\bar{1}$	7.434(3)	70.570(19)
		Triclinic	8.712(3)	78.527(19)
		658.9(4)	11.028(4)	89.414(19)
(1,4-XDA)$PbBr_4$	$(1,4\text{-}C_8H_{14}N_2)$ $PbBr_4$	$P2_1/c$	12.3274(7)	90
		Monoclinic	8.1618(4)	90.817(2)
		821.68(7)	8.1675(4)	90

Not all the samples investigated crystallize as a layered perovskite structure, in particular, this does not occur for the composition including the 1,3-XDA cation, giving the chemical formula $(1,3\text{-XDA})_2PbBr_6$. Graphical representations of the crystal structures are reported in Figure 62.

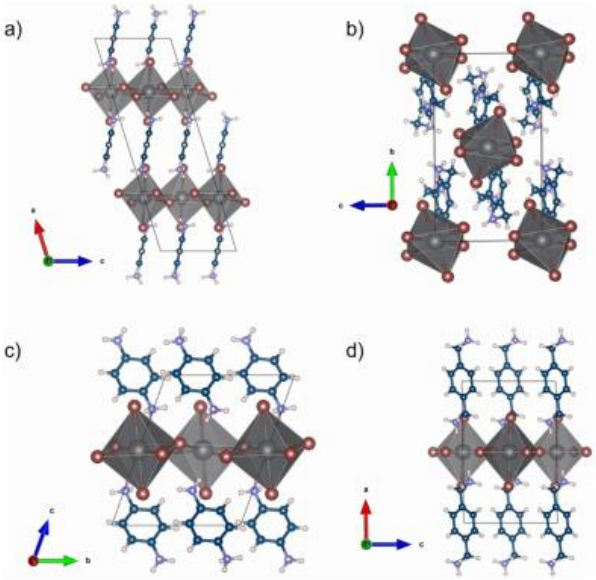

Figure 62 *Crystal structures of (a) (1,3-PDA)$PbBr_4$, (b) $(1,3\text{-XDA})_2PbBr_6$, (c) (1,4-PDA)$PbBr_4$, and (d) (1,4-XDA)$PbBr_4$.*

As mentioned, (1,3-XDA)$_2$PbBr$_6$ does not possess the perovskite structure, being constituted by a slightly distorted isolated octahedra, corresponding to a 0D perovskitoid. The crystal cohesion is then given by the aromatic cations whose NH_3^+ groups interact with both equatorial and axial Br atoms. To the best of our knowledge, this is one of the first 0D bromide perovskite derivatives including a diammonium cation, while chloride-containing 0D systems have been reported in the past.[3] (1,3-PDA)PbBr$_4$, (1,4-PDA)PbBr$_4$, and (1,4-XDA)PbBr$_4$ occur as DJ phases with n = 1, according to the general formula A'A$_{n-1}$M$_n$X3$_{n+1}$. They all comprise layers of PbBr$_6$ octahedra separated by layers of organic cations. The aromatic cations interact with the inorganic framework in the terminal mode. The interaction between the NH_3^+ terminal group and the inorganic framework is known to affect the structure and properties of hybrid halide perovskites.[4,5] In the case of diammonium cations, it was already reported that some cations cannot give origin to layered perovskite structures. For example, even-membered alkyl chains with ammonium groups at both ends form layered perovskite-type hybrid structures, both in bromide and iodide compounds whereas odd-membered chains do not.[6] The layered perovskite structure is adopted only when the chains are kinked so that the hydrogens on both the ends of the organic molecules can hydrogen bond with the halides of the inorganic layers.[6] Moving away from linear chains, it has been shown that cations with fused aromatic rings can give the layered perovskite structure only when the cation is able to tilt and hydrogen bond to the halides.[6] More generally, aromatic cations where the ammonium groups may have no degree of freedom do not necessarily give the layered perovskite motif, and 1D motifs are observed for 4,4'-MDAPbI$_4$[6] [MDA = methylenedianilinium ($H_3NC_6H_4CH_2C_6H_4NH_3$)], (1,4PDA)PbI$_4$,[7] whereas the aforementioned (1,3-PDA)PbBr$_4$, (1,4-PDA)PbBr$_4$, and (1,4-XDA)PbBr$_4$, together with (1,3-PDA)PbI$_4$,[8] (1,3-PDA)PbCl$_4$[3] and (AEA)PbBr$_4$ form a layered perovskite structure.[9] The XRD powder patterns obtained on the crushed crystals are reported in Figure 63 superimposed to the calculated patterns from the single crystal XRD data.

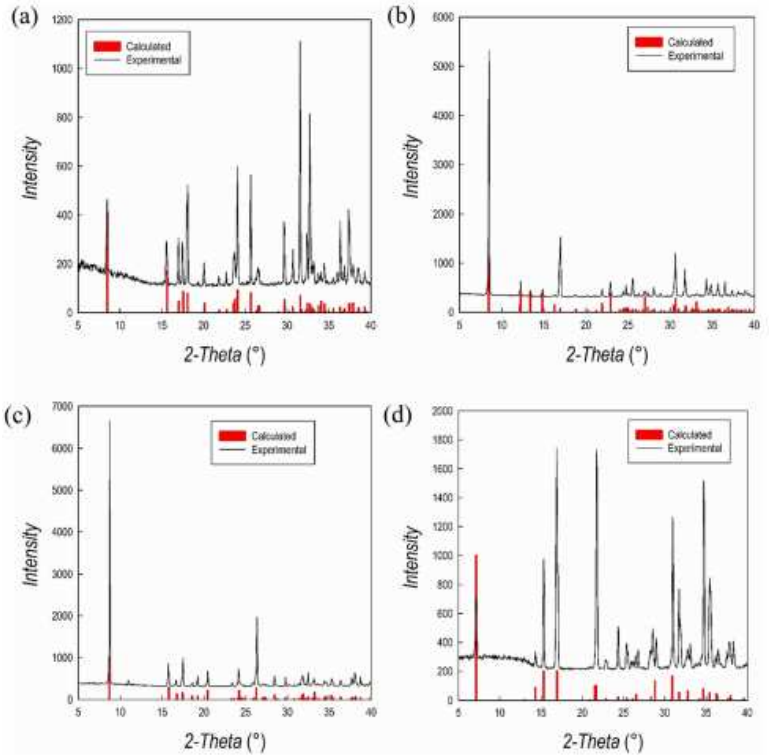

Figure 63 *XRD powder patterns of (a) (1,3-PDA)PbBr$_4$, (b) (1,3-XDA)$_2$PbBr$_6$, (c) (1,4-PDA)PbBr$_4$, (d) (1,4-XDA)PbBr$_4$ superimposed to the calculated patterns from SC-XRD (vertical red bars).*

We can further explore the interaction between the inorganic framework and the organic cation using the penetration depth, defined as the distance between the N atom of the amino group and the plane of the terminal halides, according to ref. 5. The NH_3^+ penetration affects both the distortion between the octahedra, in terms of deviation from 180° of the Pb-X-Pb angle, and within the octahedra, in terms of the octahedral elongation length (λ_{oct}), and their bond angle variance (σ^2_{oct}), as defined by Robison *et al.* (1971).[10] By comparing the present data for the 2D perovskites, and the above mentioned reported systems including diammonium cations, it is

possible to note that Pb-X-Pb angle increases with increasing penetration with a linear trend from chloride to iodide (Figure 64).

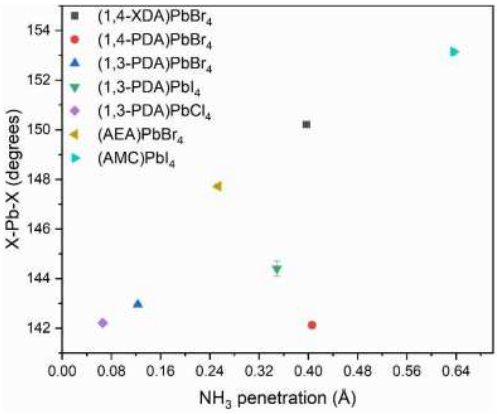

Figure 64 *Variation of the Pb-X-Pb bond angle as a function of NH_3 penetration.*

It is worth noting that (1,4-PDA)$PbBr_4$ falls outside this trend, probably because the PDA cation is short and rigid, and because of the increasing strength of the hydrogen bond from I to Br to Cl.[11,12] For the present 2D DJ perovskites, the values of the average Pb-Br-Pb angles are 142.95° for (1,3-PDA)$PbBr_4$, 142.12° for (1,4-PDA)$PbBr_4$, and 150.21° for (1,4-XDA)$PbBr_4$, indicating therefore a greater distortion for the two short diammonium cations with respect to 1,4-XDA. The plots correlating the octahedral elongation and bond angle variance of present 2D perovskites, and other DJ systems based on diammonium cations where crystal structure data are available, are reported in Figures 65a and 65b.

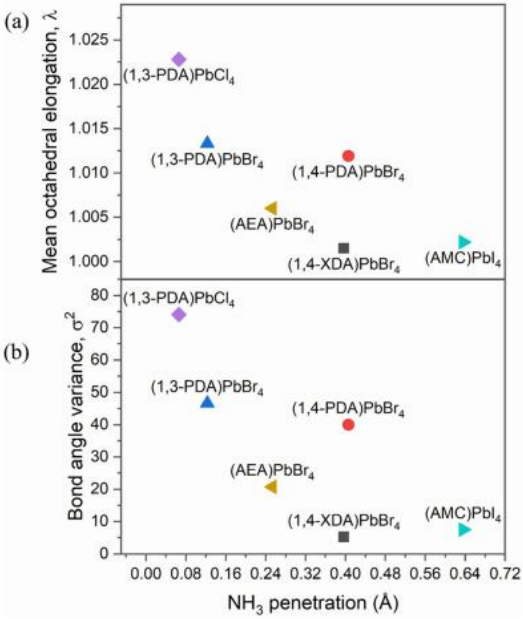

Figure 65 *(a) Octahedral elongation and (b) bond angle variance as a function of NH_3 penetration. PDA= phenylenediammonium; AEA = 3-(2-ammonio-ethyl)anilinium; XDA= xylylenediammonium; AMC = 1,4-bis(ammonio-methyl)cyclohexane. Values for (AEA)$PbBr_4$ and (1-4AMC)PbI_4 are calculated from ref. 8 and 9, respectively.*

It is clear that the octahedral elongation and bond angle variance of this group of compounds decrease as the NH_3^+ penetration increases. This effect may be a consequence of the flexibility of the organic cation, in particular of the degrees of freedom of the substituents on the aromatic ring. In fact, the 1,3-PDA cation, where all the atoms except the hydrogens are forced to lie in the same plane, induces a larger distortion among all the investigated halides.[3,13] Notably, the 1,4-PDA cation induces a distortion within the octahedra similar to the 1,3-PDA cation, whilst the distortion decreases for the 1,4-XDA that is more flexible since the nitrogen atoms are not bound to stay in the same plane as the aromatic ring. The smallest distortion is shown by 1,4-AMC cation, which is the aliphatic analogue of 1,4-XDA reported in

ref. 8, suggesting that a conjugate ring provides more rigid structural constraints.

To address the possibility that additional flexibility could be leading to the formation of stronger H-Br hydrogen bonds *via* differences in the electrostatic potential, we carried out a series of density functional theory (DFT) calculations on isolated diammonium cations 1,3-PDA^{2+}, 1,4-PDA^{2+}, and 1,4-XDA^{2+} in the gas phase; on isolated $[PbBr_6]^{4-}$ and $[Pb_2Br_{11}]^{7-}$ in the gas phase (retaining distortions present in each parent perovskite); and of the three systems (1,3-PDA)$PbBr_4$, (1,4-PDA)$PbBr_4$, and (1,4-XDA)$PbBr_4$, shown in detail in the experimental methods section.

Focusing on charges calculated for aminic protons and bromide, our single-point energy calculations show that while a systematic charge transfer from Br to -(N)H_3^+ is expectedly recognized upon perovskite formation by both charge assignment methods, charge distribution remains consistently uniform across atoms of all three isolated diammonium cations, atoms of the $[PbBr_6]^{4-}$/$[Pb_2Br_{11}]^{7-}$ octahedra, and perovskites (1,3-PDA)$PbBr_4$, (1,4-PDA)$PbBr_4$, and (1,4-XDA)$PbBr_4$ alike.[14,15] Geometry optimization (carried out for all species except $[PbBr_6]^{4-}$/$[Pb_2Br_{11}]^{7-}$ octahedra) does not alter the situation: changes observed with respect to single-point energy calculations always remain consistent across all atoms, and charges retain comparably uniform distributions across all three perovskite systems after optimization. Together with the relatively small variation in hydrogen bond lengths observed both experimentally and computationally across (1,3-PDA)$PbBr_4$, (1,4-PDA)$PbBr_4$, and (1,4-XDA)$PbBr_4$, these results lead us to conclude that there should be no systematic differences in electronic distribution between the three perovskites that could drive the formation of stronger or weaker hydrogen-halide bonds. This reasoning is further confirmed by the room temperature Raman spectra for (1,3-PDA)$PbBr_4$, (1,4-PDA)$PbBr_4$, and (1,4-XDA)$PbBr_4$ samples reported in Figure 66 in the range 70-250 cm^{-1}.

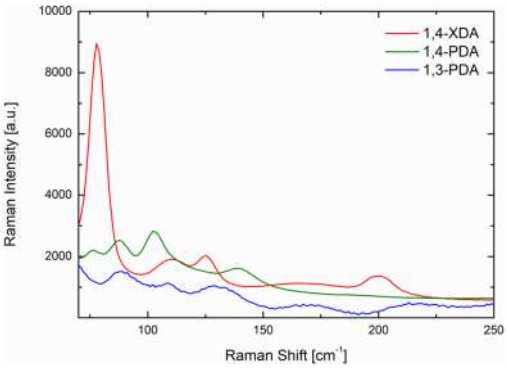

Figure 66 *Room temperature Raman spectra of (1,3-PDA)$PbBr_4$ (blue line), (1,4-PDA)$PbBr_4$ (green line) and (1,4-XDA)$PbBr_4$ (red line) excited at 632.8 nm with microscopic resolution. All the spectra are the average over 10 spectra collected along a line of 30 µm.*

According to ref. 14, in this energy region, two main vibrating reservoirs should be active: the stretching and bending modes of the Pb-Br cages in the lower energy part and the liberation of the organic cations partially bound to the Pb-Br framework.[16] At first, we observe well-defined Raman fingerprints for all the investigated samples thus confirming a high crystal quality. In addition, the data point out that the Raman yields from (1,3-PDA)$PbBr_4$ and (1,4-PDA)$PbBr_4$ are markedly lower with respect to that from (1,4-XDA)$PbBr_4$. This is particularly clear for the mode observed for (1,4-XDA)$PbBr_4$ at 78.5 cm^{-1} probably associated with the stretching motion of the Pb-Br unit. For (1,3-PDA)$PbBr_4$ and (1,4-PDA)$PbBr_4$, weaker bands are observed at 88 cm^{-1}. This behaviour is consistent with the greater distortion affecting the two short diammonium cations with respect to 1,4-XDA. In the region 130-250 cm^{-1} we observe, in comparison with the octahedral Raman yield, a small Raman activity decreases for 1,4-PDA and 1,4-XDA with respect to 1,3-PDA. Even if a detailed mode attribution is required, this could be due to the smaller NH_3^+ penetration characterizing (1,3-PDA)$PbBr_4$ sample.

The importance of the flexibility of the organic cation is confirmed by a closer analysis of the octahedral distortion reported in Figure 6.

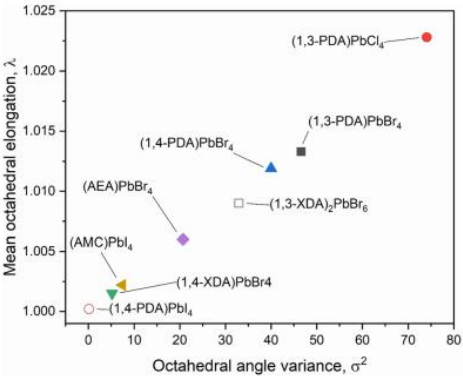

Figure 67 *Distortion parameters for the newly synthesized compounds and already reported materials with similar characteristics. Open symbols mark compositions that do not crystallize in a layered perovskite structure.*

In the plot of Figure 67, related to the octahedra structural parameters, we could also include those perovskite derivatives not crystallizing as 2D systems. For these systems, the distortion is mostly due to the arrangement of the inorganic framework. In particular, in (1,4-PDA)PbI_4, the asymmetric unit contains a Pb atom on a site of 2/*m* symmetry and two I atoms on mirror planes and thus, by symmetry, the equatorial plane is defined by four equivalent positions for atom I2, whereas the two equivalent positions for atom I1 are necessarily axial.[7] The symmetry constraints together with the edge-sharing motif that occurs through the equatorial I atoms give rise to regular octahedra. $(1,3\text{-XDA})_2PbBr_6$ comprises isolated and slightly distorted octahedra, characterized by a relatively high angle variance, suggesting a deviation of the Br-Pb-Br angles from 90°. The crystal cohesion is given by a framework of contacts between the amino groups and the bromide atoms. The organic molecule present in the asymmetric unit is tilted by 20° with respect to the (001) plane. Coming to the layered perovskites, the octahedra

show large distortion when cations where the nitrogen atoms are bound to sit in the same plane as the aromatic cation, such as the 1,3-PDA and 1,4-PDA, are present. On the other hand, the more flexible 1,4-XDA cation induces only a slight distortion in the $PbBr_6$ octahedra. Analogously with the AEA cation, where one nitrogen atom is bound to the aromatic plane and the other one is not, the octahedra adopts a distortion between those reported for 1,4-XDA and 1,4-PDA.[9] Again, based on the present results, the 2D DJ perovskites reported in this work show an octahedral distortion increasing passing from (1,4-XDA)$PbBr_4$ to (1,4-PDA)$PbBr_4$ and to (1,3-PDA)$PbBr_4$, with the last two showing, in particular, a significant increase in the octahedral angle variance with respect to (1,4-XDA)$PbBr_4$.

To further investigate the relationship between the structure of the perovskites, in particular the degree of octahedral distortion, and their optical properties, we performed an in-depth spectroscopic study on the samples which present the 2D DJ structure: (1,3-PDA)$PbBr_4$, (1,4-PDA)$PbBr_4$, and (1,4-XDA)$PbBr_4$. The materials' static absorbance and photoluminescence (PL) at room temperature are presented in Figure 68a. For all samples, the absorbance (solid lines), calculated from the reflectivity of powdered single crystals, shows an absorption edge well close to the UV range (between 380 nm and 420 nm) as expected for two- dimensional Pb bromides.[17-19] Furthermore, even at room temperature, a relatively narrow absorption peak can be observed on top of the band edge, consistent with a stable excitonic population, typical of the quantum confinement effect.[18] The static PL (dashed lines) measured under pulsed excitation at 355 nm shows a more diverse picture: only (1,4-XDA)$PbBr_4$ shows a narrow peak (~26 nm bandwidth) centered at 421 nm with a Stokes shift of only a few nm, as expected from excitonic photoluminescence. On the other hand, (1,3-PDA)$PbBr_4$ and (1,4- PDA)$PbBr_4$ show very broad emission peaks centered, respectively, at 650 nm and at 565 nm, with FWHM of hundreds of nm. While the absorption edge of these materials remains in the blue region, their PL shows a very large Stokes shift uncharacteristic of excitonic emission, resulting in bright white or yellow light emission. Such bright and broadband emission is typical of highly distorted 2D materials, where

excitonic recombination is mediated by defects or self-trapping resulting in a significant red shift and broadening of the PL peak.[17,20]

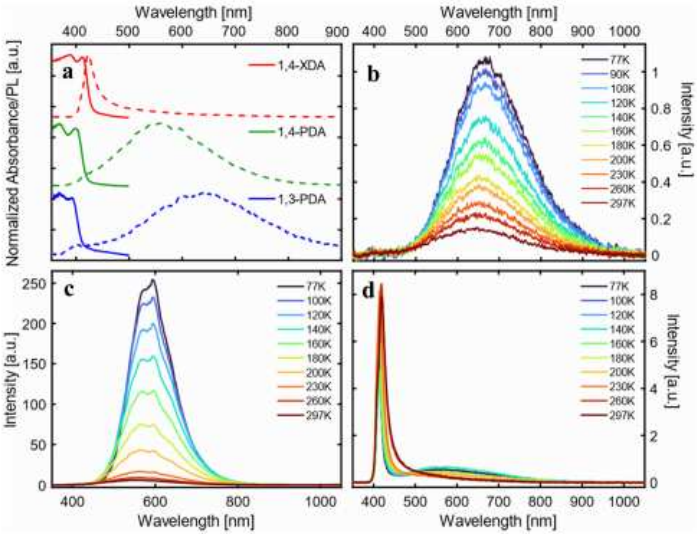

Figure 68 *(a) Absorption (solid lines) and PL (dashed lines) spectra of (1,3-PDA)PbBr₄ (blue line), (1,4-PDA)PbBr₄ (green line) and (1,4-XDA)PbBr₄ (red line) at 297K. (b)–(d) Temperature-dependent photoluminescence spectra of: (b) (1,3-PDA)PbBr₄, (c) (1.4-PDA)PbBr₄, (d) (1,4-XDA)PbBr₄. All spectra are acquired using an excitation wavelength, λ_{exc}, at 355 nm between 77 and 297 K.*

To better understand the nature of the photoluminescence, we measured temperature-dependent PL spectra between 77 and 297 K (Figures 68b-d). The two samples with a higher (and similar) degree of distortion, (1,3-PDA)$PbBr_4$ and (1,4- PDA)$PbBr_4$, show a similar trend, with a bright and broad feature dominating the emission at all considered temperatures; intriguingly a small narrow feature appears at 420 nm for (1,3-PDA)$PbBr_4$ while cooling down. While hard to identify in static PL measurements due to its comparatively low intensity, this feature is particularly prominent in the first few picoseconds of emission: its spectrum is highlighted in Figure 70 (inset).

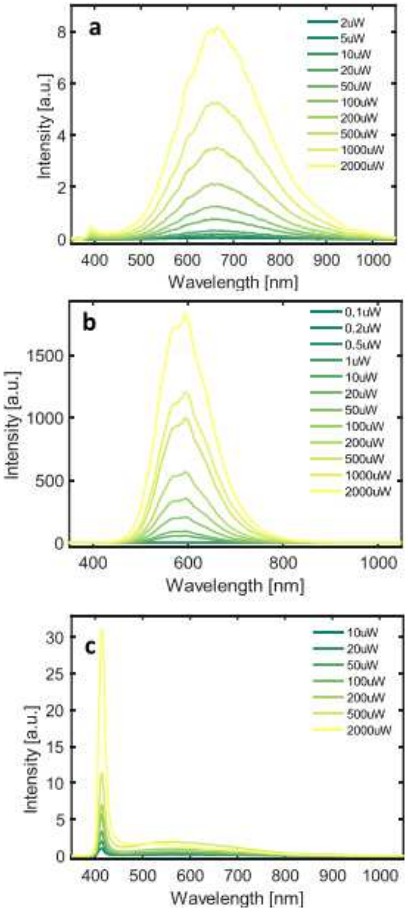

Figure 69 *Fluence-dependent photoluminescence spectra at 77K of: a)1,3-PDA b)1,4-PDA c)1,4- XDA. All spectra are recorded using λex of 355nm pulsed laser (1Khz).*

At lower temperatures, luminescence efficiency of (1,4-PDA)$PbBr_4$ is boosted. In (1,4-XDA)$PbBr_4$, the PL is still dominated by the narrowband emission at 420 nm, with broad band emission centered at around 575 nm arising as the temperature decreases.

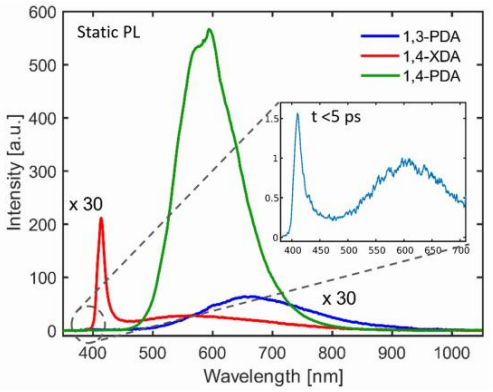

Figure 70 *Comparison between static photoluminescence spectra at 77K. Inset: spectrum of 1,3-PDA at 77K during the first 5 ps of emission (retrieved from high resolution time resolved data), highlighting the feature at 420 nm which is particularly prominent at early decays.*

Significant insight into the relationship between light emission and structural parameters can be gleaned from a more careful analysis of the temperature dependence of the PL. First of all, we analyze the temperature dependence of the integrated PL intensity (Figure 71a), integrating the broadband emission, *i.e.* the broad emission of (1,3-PDA)$PbBr_4$ (450–1000 nm), (1,4-PDA)$PbBr_4$ (400–900 nm), and (1,4-XDA)$PbBr_4$ (500–1000 nm). For all three materials, the PL intensity decreases from 77 K to room temperature, suggesting the presence of thermally activated non-radiative recombination channels which compete with radiative excitonic recombination. For all three materials, we fit the data with an Arrhenius curve to estimate the activation energy for non-radiative recombination pathways. The obtained activation energies are $\Delta E_{1,4\text{-PDA}}$ = 95 meV, $\Delta E_{1,3\text{-PDA}}$ = 39 meV and $\Delta E_{1,4\text{-xDA}}$ = 71 meV. We note that in the case of (1,4-XDA)$PbBr_4$, the recombination channel might be back transferred to the excitonic state, which indeed is the brightest emissive feature for this material. A higher value of ΔE is desirable for photoluminescence application, indicating a PL more stable at room temperature. Indeed, (1,4-PDA)$PbBr_4$ shows a large ΔE and consistently shows a very promising intense luminescence.[21]

We then consider the variation of the luminescence band width, estimated by fitting the main emission component (at 650 nm and 550 nm) for (1,3-PDA)$PbBr_4$ and (1,4-PDA)$PbBr_4$, respectively, and at 420 nm for (1,4-XDA)$PbBr_4$ with a Gaussian and taking its FWHM (Figure 71b). The broad luminescence of (1,4-XDA)$PbBr_4$ is not considered in this analysis as its superimposition to the narrow component makes it hard to isolate correctly, especially at higher temperatures.

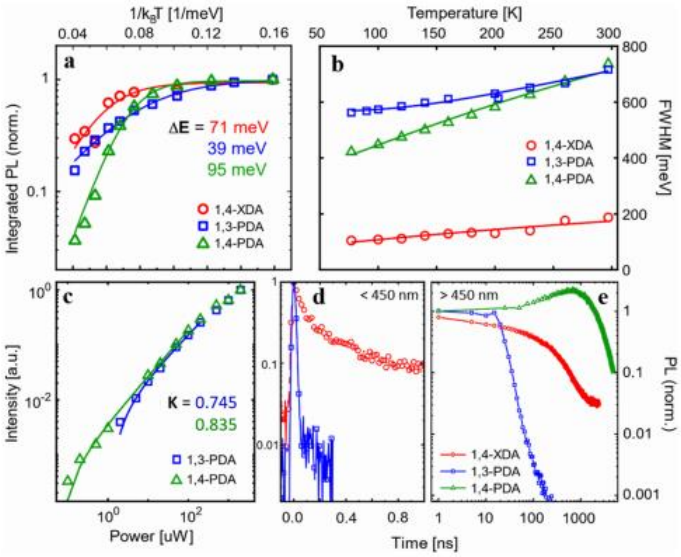

Figure 71 *(a) Integrated PL intensity and (b) FWHM as a function of temperature, measured under pulsed excitation (1 kHz) at λexc =355 nm. (c) Fluence dependence of the integrated PL intensity at 77 K fitted with a power law (d and e) Time-resolved photoluminescence measured for the (d) narrow band components (<450 nm) and (e) broad emission (>500 nm). The fast decays of excitonic features are measured with ps resolution up to 1 ns, while the long-lived broad emission is acquired up to a window of 10 μs.*

The PL FWHM can be used to evaluate the coupling of the carriers - excitons in this case - with phonons by fitting the FWHM trend *vs.* temperature with eqn (1), thus obtaining the Huang-Rhys factor and the energy of the involved phonons.[22-24]

$$\mathrm{FWHM}(T) = 2.36\sqrt{S}E_{\mathrm{ph}}\sqrt{\coth\frac{E_{\mathrm{ph}}}{2k_{\mathrm{B}}T}} \qquad (1)$$

Here, S is the Huang-Rhys factor and E_{ph} is the phonons energy. A large value of S is related to a significant degree of a carrier-phonon coupling, indicative of either emission by STEs or phonon-mediated detrapping and radiative recombination. Indeed, for the two samples with broadband emission, (1,3-PDA)$PbBr_4$ and (1,4-PDA)$PbBr_4$, we obtain, respectively, S = 39.09 and S = 131.6. For the excitonic component of (1,4-XDA)$PbBr_4$, on the other hand, we obtain S =8.58 with E_{ph} = 12.12 meV. The values of S > 10 have been associated with the presence of STEs in perovskites and organic materials: in the broadband emitters, the coupling between phonons and carriers is compatible with the formation of self-trapped excitons which can explain the broad emission from these samples.[24-26] In particular, the bright (1,4-PDA)$PbBr_4$ has the largest Huang-Rhys factor, indicating very efficient coupling with phonons with E = 13 meV. On the contrary, the value of S extrapolated for the last sample (1,4-XDA)$PbBr_4$ is small, which agrees with an emission due to the recombination of free excitons.

Further indication of the nature of the broad emission comes from the pump fluence dependence of PL (Figure 69).

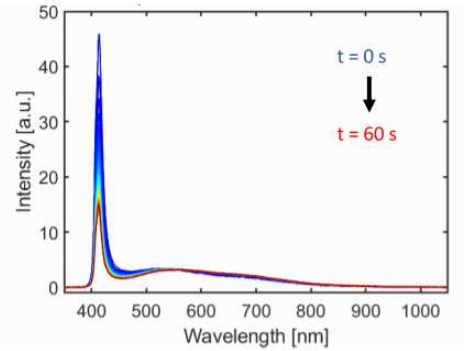

Figure 72 *1,4-XDA PL evolution in time using a λex of 355nm pulsed laser (1Khz) at 2000 uW.*

Fitting the intensity of emission in the function of the incident power with a power law $I = P^K$, we estimate exponential K (Fig. 8c): the values $K_{1,3\text{-PDA}}$ = 0.745 and $K_{1,4\text{-PDA}}$ = 0.835, lower than 1, indicate a recombination pathway mediated by defects leading to the formation of self-trapped excitons.[17,27,28] A purely excitonic recombination on the other hand is expected to yield a power dependence with K = 1. However, it is not possible to compare this power law with the narrow emission of (1,4-XDA)$PbBr_4$: its small Stokes shift results in significant reabsorption in powdered single crystal samples, distorting the measured spectrum. Furthermore, while (1,3-PDA)$PbBr_4$ and (1,4-PDA)$PbBr_4$ have remarkably photostable emissions, (1,4- XDA)$PbBr_4$ is unstable under prolonged intense illumination, even on a scale of a few seconds (Figure 72). The excitonic component decreases faster than the broad emission, making a fluence dependence measurement unreliable.

To validate the idea of different origins for the emission of the samples, we performed time-resolved photoluminescence (trPL) measurement at 77 K. To better show the disparate dynamics of the narrow- and broadband PL features, we measured trPL in different time ranges: high resolution decays in a time range < 1 ns (Figure 71d) where the excitonic decay is fully resolved are coupled with measurements up to 10 µs (Figure 71e) to fully record the decay of the broadband components. The detailed setup of both high resolution and long temporal window measurements are found in the Experimental methods section, while the complete trPL maps in both regimes is reported in Figure 73. In sample (1,4-XDA)$PbBr_4$, the difference between the excitonic and broad emission is stark: while the excitonic component at 410 nm decays in τ =76 $\pm$ 2 ps, in line with the expected excitonic lifetimes at 77 K, the decay rate of the broad emission is 3 orders of magnitude slower (τ = 180 ns) which is compatible with a trap- or phonon-mediated process, with a consequent redshift of the PL emission.

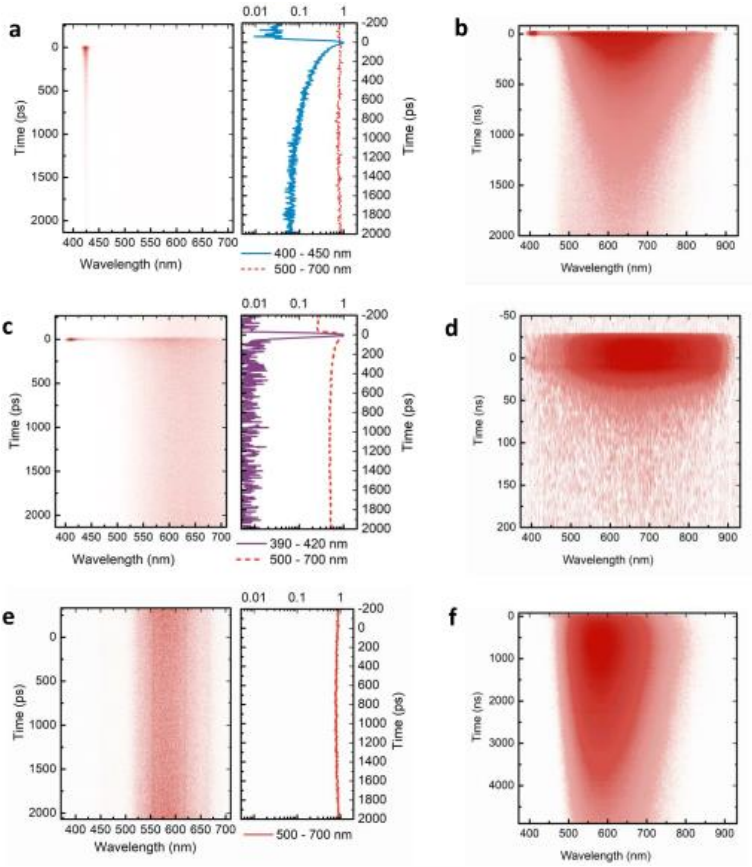

Figure 73 *Time resolved spectra in ps (left) and ns (right) time range of sample a,b) 1,4-XDA c,d) 1,3-PDA and e,f) 1,4-PDA.*

Sample (1,3-PDA)$PbBr_4$ also shows a long-lived lifetime for its broad emission at 650 nm (τ = 8.5 ns). Interestingly, in the high-resolution time-resolved measurement, we also observe a narrowband component centered at 420 nm (FWHM = 20 nm), which has a very low intensity in the static PL measurements. This is related to its extremely short lifetime, which is shorter than the response function of instruments indicating t < 3.5 ns:

such rapid PL decay, coupled with the very low total intensity of this narrow band emission, points to emission from free exciton recombination that is swiftly quenched by transfer to states with red-shifted emission. The lifetime of both narrow and broad emission of (1,3-PDA)$PbBr_4$ is almost an order of magnitude faster than the one of the samples (1,4-XDA)$PbBr_4$: this is an indication, supported also by the brighter emission and higher activation energy for non- radiative pathways of the latter, that fast non-radiative recombination is the dominant mechanism in (1,3-PDA)$PbBr_4$.

Lastly, the sample (1,4-PDA)$PbBr_4$, as in the static measures, shows only a broadband emission which presents a decay characterized by a late rise in the intensity (about 1000 ns) followed by a long decay over tens of μs. This could be an indication of a complete and efficient energy transfer from the higher energy-free exciton to a red-shifted self-trapped exciton with an efficient radiative recombination mechanism, which prevents any radiative excitonic recombination to be observed even on fast timescales. Consistently, this sample has the highest ΔE ($\Delta E_{1,4\text{-PDA}}$ = 95 meV) between the analyzed samples leading to photoluminescence dominated by radiative recombination of carriers both at room temperature and cryogenic temperature. The late rise in PL intensity suggests a back transfer mechanism from the non-radiative recombination sites to the radiative one, resulting in delayed luminescence; this feature is not present in (1,3-PDA)$PbBr_4$ decay which emission is, in fact, dominated by non-radiative pathways, from which a back transfer to the radiative state is hindered.

As we have shown with both static and time-resolved photo-luminescence spectroscopy at 77 K, the three materials which form 2D Dion–Jacobson phases all exhibit a broadband emissive component with hundreds of nanometers of bandwidth and a significant shift (100 to 150 nm) from the absorption edge. Such broad emission, as indicated by the analysis of the power and temperature dependence of the PL, can be attributed to trap-mediated excitonic recombination or STEs. In the case of (1,4-XDA)$PbBr_4$, the strongest emission is not the broadband component, but rather a narrowband, short-lived component characterized by a small Stokes shift, which is consistent with the radiative recombination of free excitons; at

room temperature, this narrow band feature at 420 nm is the only significant emission.

The different luminescence of the three samples can be rationalized by considering their structural characteristics. The two materials, (1,3-PDA)$PbBr_4$ and (1,4-PDA)$PbBr_4$, with larger values of σ^2 and λ_{oct} (Figure 67), show a dominant role in the broadband emission, as expected in materials with significant deviations from ideal octahedral geometry.[20] On the other hand, (1,4-XDA)$PbBr_4$, which has relatively undistorted octahedra, but shows significant tilting of the Pb-Br-Pb angle (< 150°), exhibits a mixture of narrow and broad band emission, with only the free exciton component persisting at room temperature.[27] However, it is interesting to note that the respective degrees of inter- and intra-octahedral distortion are not sufficient to fully explain the luminescence properties we have observed. In particular, (1,3-PDA)$PbBr_4$ has a highly distorted geometry, very similar to (1,4-PDA)$PbBr_4$ in terms of the most commonly used short-hands for octahedral distortion: their values of λ_{oct}, σ^2 and D_{tilt} are comparable. However, (1,3-PDA)$PbBr_4$ also shows a small narrowband component at 420 nm, which is quickly transferred (< 3 ps) to the broadband feature, but not before radiative-free exciton recombination can occur. No such feature is observed for (1,4-PDA)$PbBr_4$: this behaviour may indicate a much more effective transfer to the broadband emissive states which completely overtakes radiative recombination. It should also be noted that (1,3-PDA)$PbBr_4$ is significantly less emissive than its 1,4 counterpart, pointing to a larger contribution from traps acting as non-radiative recombination centers.

Conclusions

In this study we extended the family of DJ halide perovskite containing diammonium cations, by preparing, solving the structure, and characterizing novel lead bromide materials containing 1,3-phenylenediammonium (1,3-PDA), 1,3-xylylenediammonium (1,3-XDA), 1,4-phenylenediammonium (1,4-PDA), and 1,4-xylylenediammonium (1,4-XDA) cations. We showed that the

choice of the organic cation has a great influence on the topology of the structure, determining whether the layered perovskite structure can occur or not. Consistently, the degree of freedom of the organic cation deeply affects the interactions with the inorganic framework, influencing octahedral distortions and thus the optical properties of the compounds. Thanks to detailed structural and optical characterizations, we could link the differences in the optical properties, such as the nature of luminescence, to the structural parameters. In fact, samples with a high degree of distortion (containing the 1,3-PDA and 1,4-PDA cations), *i.e.* with larger values of σ^2 and λ_{oct}, show a dominant role in the broadband emission, while the presence of relatively undistorted octahedra when 1,4-XDA cation is the spacer leads to a mixture of narrow and broadband emission. However, the difference in optical properties, and in particular in the intensity of the emission, cannot be completely explained based on common and traditionally used parameters of the distortion in the octahedral layers. This finding suggests that further investigation into the relationship between structural properties and broadband luminescence in low-dimensional perovskites containing diammonium cations would be needed to identify precise design rules allowing development of efficient perovskite-based broadband and white light emitters.

References

1. A. Dučinskas, G. C. Fish, M. A. Hope, L. Merten, D. Moia, A. Hinderhofer, L. C. Carbone, J.-E. Moser, F. Schreiber, J. Maier, J. V. Milic and M. Grätzel, *J. Phys. Chem. Lett.*, 2021, 12, 10325-10332.
2. L. Gao, X. Li, B. Traoré, Y. Zhang, J. Fang, Y. Han, J. Even, C. Katan, K. Zhao, S. Liu and M. G. Kanatzidis, *J. Am. Chem. Soc.*, 2021, 143, 12063-12073.
3. L. Dobrzycki and K. Woźniak, *CrystEngComm*, 2008, 10, 577-589.
4. X. Li, J. M. Hoffman and M. G. Kanatzidis, *Chem. Rev.*, 2021, 121, 2230–2291.

5. K. Du, Q. Tu, X. Zhang, Q. Han, J. Liu, S. Zauscher and D. B. Mitzi, *Inorg. Chem.*, 2017, 56, 9291-9302.
6. A. Lemmerer and D. G. Billing, *CrystEngComm*, 2012, 14, 1954-1966.
7. A. Lemmerer and D. G. Billing, *Acta Crystallogr., Sect. C: Cryst. Struct. Commun.*, 2006, 62, m597-m601.
8. M. K. Rayner and D. G. Billing, *Acta Crystallogr., Sect. E: Struct. Rep. Online*, 2010, 66, m660.
9. M. D. Smith, A. Jaffe, E. R. Dohner, A. M. Lindenberg and H. I. Karunadasa, *Chem. Sci.*, 2017, 8, 4497-4504.
10. K. Robinson, G. V. Gibbs and P. H. Ribbe, *Science*, 1971, 172, 567-570.
11. T. Steiner, *Acta Crystallogr., Sect. B: Struct. Crystallogr. Cryst. Chem.*, 1998, 54, 456-463.
12. L. Brammer, E. A. Bruton and P. Sherwood, *Cryst. Growth Des.*, 2001, 1, 277-290.
13. L. Gao, X. Li, B. Traoré, Y. Zhang, J. Fang, Y. Han, J. Even, C. Katan, K. Zhao, S. Liu and M. G. Kanatzidis, *J. Am. Chem. Soc.*, 2021, 143, 12063-12073.
14. A. V. Marenich, S. V. Jerome, C. J. Cramer and D. G. Truhlar, *J. Chem. Theory Comput.*, 2012, 8, 527-541.
15. R. S. Mulliken, *J. Chem. Phys.*, 1955, 23, 1833-1840.
16. S. Krishnamurthy, R. Naphade, W. J. Mir, S. Gosavi, S. Chakraborty, R. Vaidhyanathan and S. Ogale, *Adv. Opt. Mater.*, 2018, 6, 1800751.
17. B. Febriansyah, T. Borzda, D. Cortecchia, S. Neutzner, G. Folpini, T. M. Koh, Y. Li, N. Mathews, A. Petrozza and J. England, *Angew. Chem., Int. Ed.*, 2020, 59, 10791-10796.
18. X. Li, X. Lian, J. Pang, B. Luo, Y. Xiao, M.-D. Li, X.-C. Huang and J. Z. Zhang, *J. Phys. Chem. Lett.*, 2020, 11, 8157-8163.
19. B. Febriansyah, D. Giovanni, S. Ramesh, T. M. Koh, Y. Li, T. C. Sum, N. Mathews and J. England, *J. Mater. Chem. C*, 2020, 8, 889-893.
20. D. Cortecchia, J. Yin, A. Petrozza and C. Soci, *J. Mater. Chem. C*, 2019, 7, 4956-4969.

21. H. Peng, Y. Tian, X. Wang, T. Huang, Z. Yu, Y. Zhao, T. Dong, J. Wang and B. Zou, *ACS Appl. Mater. Interfaces*, 2022, 14, 12395-12403.
22. W. Stadler, D. M. Hofmann, H. C. Alt, T. Muschik, B. K. Meyer, E. Weigel, G. Müller-Vogt, M. Salk, E. Rupp and K. W. Benz, *Phys. Rev. B: Condens. Matter Mater. Phys.*, 1995, 51, 10619-10630.
23. R. Zeng, L. Zhang, Y. Xue, B. Ke, Z. Zhao, D. Huang, Q. Wei, W. Zhou and B. Zou, *J. Phys. Chem. Lett.*, 2020, 11, 2053-2061.
24. K. M. McCall, C. C. Stoumpos, S. S. Kostina, M. G. Kanatzidis and B. W. Wessels, Chem. Mater., 2017, 29, 4129-4145.
25. J. Luo, X. Wang, S. Li, J. Liu, Y. Guo, G. Niu, L. Yao, Y. Fu, L. Gao, Q. Dong, C. Zhao, M. Leng, F. Ma, W. Liang, L. Wang, S. Jin, J. Han, L. Zhang, J. Etheridge, J. Wang, Y. Yan, E. H. Sargent and J. Tang, *Nature*, 2018, 563, 541-545.
26. H. Peng, S. Yao, Y. Guo, R. Zhi, X. Wang, F. Ge, Y. Tian, J. Wang and B. Zou, *J. Phys. Chem. Lett.*, 2020, 11, 4703-4710.
27. M. D. Smith and H. I. Karunadasa, *Acc. Chem. Res.*, 2018, 51, 619-627.
28. T. Schmidt, K. Lischka and W. Zulehner, *Phys. Rev. B: Condens. Matter Mater. Phys.*, 1992, 45, 8989-8994.

5.2 Lead chloride perovskites based on diammonium cations

We tried to expand the family of compounds containing diammonium cations, by synthetizing and characterizing chloride samples containing four diammonium cations, namely 1,3-phenylenediammonium (1,3-PDA), 1,3-xylylenediamimonium (1,3-XDA), 1,4-phenylenediammonium (1,4-PDA), and 1,4-xylylenediamimonium (1,4-XDA). The resulting bright white materials crystallize in monoclinic and orthorhombic space group, as detailed in Table 6.

Table 6 *Crystal structure data for $APbCl_4$ samples (A= 1,3-PDA, 1,3-XDA, 1,4-PDA, and 1,4-PDA).*

Sample	**Chemical formula**	**Space group, lattice volume ($Å^3$)**	***a*,*b*,*c* (Å)**	**α, β, γ (°)**
(1,3-PDA)$PbCl_4$	(1,3-$C_6H_{10}N_2$)$PbBr_4$	P2/*c* Monoclinic 1223.18(13)	20.4867(11) 8.4386(5) 7.0834(5)	90 92.735(6) 90
(1,3-XDA)$_2PbCl_6$	(1,3-$C_8H_{14}N_2$)$_2PbCl_6$	*P*2$_1$/*c* Monoclinic 1192.13(13)	10.5995(7) 13.8588(7) 8.3131(5)	90 102.518(7) 90
(1,4-PDA)Pb_2Cl_6	(1,4-$C_6H_{10}N_2$)Pb_2Cl_6	*P*2$_1$/*c* Monoclinic 777.53(8)	13.7789(8) 7.8328(4) 7.4805(4)	90 105.622(6) 90
(1,4-XDA)$PbCl_4$	(1,4-$C_8H_{14}N_2$)$PbCl_4$	*Pnma* Orthorhombic 1467.31(10)	7.7006(3) 24.3807(9) 7.8154(3)	90 90 90

Lead bromide perovskites and perovskite derivative containing these diammonium cations have already been reported to show interesting physical properties.[1,2] They also display a wide structural variability, giving raise to different topologies. In fact, a layered perovskite structure does not always occur when the organic cation is ditopic. With linear cations, only even-membered alkyl chains can give layered perovskite-type hybrid structures, whereas odd-membered chains cannot.[3] Moreover, cations with

fused aromatic rings generate the layered perovskite structure only when the cation is able to tilt and give hydrogen bond to the halides.[3] In general, the flexibility of the cations seems to be of great importance, as aromatic cations bearing ammonium groups with no degree of freedom tend to occur in 1D motifs. This is the case for 4,4'-MDAPbI_4 [MDA=methylenedianilinium ($H_3NC_6H_4CH_2C_6H_4NH_3$)][3], (1,4-PDA)PbI_4[4], which sounds particularly interesting, since a similar but asymmetric diammonium cation (DPDA=*N*,*N*-dimethylphenylene-*p*-diamine, $C_8H_{14}Br_4N_2$) can form both a layered structure with both the iodide and bromide (DPDA)PbX_4 (X = Br, I), and a 1D perovskite derivative with the iodide, $(DPDA)_2PbI_5 \cdot I$, under different stoichiometric conditions.[5] A layered perovskite structure was reported for (1,3-PDA)$PbBr_4$, (1,4-PDA)$PbBr_4$, (1,4-XDA)$PbBr_4$[1], together with (1,3-PDA)PbI_4[2], and (AEA)$PbBr_4$[6]. Chloride compounds are not an exception. Indeed, the investigated compositions show different structure types, as depicted in Figure 74.

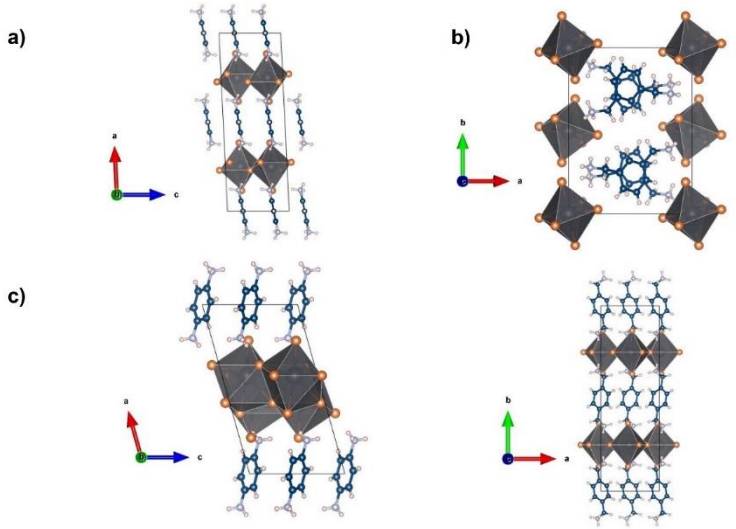

Figure 74 *Crystal structures of a) (1,3-PDA)$PbCl_4$, b) (1,3-XDA)$_2PbCl_6$, c) (1,4-PDA)Pb_2Cl_6, d) (1,4-XDA)$PbCl_4$.*

$(1,3\text{-XDA})_2PbCl_6$ does not display a layered structure but corresponds to a so-called 0D perovskitoid being constituted by isolated octahedra. Notably, it is isostructural to $(1,3\text{-XDA})_2PbBr_6$[1] suggesting that the 1,3-XDA cation may have a large tendency to give this topology. Such a structure type is probably not common with diammonium cations, even if other chloride containing 0D systems have been reported in the past.[7] $(1,4\text{-PDA})PbCl_4$ shows a layered structure, with an inorganic layer made of face-sharing square antiprisms and a layer of organic cations located on the inversion center. The central Pb atom is eight-coordinate with Pb–Cl distances ranging from 2.8029(18) to 3.3869(15), creating a distorted square antiprism. The structure described in this work is highly consistent with previous findings[7,8], for which structural data were not mentioned. On the other hand, $(1,3\text{-PDA})PbCl_4$ and $(1,4\text{-XDA})PbCl_4$ crystallize as Dion-Jacobson (DJ) phases with n=1, according to the general formula $A'A_{n-1}M_nX_{3n+1}$, comprising layers of $PbCl_6$ octahedra separated by layers of organic cations.

The experimental XRD powder patterns obtained are reported in Figure 75, superimposed to the calculated patterns from the single crystal XRD data.

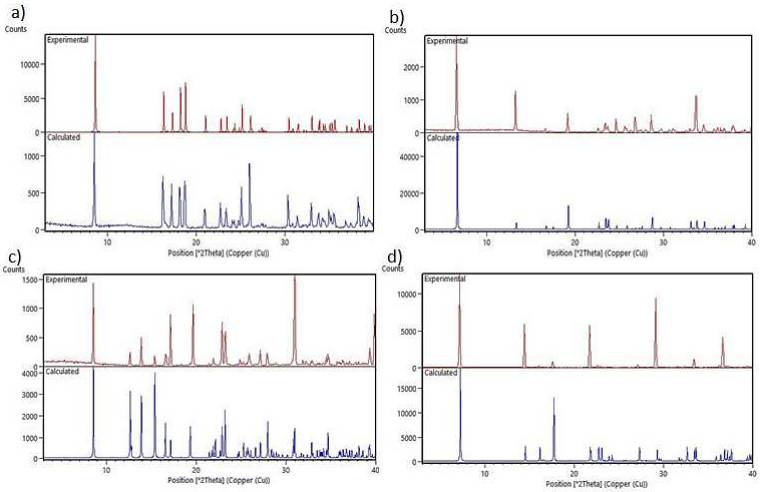

Figure 75 XRD powder patterns (red) of a) *$(1,3\text{-PDA})PbCl_4$, b) $(1,3\text{-XDA})_2PbCl_6$, c) $(1,4\text{-PDA})Pb_2Cl_6$, d) $(1,4\text{-XDA})PbCl_4$ superimposed to the calculated patterns from SC-XRD (blue).*

It is well known that the interaction between the ammonium group and the octahedral framework deeply affects the structure and properties of layered perovskites.[10,11] An useful parameter to unveil this effect is the penetration depth, meant as the distance between the N atom of the amino group and the plane of the terminal halides.[9] Consistently with what was stated for their bromide counterparts[1], the NH_3^+ penetration seems to influence both the inter-octahedral, in terms of the X-Pb-X angle, and intra-octahedral, such as the octahedral elongation length ($\langle\lambda_{oct}\rangle$) and the bond angle variance (σ^2_{oct})[10], distortion parameters. In particular, considering the bromide and chloride containing phenylamines reported so far, some general trends can be envisaged (Figure 76).

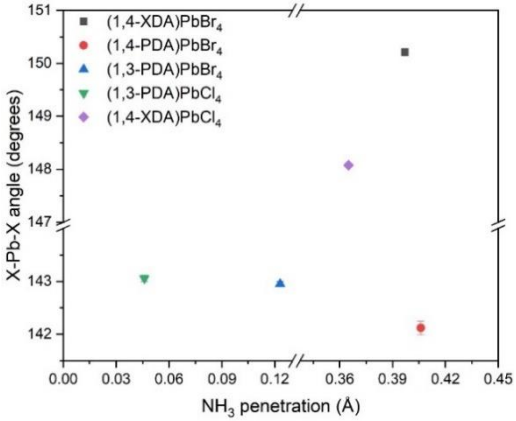

Figure 76 *Variation of the Pb-X-Pb bond angle as a function of NH_3 penetration.*

With the same organic cation, the penetration depth increases from the chloride to the bromide[9], probably as a consequence of the different strength of the hydrogen bond.[11,12] The position and length of the substituents seems to play a pivotal role; 1,3 cations have shorter depth of penetration, most likely because of the steric hindrance of the relatively close substituents, while the 1,4 cations show larger penetration and more

regular octahedral layers. Among them, 1,4-PDA give rise to the largest tilt, because, being short and rigid, it has less degrees of freedom, while the 1,4-XDA cations has longer substituents that can more easily interact with the halide.

Similar yet opposite trends can also be seen in the intra-octahedral distortion parameters (Figure 77).

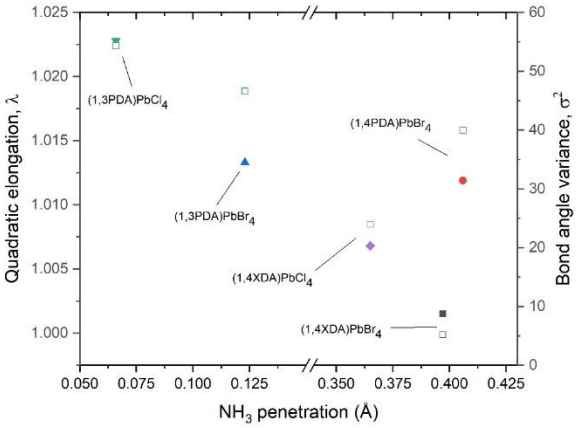

Figure 77 *Octahedral elongation and bond angle variance as a function of NH_3 penetration for the compounds with a layered perovskite structure.*

In fact, the 1,3 cations have small NH_3 penetration, but give rise large distortions within the octahedra. Among the 1,4 cations, the rigidity of 1,4-PDA again seems to affect the PbX_6 octahedra, inducing a distortion close to that found for the 1,3 cations. On the other hand, the more flexible 1,4-XDA cations allow for more regular octahedra. When the same organic cation is involved, the distortion within the octahedra increases from Br to Cl, thus with the hardness of the anion, as predicted by first-principles calculations[13] and shown by local structure studies[14].

In order to have further insight on the role of the flexibility of the organic cation, we can extend the analysis of the intra-octahedral distortion to

include the compounds in which the layered perovskite structure does not occur (Figure 78).

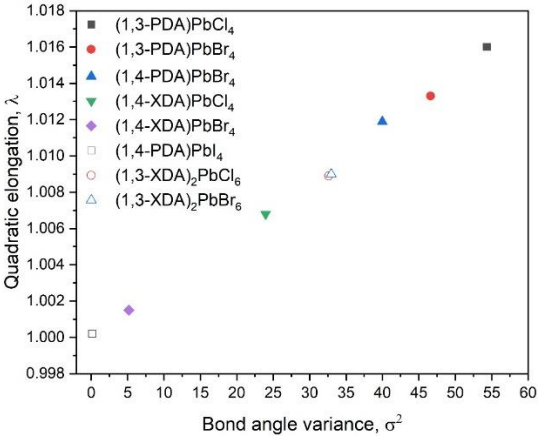

Figure 78 *Distortion parameters for the newly synthesized compounds and already reported materials with similar characteristics.*

It is worth noting that the smallest distortion is shown by (1,4-PDA)PbI_4 where the symmetry, together with the edge sharing motif present in the structure[3], gives rise to regular octahedra. Then the XDA cations undergo an increasing distortion, with 1,3-XDA cations generating a larger yet very close distortions, supporting the idea that the 0D arrangement is mostly due to the type of organic cation. The more rigid PDA cations, and in particular the 1,3 ones, induce the largest distortions within the octahedra. Furthermore, as already pointed out, the distortion increases along with the hardness of the halide.

To conduct a better investigation of the correlation between the octahedral distortion degree and optical properties of these materials, we performed static absorbance and photoluminescence (PL) measurements at room temperature, as reported in Figure 79.

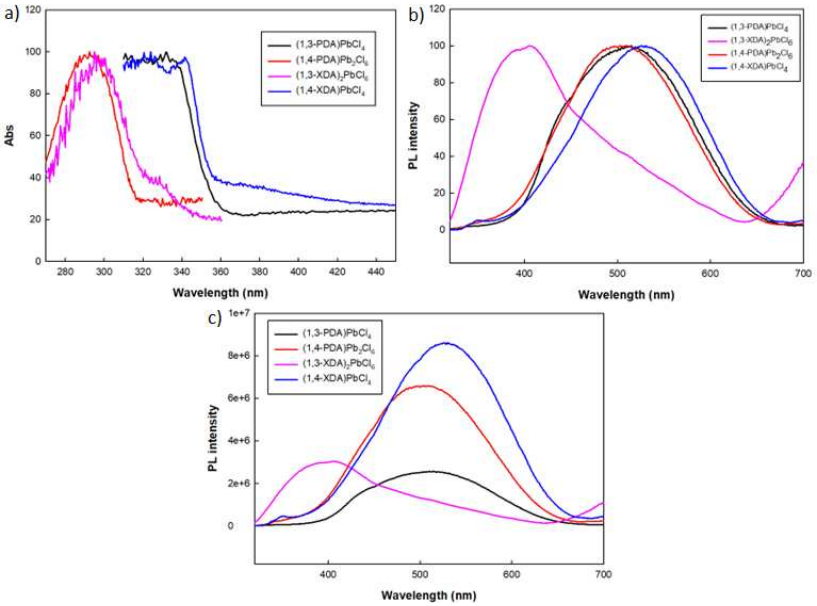

Figure 79 *a) Normalized optical absorbance, b) normalized steady-state PL (λ_{exc}=300 nm) and c) non-normalized PL spectra of (1,3-PDA)$PbCl_4$, (1,3-XDA)$_2PbCl_6$, (1,4-PDA)Pb_2Cl_6 and (1,4-XDA)$PbCl_4$.*

Figures 79a and 79b show the comparison among the normalized absorption and the normalized PL spectra for (1,3-PDA)$PbCl_4$, (1,3-XDA)$_2PbCl_6$, (1,4-PDA)Pb_2Cl_6, (1,4-XDA)$PbCl_4$, while the non-normalized PL curves are reported in Figure 79c.

The wide band gap of the four samples, calculated from Tauc plots by considering a direct nature of the gap, corresponds to similar values for (1,3-PDA)$PbCl_4$ and (1,4-XDA)$PbCl_4$ (3.53 eV and 3.51 eV, respectively), while 3.92 eV is detected for (1,4-PDA)Pb_2Cl_6 and 3.87 eV for (1,3-XDA)$_2PbCl_6$. For all the samples, the static absorbance reveals an absorption edge quite close to the UV range, between 300 - 340 nm for 1,4-PDA and 1,3-XDA cations and between 340 - 380 nm for the other two spacers. As expected, a shift towards lower wavelengths is observed for the chloride compounds with

respect to the corresponding 2D lead bromide perovskites.[1] Only (1,4-XDA)$PbCl_4$ shows a narrow absorption peak on top of the band edge, which usual emerges in low-temperature measurements, and typical of the important quantum confinement effect of these 2D materials.[15] The static PL spectra was collected under pulsed excitation at 300 nm and show very broad emission peaks with a full width at half maximum (FWHM) of hundreds of nm, unlike it was expected from excitonic photoluminescence. The comparison of the non-normalized PL spectra, as reported in Figure 79c, highlights the most intense emission of (1,4-PDA)Pb_2Cl_6 and (1,4-XDA)$PbCl_4$, while a moderate PL intensity was revealed for the other two materials. $(1,3\text{-XDA})_2PbCl_6$ presents the relatively narrowest peak (~130 nm) centered at 405 nm with a shoulder suggesting the existence of a second PL contribute and with the lowest Stokes shift of ~105 nm. On the contrary, the remaining three samples show a broader emission peak (FWHM between 155 and 165 nm) centered 528 nm, 510 nm and 505 nm, respectively for (1,4-XDA)$PbCl_4$, (1,3-PDA)$PbCl_4$ and (1,4-PDA)Pb_2Cl_6, with greater Stokes shifts close to 200 nm. In general, this large Stokes shift is uncharacteristic of excitonic emission; however, previous studies have confirmed that both such broadband emission, resulting in bright white light, and the pronounced Stokes shift, are due to self-trapping mechanisms occurring in the excitonic recombination of 2D materials with a high degree of octahedral distortion.[16,17]

Conclusions

In the present study, four novel lead chloride perovskites containing diammonium spacer cations have been reported. We confirmed that the selection of the organic spacer plays a pivotal role in the formation of layered perovskite structures, often resulting in 1D or 0D structural motifs instead of the 2D topology. We also proved, through the evaluation of appropriate structural distortion parameters, that the flexibility of the organic cation and its degree of freedom strongly influence the interaction

with the inorganic framework. As already described for the corresponding bromide samples, this different level of interaction has a key role on the modulation of the optical properties. However, further investigations would be needed in order to provide a better explanation of optical behaviour of these systems related to the mechanisms occurring in their lattice, leading to the development of efficient broadband emitters.

References

1. Chiara, R.; Morana, M.; Folpini, G.; Olivati, A.; Albini, B.; Galinetto, P.; Chelazzi, L.; Ciattini, S.; Fantechi, E.; Serapian, S. A.; Petrozza, A.; Malavasi, L. The templating effect of diammonium cations on structural and optical properties of lead bromide perovskites: a guide to design broad light emitters. *J. Mater. Chem. C.* **2022**, 10, 12367-12376
2. Gao, L.; Li, X.; Traoré, B.; Zhang, Y.; Fang, J.; Han, Y.; Even, J.; Katan, C.; Zhao, K.; Liu, S.; Kanatzidis, M. G. *M* -Phenylenediammonium as a New Spacer for Dion–Jacobson Two-Dimensional Perovskites. *J. Am. Chem. Soc.* **2021**, *143* (31), 12063–12073.
3. Lemmerer, A.; Billing, D. G. Lead Halide Inorganic–Organic Hybrids Incorporating Diammonium Cations. *CrystEngComm* **2012**, *14* (6), 1954–1966.
4. emmerer, A.; Billing, D. G. Two Packing Motifs Based upon Chains of Edge-Sharing PbI6 Octa-hedra. *Acta Cryst C* **2006**, *62* (12), m597–m601.
5. Hautzinger, M. P.; Dai, J.; Ji, Y.; Fu, Y.; Chen, J.; Guzei, I. A.; Wright, J. C.; Li, Y.; Jin, S. Two-Dimensional Lead Halide Perovskites Templated by a Conjugated Asymmetric Diammonium. *Inorg. Chem.* **2017**, *56* (24), 14991–14998.
6. Smith, M. D.; Jaffe, A.; Dohner, E. R.; Lindenberg, A. M.; Karunadasa, H. I. Structural Origins of Broadband Emission from

Layered Pb–Br Hybrid Perovskites. *Chem. Sci.* **2017**, *8* (6), 4497–4504.

7. Dobrzycki, L.; Woźniak, K. Inorganic–Organic Hybrid Salts of Diaminobenzenes and Related Cations. *CrystEngComm* **2008**, *10* (5), 577–589.
8. Bourne, S. A.; Mangombo, Z. Phenylamines as Building Blocks to Layered Inorganic–Organic Structures. *CrystEngComm* **2004**, *6* (72), 438–442.
9. Du, K.; Tu, Q.; Zhang, X.; Han, Q.; Liu, J.; Zauscher, S.; Mitzi, D. B. Two-Dimensional Lead(II) Halide-Based Hybrid Perovskites Templated by Acene Alkylamines: Crystal Structures, Optical Properties, and Piezoelectricity. *Inorg. Chem.* **2017**, *56* (15), 9291–9302.
10. Robinson, K.; Gibbs, G. V.; Ribbe, P. H. Quadratic Elongation: A Quantitative Measure of Distortion in Coordination Polyhedra. *Science* **1971**, *172* (3983), 567–570.
11. Steiner, T. Hydrogen-Bond Distances to Halide Ions in Organic and Organometallic Crystal Structures: Up-to-Date Database Study. *Acta Crystallographica Section B* **1998**, *54* (4), 456–463.
12. Brammer, L.; Bruton, E. A.; Sherwood, P. Understanding the Behavior of Halogens as Hydrogen Bond Acceptors. *Crystal Growth & Design* **2001**, *1* (4), 277–290.
13. Waghmare, U. V.; Spaldin, N. A.; Kandpal, H. C.; Seshadri, R. First-Principles Indicators of Metallicity and Cation off-Centricity in the IV-VI Rocksalt Chalcogenides of Divalent Ge, Sn, and Pb. *Phys. Rev. B* **2003**, *67* (12), 125111.
14. Laurita, G.; H. Fabini, D.; C. Stoumpos, C.; G. Kanatzidis, M.; Seshadri, R. Chemical Tuning of Dynamic Cation Off-Centering in the Cubic Phases of Hybrid Tin and Lead Halide Perovskites. *Chemical Science* **2017**, *8* (8), 5628–5635.
15. X. Li, X. Lian, J. Pang, B. Luo, Y. Xiao, M.-D. Li, X.-C. Huang and J. Z. Zhang, *J. Phys. Chem. Lett.*, 2020, 11, 8157-8163.

16. B. Febriansyah, T. Borzda, D. Cortecchia, S. Neutzner, G. Folpini, T. M. Koh, Y. Li, N. Mathews, A. Petrozza and J. England, *Angew. Chem., Int. Ed.*, 2020, 59, 10791-10796.
17. D. Cortecchia, J. Yin, A. Petrozza and C. Soci, *J. Mater. Chem. C*, 2019, 7, 4956-4969.

CHAPTER 6.

DIPHENYL-BASED MONOAMMONIUM SPACERS

MHPs are attracting a huge interest for their possible application in heterogeneous photocatalysis following the recent synthesis of materials and heterostructures that have been found to be efficient for a plethora of photocatalyzed chemical reaction, including hydrogen generation and CO_2 reduction. [104–106] A major limitation of MHPs in photocatalysis, is their limited water-stability which derives from the high ionic character of the metal halide framework. [105,107] In this context, 2D layered MHPs may be particularly suitable to overcome this issue, in virtue of the vast range of organic spacers which can be inserted as protective barrier between the inorganic perovskite layers. [6] In fact, upon introduction of a highly hydrophobic organic spacer in the perovskite structure, a significant moisture and water stability could be achieved, and examples exist of systems forming a suspension in water instead of being dissolved. [106,108] In this respect, recently, some Bi-based and Sn-based perovskites with improved water resistance were found to show significant visible-light photocatalytic activity of hydrogen photogeneration and organic dye degradation, which was further enhanced by designing heterostructures with g-C_3N_4. [106,108] Similar strategies have been used also by other authors on the $Cs_3Bi_2I_9$ perovskite-derivative. [109] While materials engineering has been successful for the synthesis of lead-free MHPs photocatalysts, there are no reports about any photoactive germanium halide perovskite. In this respect, a recent series of Ruddlesden-Popper (RP) 2D germanium bromide perovskites (n=1), namely A_2GeBr_4 with A = phenylethylammonium (PEA), Br-phenylethylammonium (BrPEA), F-

phenylethylammonium (FPEA), and benzylammonium (BzA) showed air-stability but not water-tolerance. [3]

6.1 Air and water stable and photocatalytically active germanium-based 2D perovskites by organic spacer engineering

Purpose and scope

Photocatalytic reactions mediated by MHPs semiconductors may be the next big thing in the ever-growing exploitation scenarios of these fascinating materials. To make a real impact in this contest, advancements in the material moisture stability and toxicity are needed. We investigated novel germanium-based 2D MHPs which show an intrinsic water-stability realized through organic cation engineering. By incorporating 4-phenylbenzylammonium (PhBz) (Figure 80a) we demonstrate, by means of extended experimental and computational results, that $PhBz_2GeBr_4$ and $PhBz_4GeI_4$ can achieve a relevant air and water stability. This cation presents extended π conjugated systems, creating a unique condition in which strong intra-layer van der Waals interactions are established, substantially stabilizing the resulting bulk perovskite. The creation of composites embedding g-C_3N_4 allows to provide the first proof-of-concept for light induced hydrogen evolution from water by a 2D Ge-based MHP, thanks to the effective charge transfer at the heterojunction between the two semiconductors. These results pave the way to the intelligent design of intrinsically water stable MHPs phases which are highly demanded in all the applicative fields of MHPs.

Experimental methods

Materials preparation

$PhBz_2GeBr_4$ has been prepared by dissolving a proper amount of GeO_2 powder in HBr and H_3PO_2 gradually heating to 100°C under stirring and under nitrogen flux. After the solid dissolution, the amine is added and the reaction mixture is cooled down to room temperature obtaining the formation of the product. The same procedure has been used to prepare the iodide containing samples by changing HBr with HI. Bulk g-C_3N_4 has been synthesized from the polymerization of DCD (NH C(=NH)NHCN, Aldrich, 99%) by the following thermal treatment (under N_2 flux): heating (1°C/min) to 550°C, isothermal step for 4 hours followed by cooling to room temperature (10°C/min). Synthesis has been carried out in a partially closed alumina crucible. The $PhBz_2GeBr_4$@g-C_3N_4 composites have been prepared by adding to the DMF solution containing the perovskite the proper amount of g-C_3N_4.

Characterization

The crystal structure of the samples has been characterized by room temperature Cu-radiation XRD acquired with a Bruker D8 diffractometer. DRS spectra were acquired in the wavelength range 300-800 nm directly on the powders by using a Jasco V-750 spectrophotometer, equipped with an integrating sphere (Jasco ISV-922).

The photoluminescence (PL) measurements were recorded by means of a Fluorolog-3 spectrofluorometer (HORIBA Jobin-Yvon), equipped with a 450 W xenon lamp as exciting source and double grating excitation and emission monochromators. All the optical measurements were performed at room temperature on powder dispersed samples as-obtained from the synthesis without any size sorting treatment. The PL emission spectra were recorded by using an excitation wavelength of 375 nm.

Hydrogen evolution experiments

H_2 evolution experiments were conducted in distilled water containing 10% (v/v) triethanolamine (Aldrich, ≥ 99%), irradiated in Pyrex glass containers (28 mL capacity, 21 mL sample). After addition of the catalyst (1 g L^{-1}), the sample was deoxygenated by Ar bubbling (20 min) to obtain anoxic conditions, and irradiated under magnetic stirring for 6 hours. Chloroplatinic acid (H_2PtCl_6, 38% Pt basis), used as precursor for metallic Pt, was from Sigma-Aldrich. Since Pt is *in situ* photodeposited on the catalyst surface, after Ar bubbling a small volume from a 15 g L^{-1} H_2PtCl_6 aqueous solution was added, using a 10-100 µL micropipette, to the catalyst suspension (1 g L^{-1}) directly in the photoreactor. The latter was closed with sleeve stopper septa and was irradiated, as described in the following, achieving simultaneous Pt deposition and H_2 production. Irradiation was performed under simulated solar light (1500 W Xenon lamp, 300-800 nm) using a Solar Box 1500e (CO.FO.ME.GRA S.r.l., Milan, Italy) set at a power factor 500 W m^{-2}, and equipped with UV outdoor filter made of IR-treated soda lime glass. Triplicate photoproduction experiments were performed on all samples. The headspace evolved gas was quantified by gas chromatography coupled with thermal conductivity detection (GC-TCD). The results obtained in terms of H_2 evolution rate are expressed as µmoles of gas per gram of catalyst per hour (µmol g^{-1} h^{-1}). XRD measurements on spent catalysts have been done by filtering the suspensions and recovering the powder, which underwent diffraction measurements.

Metal leaching tests

The leaching tests were performed by dispersion of the powders in distilled water, under magnetic stirring for 4, 8, 16 and 24 h. Then the suspension was filtered on 0.2 µm nylon membrane and the amount of tin in solution was determined by ICP-OES analysis, after acidification (1% v/v ultrapure nitric acid).

Computational details

All the calculations have been performed with the CP2K code. Atom-centered Gaussian-type basis functions are used to describe the orbitals. We employ the MOLOPT[2] basis set and use a cutoff of 600 Ha for the plane waves. Core-valence interactions are described by Goedecker-Teter-Hutter pseudopotentials.

To calculate the formation energies from first-principles as reported in Eq. 2 (see below), we need to build atomistic models (i) of the considered A_2GeX_4 perovskites: PEA_2GeBr_4, $BrPEA_2GeBr_4$, $BPEA_2GeI_4$, and $BPEA_2GeBr_4$, X(ii) of GeX_2 (X=I, Br) and, (iii) of AX. For PEA_2GeBr_4 and $BrPEA_2GeBr_4$, we construct supercells starting from the experimental crystallographic structures. Then, we perform density functional theory (DFT) calculations to relax both the coordinates of the atoms and the lattice parameters. These calculations are carried out employing the rVV10 functional, which accounts for van der Waals interactions and has been found to be suited to describe the energetics of layered and 2D materials. In fact, the calculated lattice parameters for PEA_2GeBr_4 and $BrPEA_2GeBr_4$ nicely agree with those measured, with differences below 2%. To model $BPEA_2GeI_4$, we start from the experimental crystallographic structure of $BPEA_2PbI_4$[1], in which we replace Pb atoms with Ge atoms and then we fully relax both coordinates and lattice parameters. Analogously, we obtain an atomistic model of $BPEA_2PbBr_4$, by further replacing I with Br.

GeI_2 and $GeBr_2$ are analogously modelled constructing atomistic supercells from the experimentally available crystal structure: a=b=4.13 Å, c=6.75 Å, α=β=90°, γ=120° for GeI_2 and a=11.680 Å, b=9.120 Å, c=6.869 Å, α= γ=90°, β=101.9° for $GeBr_2$. For GeI_2 ($GeBr_2$), we constructed a 4x4x3 (2x2x3) supercell. For AX salts, experimental data were not available for many of them. Therefore, we considered, as a reference, the total energy of an isolated AX dimer for all considered species.

Results and discussion

The novel $PhBz_2GeBr_4$ perovskite was synthesized by means of wet-chemistry route as described above. The powder has a white colour (Figure 80b) and the corresponding high-resolution synchrotron radiation (SR) powder X-ray diffraction (XRD) pattern collected at 0.3547 Å is shown in Figure 80c.

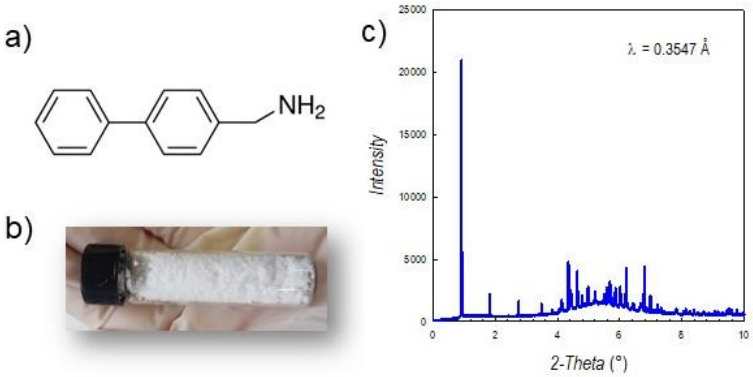

Figure 80 *(a) Sketch of the chemical formula of 4-phenylbenzylamine; (b) picture showing the appearance of the powdered sample; (c) SR-XRD pattern of $PhBz_2GeBr_4$ collected at 0.3547 Å.*

The indexing of the SR-XRD data provided an orthorhombic cell (space group $Pmc2_1$) with refined lattice parameters of a=6.0260(1) Å, b=9.1744(2) Å, c=44.376(1) Å. There are no literature reports on 2D perovskites containing 4-phenylbenzilammonium cation, therefore a direct comparison with analogous compositions cannot be posed. The most similar material reported, in terms of organic cation, is $BPEA_2PbI_4$ (BPEA = 2-(4-biphenyl)ethylamine) in which the organic cation has an ethyl linked to the amine group.[1] Even though the central metal and the halide are different with respect to $PhBz_2GeBr_4$, the concordance with the symmetry of the $BPEA_2PbI_4$ crystal suggests a similar organic spacer arrangement, as shown in Figure 81 where $PhBz_2GeBr_4$ diffraction is plotted against the expected

Bragg peaks from $BPEA_2PbI_4$. Long *c*-axis is, as well, in a similar range as that herein reported.[1]

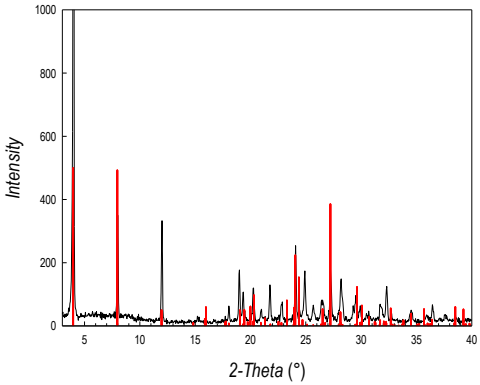

Figure 81 *Diffraction pattern (Cu-alpha radiation) of $PhBz_2GeBr_4$ against the expected Bragg peaks of $BPEA_2PbI_4$ with actual lattice parameters obtained from the indexing procedure.*

The optical properties of $PhBz_2GeBr_4$ have been determined by UV-Vis absorption spectroscopy and photoluminescence (PL), see as shown in Figures 82a and 82b. From the Tauc plot, we estimate a band gap of 3.64 eV, while the PL spectrum shows a structured intense band composed of three contributions with the main emission peak centered at about 415 nm.

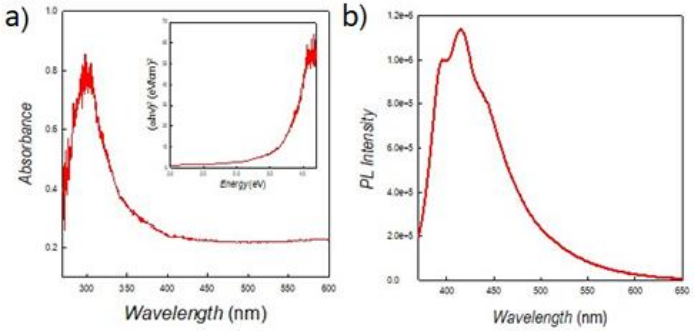

Figure 82 *(a) Absorption spectra of $PhBz_2GeBr_4$ (inset: Tauc plot); (b) PL spectra of $PhBz_2GeBr_4$.*

To test the stability vs. moisture of the synthesized material, as-prepared $PhBz_2GeBr_4$ (kept under argon in glovebox) was exposed to laboratory air (T ≈ 22°C, Relative Humidity (RH) ≈ 35%) for 2 months. The XRD pattern collected after this time interval shows a perfect match with the pattern of the as-prepared $PhBz_2GeBr_4$ (cf. red and black lines in Figure 83). Furthermore, $PhBz_2GeBr_4$ powders were dispersed in water and kept under stirring for 24 hours and the diffraction pattern of the powders was found highlyt consistent with the as-prepared material (cf. blue vs. black patterns in Figure 83).[2,3] In the rescaled inset of Figure 83, we highlighted the peaks around 10-40° to put in prominence the very optimum agreement between the patterns extending in the whole diffraction range.

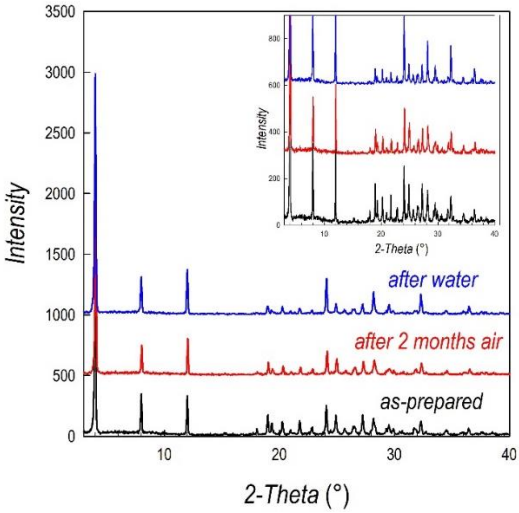

Figure 83 *XRD pattern of as-prepared $PhBz_2GeBr_4$ (black), after 2 months of air-exposure (red) and after 24 h water treatment (blue). Inset: focus on a reduced 2-theta range.*

Further evidence of water stability has been assessed through a leaching test. In this assay, $PhBz_2GeBr_4$ has been placed in water under magnetic stirring and the amount of Ge in the solution has been determined by

Inductively Coupled Plasma Optical Emission Spectroscopy (ICP-OES). After 4, 8, 16 and 24 hours of stirring the Ge amount detected in the solution was 4.3%, 5.7%, 5.9% and 6%, respectively, of the total amount of germanium present in the perovskites, thus confirming the high water-stability and insolubility of $PhBz_2GeBr_4$.

In addition to the clear evidence of air and water structural stability above reported, we applied X-ray Photoelectron Spectroscopy (XPS) on the as-prepared sample and on the sample after immersion in water. The Ge 3d spectra of the two samples reported in Figure 84 are superimposable (as for all the other elements probed, Figure 85) indicating that the Ge ions kept in immersed samples retain the same oxidation state of as-prepared materials. The relative position of the Ge3d peak suggests the possible presence of Ge(IV) on the surface of the material, possibly in the form of a native-oxide, that could act as a protective layer, as recently proposed to justify an enhanced air-stability of 2D Ge-perovskites.[4,5]

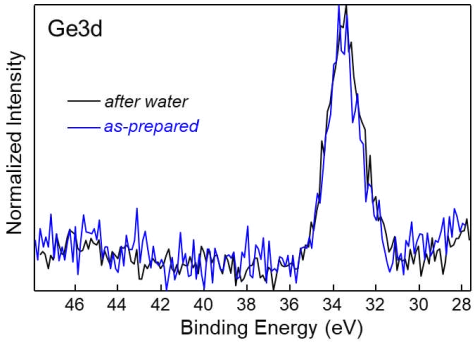

Figure 84 *Ge3d XPS spectrum of as-prepared $PhBz_2GeBr_4$ (black), and after 24 h water treatment (blue).*

More specifically, the binding energy position of the Ge 3d peaks at 33.4 eV is predictive of a Ge(IV) state, and an additional indication of the Ge(IV) oxide formation at the surface of the material derives from the curve-fit

analysis of the corresponding O1s spectra (Figure 85) revealing the presence of a component at 531.8 eV typical of GeO_2. [6,7]

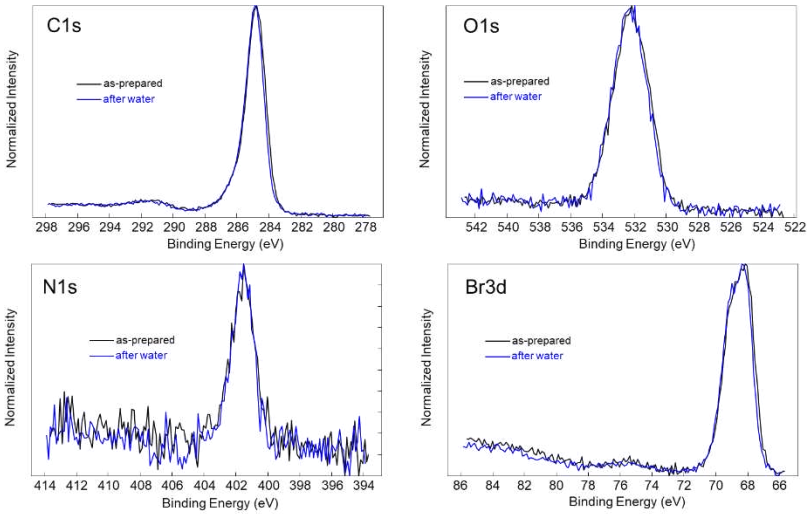

Figure 85 *XPS spectra for all the other elements probed of as-prepared $PhBz_2GeBr_4$ (black), and after 24 h water treatment (blue).*

However, since previously synthesized Ge-based 2D perovskites did not show any water-stability, the reason of the improved water-stability of $PhBz_2GeBr_4$ may lay in the bulk properties originating by the significant steric hindrance and hydrophobicity of the organic spacer.[8]

We thus exploited the advantage of $PhBz_2GeBr_4$ superior water-stability by testing its possible application in photocatalysis. Hydrogen photogeneration characteristics have been determined according to a commonly utilized protocol, already applied in our laboratory for other MHPs.[2,3,9] First, we determined the hydrogen evolution rate (HER) of pure $PhBz_2GeBr_4$ under simulated solar light, that was proven to be ~ 6 $\mu mol\, g^{-1}\, h^{-1}$, a low but relevant value for a pure MHP, also considering the relatively high band-gap of the materials, 3.6 eV, which corresponds to efficient absorption only in

the ultraviolet region of the light spectrum (in line with the UV-Vis absorption spectrum, Figure 82a). To enhance the photoactivity of the perovskite, we prepared composites with a well-known visible light-absorbing semiconductor, namely g-C_3N_4, at different weight percentages (%wt) of MHP relative to g-C_3N_4 (1%, 2.5%, 3.5%, 5% and 15%). Figure 86a reports the XRD patterns of the composites showing the main contribution of g-C3N4 up to 15wt%. We point out that the main peak of $PhBz_2GeBr_4$, located around 4°, is already detectable in the sample containing 2.5wt% of perovskite. UV-Vis spectra of the composites (Figure 86b) show a significant contribution to absorbance deriving from the carbon nitride.

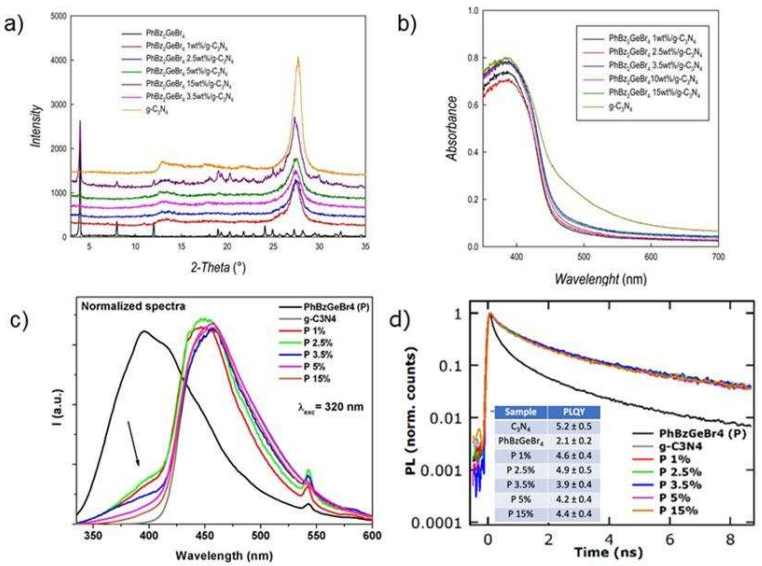

Figure 86 Structural and optical properties of $PhBz_2GeBr_4$/g-C_3N_4 composites. *a) XRD patterns of $PhBz_2GeBr_4$/g-C_3N_4 composites for different perovskite loadings; b) UV-Vis spectra of $PhBz_2GeBr_4$/g-C_3N_4 composites for different perovskite loadings. c) normalized emission spectra and of $PhBz_2GeBr_4$/g-C_3N_4 composites at different percentages of perovskite loading (wt%). g-C_3N_4 refers to pristine material. λ_{exc}=320 nm. d) normalized PL decays for the same composites (I_{exc}= 320 nm; I_{em} = 450 nm). In the inset PLQY for all samples obtained with CW excitation at 405nm.*

The normalized photoluminescence (PL) spectra of pure compounds and composites are reported in Figure 86c. Pristine materials, both, show intense luminescence band, $PhBz_2GeBr_4$ peaking at 415 nm and g-C N at 455 nm. Their bands falling in different spectral regions allow to monitor the contribution of the single components to the PL features of the composites. Noticeably the composites, when excited at a wavelength which allows the absorption of both materials, show a spread PL emission overshadowed by g-C_3N_4 contribution. Graphitic-carbon nitride emission is energetically spread spanning from 410 to 560 nm, due to various deactivation paths existing within the energy band diagram of the material.[29] The PL quantum yields (PLQY) as well as the lifetimes (τ), Figure 86d, are very similar for pristine and for g-C_3N_4 containing composites. The PLQY varies from 3.9 ± 0.4 % to 5.2 ± 0.5 % and the average τ is 9.0 ± 0.5 ns for all specimens, further suggesting the central role played by carbon nitride states in the excitation deactivation path, while the PLQY of pure $PhBz_2GeBr_4$ is lower (2.2 ± 0.2%), compatibly with the shorter PL lifetime. These observations nicely fit the band structure of the junction, modeled below. The normalized PL spectra show however some differences among the samples, while g-C_3N_4 features dominates the spectra at high perovskite-loadings suggesting a highly efficient energy transfer from perovskite moiety to g-C_3N_4, the low-loading composites show some minority features attributable to residual perovskite contribution (Figure 86). For these compositions, namely 1, 2.5 and 3.5 % loading of perovskite, the energy transfer appears somehow less effective suggesting a possible defect-filling mechanism at the g-C_3N_4/perovskite interface. An additional difference related to the shape of the composite's emission, can be found in the region of its peak (around 440-460 nm), here the g-C_3N_4 and the high loading composites show a more intense contribution at low energies, peaking their emission at 458 nm, meanwhile low loading composites (1% and 2.5%) show the maximum emission at 444 nm. The shape of the emission band in g-C_3N_4 materials can be attributed to the relative population of diverse energy transitions, withstanding a complex deactivation path for the excitation in graphitic carbon nitride materials, particularly the one at low energies are connected to π*-π

transition, meanwhile the one at high energies are related to deactivation to nitrogen atom lone pair.[10,11] In our systems the diverse shapes suggest how differences in the relative populations of excitation/deactivation processes exist between low loading and high loading composites. The peculiar optical behaviour of composites appears to be a distinctive trait of perovskite carbon nitride systems, as already described elsewhere, suggesting that low levels of perovskite doping may act on funneling the charges upon localized states.[12] Those active sites could be fundamental in boosting the photocatalytic performances of low loading composites.[12] Such effect faded with increased perovskite loadings.

Finally, we investigated the solar-driven catalytic efficiency of the prepared composites in terms of HER. The measurements have been carried out by employing current protocols applied in the literature for g-C_3N_4-based composites, *i.e.*, in 10% (v/v) aqueous triethanolamine (TEOA), as a typical sacrificial agent, and with Pt (3wt%) as metal co-catalyst.[13]

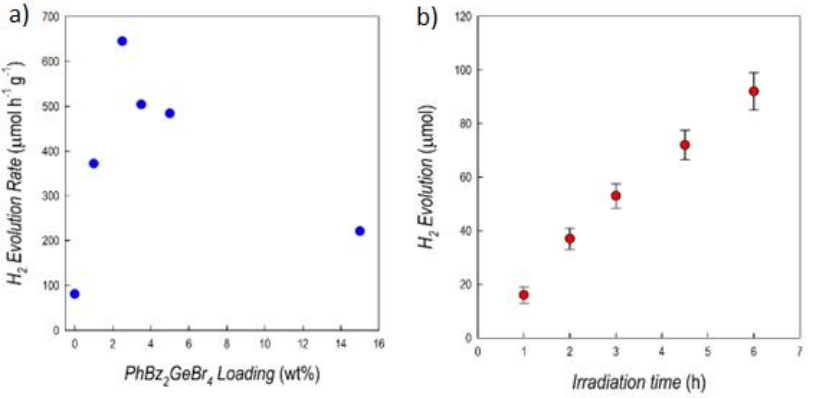

Figure 87 Hydrogen photogeneration performance of $PhBz_2Ge_2Br_4$/g-C_3N_4 composites. *(a) Hydrogen evolution rates for $PhBz_2Ge_2Br_4$/g-C_3N_4 composites at different percentages of MHP loading, 6 h irradiation, RSD < 10% (n=3); (b) Hydrogen evolution profile over irradiation time for the 2.5wt% $PhBz_2Ge_2Br_4$/g-C_3N_4 composite, RSD < 10% (n=3). Conditions: 1 g L^{-1} catalyst, 10% v/v TEOA, 3wt% Pt, simulated solar light (Xenon lamp, 500 W m^{-2}, 300-800 nm, IR-treated soda lime glass UV outdoor filter).*

Figure 87a shows the HER as a function of perovskite loading, while Figure 87b shows the kinetics of the hydrogen evolution for the best performing composite from Figure 87a, namely 2.5 wt%/$PhBz_2GeBr_4$g-C_3N_4.
Noticeably, the composites display a synergic effect providing a significant improvement of HER of about 8 times with respect to pure carbon nitride (81 μmol g^{-1} h^{-1}) and of about 100 times with respect to pure $PhBz_2GeBr_4$ (6 μmol g^{-1} h^{-1}). The maximum HER is found at a relatively low MHP loading of 2.5wt%, while higher perovskite percentages are not beneficial to improve the photoreaction. For the optimal composite, namely at 2.5wt%, the kinetics of H_2 evolution, reported in Figure 87b, indicates a substantial linear increase of the hydrogen production as function of time. The value of apparent quantum yield (AQY%), calculated as the percent ratio H_2 moles/incident photons moles, for this composition (2.5wt% of perovskite) was proven to be 5.2%.[14] This is the first evidence of the application of a Ge-based perovskite in solar-driven hydrogen generation, therefore any comparison with pre-existing literature is not possible. However, the measured rates are similar to those measured for Sn-based and Bi-based perovskites.[2,9,12] The composite at 2.5wt% of $PhBz_2GeBr_4$ has been tested over four successive catalytic cycles by centrifugating, recovering, and subjecting the sample to the same photocatalytic procedure. The HER in the second cycle was about 94% of the initial HER, while in both the third and fourth cycles it was reduced to about 74%; such result could be related to the slight but detectable Ge leaching reported above Finally, the catalyst, was recovered after a photogeneration test and analyzed by XRD to test the material stability. For the sake of clarity this test was accomplished on the material with 15wt% loading of $PhBz_2GeBr_4$ since it showed the most evident reflections from the perovskite. The patterns of fresh $PhBz_2GeBr_4$ 15wt%/g-C_3N_4 and of the same sample recovered after 6 hours of irradiation under the conditions reported above are shown in Figure 88, indicating a very excellent stability of the composite after the photocatalytic test.

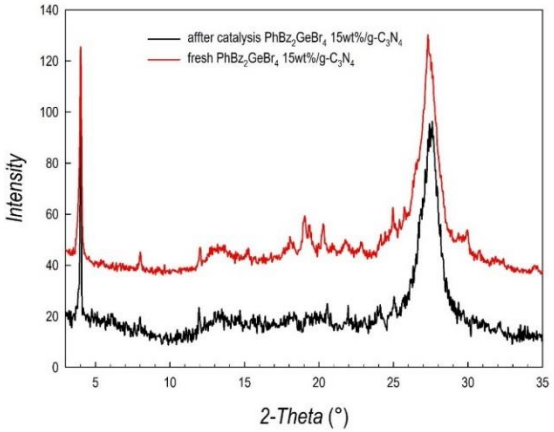

Figure 88 *XRD pattern of 15 wt% $PhBz_2GeBr_4$/g-C_3N_4 before (red) and after (black) photocatalysis.*

The origin of the reported results was further investigated from an atomistic perspective with the aim of understanding: (i) the outstanding water stability of the Ge-based perovskites synthetized in this work and (ii) the efficient photocatalytic production of H_2 when the perovskites are used in a composite with g-C_3N_4. In addition, computational modelling was extended to also include the iodide-analogous phase, namely, $PhBz_2GeI_4$, to determine its possible application in photocatalysis. As a matter of fact, the presence of iodide can red-shift the band gap and provides a more effective charge transfer in the heterostructure.[4,8,15] However, iodide-based materials are known to be less stable than the bromide counterparts.

To fulfil the first goal, we calculated the bulk formation energies E_f(bulk) of the water-stable Ge-based perovskites and we compared them to those of previously synthetized materials, bearing different A-site spacer cations, which were found to dissolve in aqueous environment.[8] Since no experimental crystallographic structure is currently available for $PhBz_2GeI_4$ and $PhBz_2GeBr_4$, we consider the perovskites with biphenyl-ethylene-ammonium (BPEA), which differs from PhBz only for an extra CH_2 between

the aromatic ring and the ammonium moiety.[1] $BPEA_2GeI_4$ and $BPEA_2GeBr_4$ were modelled starting from the analogous $BPEA_2PbI_4$. We consider, for our comparison, PEA_2GeI_4 and $BrPEA_2GeBr_4$, which have been synthetized and characterized in Ref. 1.
From the following reaction:

$$2AX + GeX_2 \text{ -- > } A_2GeX_4 \quad (1)$$

where A = Phenyl-ethylene-ammonium (PEA), 2-Bromo-Phenyl-4-ethylen-ammonium (BrPEA), BPEA (biphenyl-ethylene-ammonium) X=Br, I, we define E_f(bulk) as follows:

$$E_f(\text{bulk}) = E(A_2GeX_4) - E(AX) - E(GeX_2) \quad (2)$$

In Eq. 2, $E(A_2GeX_4)$, $E(AX)$ and $E(GeX_2)$ are the total-energies of A_2GeX_4, AX and GeX_2, which are calculated from their respective atomistic models. Results collected in Table 7 clearly indicate that perovskites bearing BPEA as spacer A-site cation are substantially more stable than the others, with formation energies being up to 0.7 eV lower. Such a larger stability may be ascribed to the enhanced van der Waals interactions available within the A-cation layers separating the inorganic frameworks when using the larger BPEA molecule. In order to assess this consideration, we calculate for each studied material the formation energy of a neutral A vacancy, V_A, which is defined as:

$$E_f(V_A) = E(V_A) - E(A_2GeX_4) - E(A) \quad (3)$$

where $E(V_A)$ is the total energy of the perovskite model with a missing A molecule and E(A) the total energy of an isolated A molecule. From Table 7, we evince that the energy associated with the removal of an A cation from the bulk perovskite is remarkably higher (up to 1 eV) for BPEA when compared to the other systems, thus clearly indicating that intra-layer Van der Waals interactions sizably stabilize BPEA perovskites. Furthermore, the higher solvation Gibbs free energies calculated for BPEA and PhBz indicate a reduced tendency of these cations to dissolve in water, when compared

to the cations employed in previous work.[8] We note that such a result is in line with a previous observation of the increased water stability observed when replacing methylammonium with dimethylammonium in tin perovskites.[16,17]

Table 7 *Calculated values of E_f(bulk) and $E_f(V_A)$ (cf. main text for definitions) for the considered A_2GeX_4 perovskites.*

Perovskite	E_f(bulk)	$E_f(V_A)$	Water-stable?
PEA_2GeBr_4	−4.15	3.98	NO
$BrPEA_2GeBr_4$	−4.12	4.18	NO
$(BPEA)_2GeI_4$	−4.65	4.92	YES
$(BPEA)_2GeBr_4$	−4.80	5.26	YES

To study the beneficial effect on the photocatalytic H_2 production of the $BPEA_2GeX_4$ perovskites in a composite with g-C_3N_4, we investigated their band alignment. To this end, we constructed atomistic models of the surface of these materials. When considering the (100) surface of $BPEA_2GeX_4$, we find that the most stable termination is the stoichiometric (BPEA)X-terminated one, with the BPEA cations pointing their hydrophobic biphenyl moieties towards the surface [cf. Figure 89a for the (BPEA)I terminated surface of $BPEA_2GeI_4$] while the ammonium moieties interact with the sub-surface inorganic chain. This termination features a surface energy as small as 0.005 eV/Å^2.

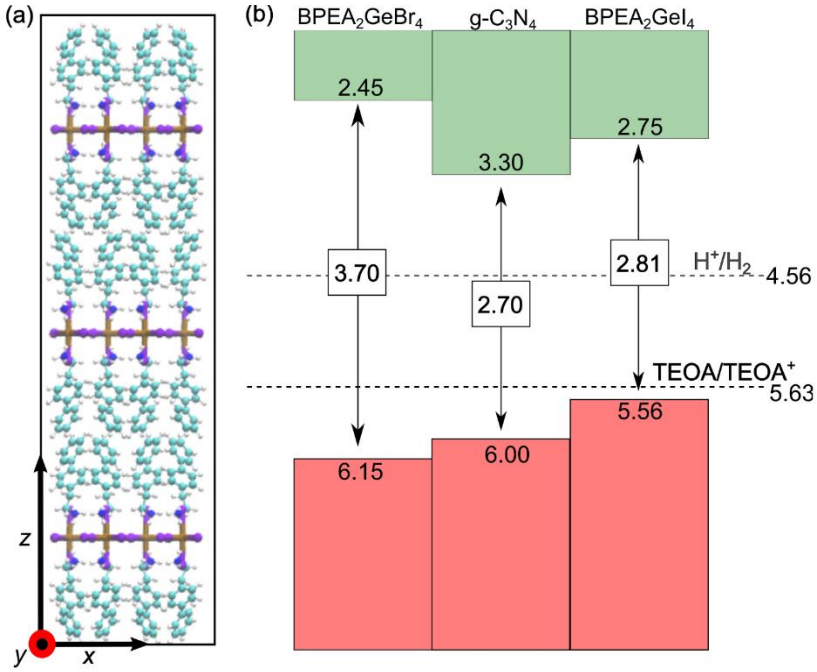

Figure 89 Computational modelling of surface termination and band alignment for $(BPEA)_2GeI_4$ and $(BPEA)_2GeBr_4$. *(a) Stick & ball representation of the atomistic model for the (BPEA)I-terminated (100) slab of $(BPEA)_2GeI_4$ perovskite. Ge atoms are depicted in ochre, I in violet, C in cyan, N in blue, and H in white. (b) Valence band (VB) and conduction band (CB) edges of g-C_3N_4, $(BPEA)_2GeI_4$, and $(BPEA)_2GeBr_4$ referred to the vacuum level. The energy level of standard hydrogen electrode calculated in Ref. 2 and the TEOA/TEOA redox level are reported as dashed lines.*

Then, we employed advanced electronic-structure calculations to evaluate the band gap of the materials and align the band edges with respect to the vacuum level. The band alignment for $BPEA_2GeI_4$ and $BPEA_2GeBr_4$ is reported in Figure 89b along with that previously calculated in Ref. 2 for g-C_3N_4. The band edges of $BPEA_2GeI_4$ are found be favourably aligned with respect to those of g-C_3N_4, thus promoting the transfer of photo-generated charges in a Type 2 heterojunction, which could also improve the carrier lifetime. At variance with this, $BPEA_2GeBr_4$, which features a larger band gap

(3.7 eV vs 2.81 eV), has his valence band edge at an energy 0.15 eV lower than g-C_3N_4, providing a Type I heterojunction. This implies that hole transfer from g-C_3N_4 to the perovskites might be subject to a small energy barrier, which may reduce the efficiency of the composite.

The results of the computational modelling have put in prominence two main results: i) confirmation of the water-stability for $BPEA_2GeBr_4$ together with a beneficial band-alignment with g-C_3N_4, as demonstrated by the above reported hydrogen photogeneration experiments, and ii) prediction of good water-stability by $BPEA_2GeI_4$ [even though with lower E_f(bulk) and $E_f(V_A)$ with respect to $BPEA_2GeBr_4$] and possible superior photocatalytic performance due to a better band-alignment with respect to the bromide-containing counterpart.

To test this last computational evidence, we synthesized the $PhBz_2GeI_4$ perovskite and a series of composites with g-C_3N_4 (1, 2.5, 3, 3.5, 4, 4.5, 5, and 15% of perovskite loading). Figures 90a and 90b reports the XRD and absorbance data on the composite.

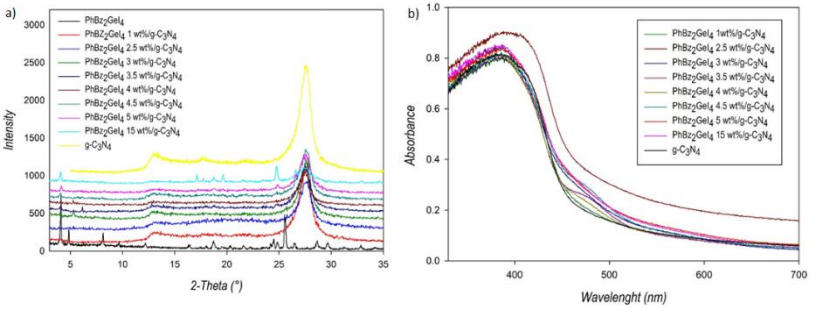

Figure 90 *(a) XRD patterns and (b) UV-Vis spectra of $PhBz_2GeI_4$/g-C_3N_4 composites for different perovskite loadings.*

We used the same approach we employed for $PhBz_2GeBr_4$ in testing the air and water stability of $PhBz_2GeI_4$. Figure 91 shows good air and water stabilities also for the iodide-containing perovskites, according to the computational prediction.

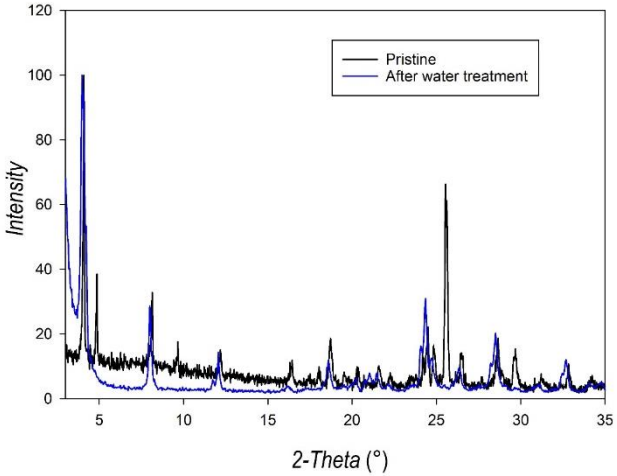

Figure 91 *XRD pattern of $PhBz_2GeI_4$ before (black) and after (blue) water treatment.*

However, the leaching test revealed an amount of Ge in the solution of about 40% already after 4 hours of stirring. This value remains then constant after 8 and 16 hours of stirring (42 and 43%), suggesting the possible occurrence of a solubility equilibrium which then keeps the perovskite unchanged in the solution, according to the XRD diffraction after recovering the powder (Figure 91). Substantially the same leaching (44%) was noticed also under photocatalytic conditions, turning in line with the overall good photocatalytic performance of this composite, described hereafter. Even though the $PhBz_2GeI_4$ results to be less stable in water, which also agrees with the calculated values of E_f(bulk), $E_f(V_A)$, we performed a thorough investigation of the hydrogen photogeneration efficiency. Figure 92a reports the HER as a function of perovskite loading for the $PhBz_2GeI_4$/g-C_3N_4 composites, while Figure 92b shows the kinetics of the hydrogen photogeneration for the best performing composite from Figure 92a, namely 3wt% $PhBz_2GeI_4$/g-C_3N_4 (AQY% of 2.8%).

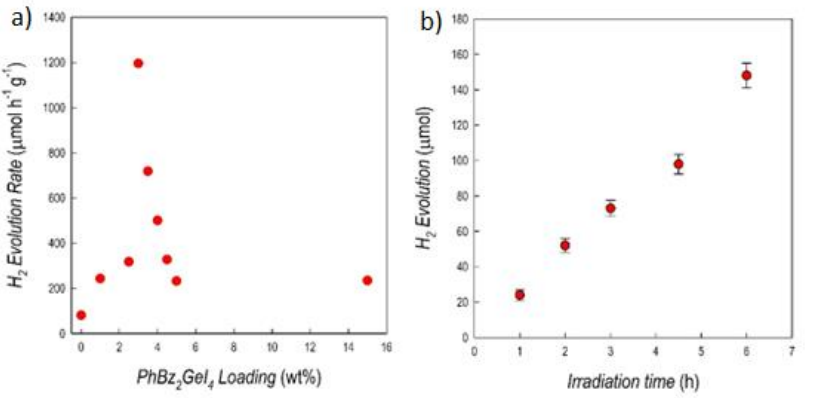

Figure 92 Hydrogen photogeneration performance of $PhBz_2Ge_2I_4$/g-C_3N_4 composites. *(a) Hydrogen evolution rates for $PhBz_2Ge_2I_4$/g-C_3N_4 composites, 6 h irradiation, RSD < 15% (n=3); (b) Hydrogen evolution profile over irradiation time for the 3wt% $PhBz_2Ge_2I_4$/g-C_3N_4 composite, RSD < 10% (n=3). Conditions: 1 g L^{-1} catalyst, 10% v/v TEOA, 3wt% Pt, simulated solar light (Xenon lamp, 500 W m^{-2}, 300-800 nm, IR-treated soda lime glass UV outdoor filter).*

The HER for the $PhBz_2GeI_4$/g-C_3N_4 composites is higher with respect to the $PhBz_2GeBr_4$/g-C_3N_4 composites, reaching a value of about 1200 µmol g^{-1} h^{-1}, again with a synergic effect with respect to pure carbon nitride (81 µmol g^{-1} h^{-1}) and of about 600 times with respect to pure $PhBz_2GeI_4$ (2 µmol g^{-1} h^{-1}). The maximum HER is found at 3wt%, very close to the value of 2.5wt% found for the $PhBz_2GeBr_4$/g-C_3N_4 series. Again, according to the computational modelling, we could confirm the better band alignment of this perovskite with g-C_3N_4 leading to a better performing heterostructure. While this composite showed to be less stable than the bromide counterpart, these results pave the way to further explore this system by improving its stability in water through encapsulations strategies.

Conclusions

We herein report a study on the realization of an intrinsically water stable 2D germanium-based halide perovskite, a novel material that can remarkably sustain suspension in water for several hours. The strategy pursued for generating such innovative system involves the use of an extended π conjugated organic cation (phenylbenzylammonium) which, through intra-layer van der Waals interactions, sizably stabilizes the resulting bulk perovskite. The material has been tested, therefore, for simulated solar light inducing hydrogen evolution from water, in combination to a partnering material; the reaction leads to the formation of an active heterojunction, responsible for very promising hydrogen evolution rates up to 1200 μmol g^{-1} h^{-1}. This may represent an outstanding result, considering the seminal exploitation of a germanium perovskite for such purposes, providing a proof-of-concept for the use of 2D Ge-based MHPs. Even more importantly, these findings may contribute to consolidate the rationale underlaying the intelligent design of intrinsically water stable MHPs phases. The achievement of such understating would have a massive impact on MHPs-based photocatalytic application, but it would also boost alternative optoelectronic innovations based on such class of materials such as LED, PV and detectors whose technological implementation was delayed, mainly due to moisture exposure weakness of the active material**.**

References

1. Venkatesan, N.R., Mahdi, A., Barraza, B., Wu, G., Chabinyc, M.L., and Seshadri, R. (2019). Enhanced yield-mobility products in hybrid halide Ruddlesden–Popper compounds with aromatic ammonium spacers. Dalton Trans. *48*, 14019–14026.
2. Romani, L., Speltini, A., Ambrosio, F., Mosconi, E., Profumo, A., Marelli, M., Margadonna, S., Milella, A., Fracassi, F., Listorti, A., et al. (2021). Water-Stable DMASnBr3 Lead-Free Perovskite for

Effective Solar-Driven Photocatalysis. Angewandte Chemie International Edition *60*, 3611–3618.

3. Pisanu, A., Speltini, A., Quadrelli, P., Drera, G., Sangaletti, L., and Malavasi, L. (2019). Enhanced air-stability of Sn-based hybrid perovskites induced by dimethylammonium (DMA): synthesis, characterization, aging and hydrogen photogeneration of the MA1−xDMAxSnBr3 system. J. Mater. Chem. C *7*, 7020–7026.
4. Malavasi, L., Morana, M., and Chiara, R. (2021). Germanium-based Halide Perovskites: Materials, Properties, and Applications. ChemPlusChem, cplu.202100191.
5. Chen, M., Ju, M.-G., Garces, H.F., Carl, A.D., Ono, L.K., Hawash, Z., Zhang, Y., Shen, T., Qi, Y., Grimm, R.L., et al. (2019). Highly stable and efficient all-inorganic lead-free perovskite solar cells with native-oxide passivation. Nature Communications *10*, 16.
6. Prabhakaran, K., and Ogino, T. (1995). Oxidation of Ge(100) and Ge(111) surfaces: an UPS and XPS study. Surface Science *325*, 263–271.
7. Wagner, C.D., Zatko, D.A., and Raymond, R.H. (1980). Use of the oxygen KLL Auger lines in identification of surface chemical states by electron spectroscopy for chemical analysis. Anal. Chem. *52*, 1445–1451.
8. Malavasi, L., Bindi, L., Coduri, M., De Angelis, F., Fracassi, F., Gaboardi, M., Listorti, A., Mahata, A., Milanese, C., Morana, M., et al. (2021). Role of Spacer Cations and Structural Distortion in Two-Dimensional Germanium Halide Perovskites. J. Mater. Chem. C. 10.1039/D1TC02394B.
9. Romani, L., Bala, A., Kumar, V., Speltini, A., Milella, A., Fracassi, F., Listorti, A., Profumo, A., and Malavasi, L. (2020). PEA2SnBr4: a water-stable lead-free two-dimensional perovskite and demonstration of its use as a co-catalyst in hydrogen photogeneration and organic-dye degradation. J. Mater. Chem. C *8*, 9189–9194.

10. Sharma, A., Varshney, M., Chae, K.H., and Won, S.O. (2018). Mechanistic investigations on emission characteristics from g-C3N4, g-C3N4@Pt and g-C3N4@Ag nanostructures using X-ray absorption spectroscopy. Current Applied Physics *18*, 1458–1464.
11. Yuan, Y., Zhang, L., Xing, J., Utama, M.I.B., Lu, X., Du, K., Li, Y., Hu, X., Wang, S., Genç, A., et al. (2015). High-yield synthesis and optical properties of g-C3N4. Nanoscale *7*, 12343–12350.
12. Romani, L., Speltini, A., Dibenedetto, C.N., Listorti, A., Ambrosio, F., Mosconi, E., Simbula, A., Saba, M., Profumo, A., Quadrelli, P., et al. (2021). Experimental Strategy and Mechanistic View to Boost the Photocatalytic Activity of $Cs_3Bi_2Br_9$ Lead-Free Perovskite Derivative by $g\text{-}C_3N_4$ Composite Engineering. Adv. Funct. Mater. *31*, 2104428.
13. Cao, S., Low, J., Yu, J., and Jaroniec, M. (2015). Polymeric Photocatalysts Based on Graphitic Carbon Nitride. Advanced Materials *27*, 2150–2176.
14. Speltini, A., Romani, L., Dondi, D., Malavasi, L., and Profumo, A. (2020). Carbon Nitride-Perovskite Composites: Evaluation and Optimization of Photocatalytic Hydrogen Evolution in Saccharides Aqueous Solution. Catalysts *10*, 1259. 10.3390/catal10111259.
15. Li, X., Hoffman, J.M., and Kanatzidis, M.G. (2021). The 2D Halide Perovskite Rulebook: How the Spacer Influences Everything from the Structure to Optoelectronic Device Efficiency. Chem. Rev. *121*, 2230–2291.
16. Ricciarelli, D., Kaiser, W., Mosconi, E., Wiktor, J., Ashraf, M.W., Malavasi, L., Ambrosio, F., and De Angelis, F. (2022). Reaction Mechanism of Photocatalytic Hydrogen Production at Water/Tin Halide Perovskite Interfaces. ACS Energy Lett., 1308–1315.
17. Kaiser, W., Ricciarelli, D., Mosconi, E., Alothman, A.A., Ambrosio, F., and De Angelis, F. (2022). Stability of Tin- versus Lead-Halide Perovskites: Ab Initio Molecular Dynamics Simulations of Perovskite/Water Interfaces. J. Phys. Chem. Lett. *13*, 2321–2329.

CHAPTER 7.

HIGH PRESSURE STUDIES

The exploration of the effects of external pressure application on MHPs is a topic of continuous interest because of the relevant and, in some cases, impressive modulation of the optical and electronic properties that can be induced on the MHP soft lattice at relatively low-pressure regimes. [68,110–113] The rich set of experimental and computational data as a function of pressure collected on 3D perovskites allowed to highlight and define several common trends in the pressure-response of, for example, band gap and carrier lifetime, providing a solid basis to anticipate and predict the phase stability and electronic properties changes in these phases. [63,66,67,113,114] In addition to the fundamental research interest of pressure-induced phenomena, the information collected in situ during pressure application may be possibly used at ambient conditions in devices by a proper modulation of stress/strain phenomena. [115,116]

The study of pressure effects on the electronic and optical properties of low-dimensional perovskites (LDPs) and perovskite-derivatives is very limited, notwithstanding the current huge interest related to the vast possibility provided by the variation of the structural dimensions (2D, 1D, and 0D) and octahedral connectivity (corner-sharing, edge-sharing, and face-sharing) in this class of materials. [6,117,118] The available data about the pressure response of LDPs have been recently reviewed by Zhang *et al.* [119] Differently from 3D perovskites, for which the variation of the bond lengths and bond angles of the inorganic framework on pressure application plays the key role in the modulation of properties, the presence of a bulky organic component, layered among the inorganic layers in 2D perovskites, provides a further degree of structural complexity and may suggest novel routes for the tuning of functional properties. The number of 2D MHPs prepared and investigated to date, particularly lead-based materials, sounds impressive.

These studies, including the rational design of the organic cation and halide, have shed light on the structure-property correlation in these systems providing a solid route to design tailored materials. [6]

On the other hand, the number of high-pressure studies of 2D MHPs with n = 1 is very limited and only focused on a few types of organic spacers, even though these specific LDPs are among the structural series of major interest for applications. [119] $(BA)_2PbI_4$ (BA = butylammonium) has been the object of intense High Pressure (HP) studies by various authors since 2004. [120,121] A thorough investigation by Yuan *et al.* up to 40 GPa indicates the presence of three phase transitions at 0.22, 2.2 and 13.1 GPa, with the coexistence of phase II and III in the range 2–7 GPa; however, it should be stressed that the sample shows a clear on-set of amorphization already from about 4 GPa. [121] The band gap of $(BA)_2PbI_4$, determined from absorbance measurements, first presents a blue-shift at about 0.22 GPa from 2.28 to 2.37 eV, followed by a progressive band gap narrowing up to 0.95 eV at around 35 GPa. [121] The trend of photoluminescence (PL) data confirms the behaviour of absorbance measurements with a peak in the PL intensity around 2 GPa, eventually vanishing around 6–7 GPa. Both PL and absorbance data point toward the presence of a wide two-phase region below 10 GPa, as evidenced by HP X-ray diffraction (XRD) data. An analogous 2D perovskite with a longer alkyl chain (octylammonium) has been investigated up to 25 GPa in 2001. [122] The authors reported the trend of PL and absorbance only, without any structural evidence as a function of P. A progressive reduction of the band gap from about 2.4 to 1.9 eV is observed in the P range from ambient pressure to about 12 GPa. [122] From the reported data it is possible to observe the presence of multiple absorption edges and PL peaks (up to three) from about 2 GPa to about 8 GPa, interpreted by the authors as originating from bound-exciton states. Other phenomena such as the disappearance of the excitonic state are discussed in terms of a change in the band structure from direct to indirect. Alternatively, as can be indirectly inferred from the reported plots of the optical properties, the observed trends could be due to the presence of a system composed by more than one structural phase as occurs in the

$(BA)_2PbI_4$. It is interesting to note that in these $(C_nH_{2n+1}NH_3)_2PbI_4$ perovskites, for n = 4 and 8, the trend of the band gap is different with respect to lead-based 3D perovskites where, after a red shift at relatively low pressures, a progressive blue-shift occurs, usually accompanied by structural amorphization. [68]

7.1 Diamond Anvil Cells

High-pressure experiments are carried out by using a diamond anvil cell (DAC), composed by two opposing diamonds which compress a gasket surrounding the sample in a pressure-transmitting medium (Figure 93).

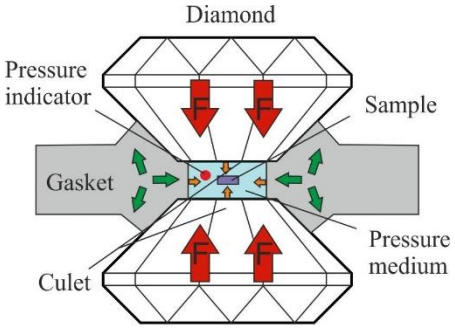

Figure 93 *Schematic representation of a diamond anvil cell.*

Depending on experimental parameters such as diamond size, culet diameter, gasket material and pressure medium, the reached pressure can be up to 100 GPa. Diamond is used for these high-pressure structural studies because it represents the hardest material and it is transparent to the x-ray radiation. The gasket is a thin foil which avoids the direct contact between the two diamonds and it is usually made of stainless steel: for instance, rhenium and iridium are used for experiments at elevated pressures, while beryllium if the x-rays are required to pass through the gasket. The pressure-

transmitting medium is a solid, liquid or gaseous inert material, depending on the type of experiment, which has the aim to convert the stress applied to the diamonds into pressure on the sample. Examples of pressure-transmitting media can be silicon oil, the mixture methanol:ethanol 4:1, Argon and Helium, the latter used for very high pressures up to 70 GPa. [123] Lastly, the pressure in the DAC is determined using a ruby, that is a red variety of corundum (α-Al_2O_3) with a partial substitution of Al^{3+} with Cr^{3+} causing a strong luminescence. [124]

7.2 Pressure response of decylammonium-containing 2D iodide perovskites

Purpose and scope

Manipulation by external pressure of the optical response of 2D MHPs is a fascinating route to tune their properties and promote the emergence of novel features. Triggered by the actual interest on LDPs and by the limited evidence of a relevant pressure-response in these systems, we investigated here DA_2PbI_4 and DA_2GeI_4 (DA = decylammonium) perovskites in the pressure range up to ~12 GPa by X-ray powder diffraction, absorption, and photoluminescence spectroscopy. Although the two systems share a similar structural evolution with pressure, the optical properties are rather different and influenced by the metal central atom. DA_2PbI_4 shows a progressive red shift from 2.28 eV (P = 0 GPa) to 1.64 eV at 11.5 GPa, with a narrow PL emission, whereas DA_2GeI_4, changes from a non-PL system at ambient pressure to a clear broadband emitter centered around 730 nm with an intensity maximum at about 3.7GPa. These results unveil the role of the central atom on the nature of emission under pressure in 2D MHPs containing a long alkyl chain. The present work provides the only available work of the pressure response of a Ge-based 2D MHPs.

Experimental section

Synthesis of DA_2GeI_4 and DA_2GeI_4

DA_2GeI_4 powder was prepared in inert atmosphere under N_2 flux by a solution method. The followed procedure consisted in the dissolution of a proper amount of GeO_2 powder in a large excess of both 57% w/w aqueous HI and 50% w/w aqueous H_3PO_2, the latter introduced to reduce Ge (IV) and stabilize the reduced oxidation state of Ge. The solution was gradually heated in an oil bath to 100°C under continuous stirring and nitrogen atmosphere to prevent Ge oxidation. After the solid dissolution, a stoichiometric amount of the liquid decylamine was added dropwise. Subsequently, the reaction mixture was cooled down to room temperature obtaining the formation of an orange powder. The precipitate was immediately filtered, dried under vacuum overnight at 65°C and lastly stored in the glove box under Ar atmosphere.
For the DA_2PbI_4 powder the synthetic procedure also consisted in a solution method but performed, in this case, under ambient conditions. A proper amount of lead (II) acetate was dissolved in a large excess of 57% w/w aqueous HI under magnetic stirring. The solution was heated to 100°C in an oil bath until the solid dissolution, and a stoichiometric amount of the amine was introduced dropwise. Then, a bright orange powder was obtained after cooling down to room temperature. The product was finally filtered and dried at 65°C under vacuum overnight.

Characterization of DA_2GeI_4 and DA_2PbI_4

High-pressure x-ray-diffraction studies were carried out on two samples at the Xpress beamline of Elettra. For the pressure run, a membrane-driven symmetric DAC was used together with a PACE5000-based automatic membrane drive. Silicone oil was used as the pressure-transmitting medium (PTM). Pressure was monitored in situ by ruby fluorescence method, by including one or more ruby chips (~10 mm) along with the sample in the pressure cell. Diffraction data collection was performed by a

monochromatic circular beam with a wavelength of 0.495 Å and a beam cross-sectional diameter ~ 40 mm.

Uncorrected emission spectra were obtained on two samples with an Edinburgh FLS980 spectrometer equipped with a Peltier-cooled Hamamatsu R928 photomultiplier tube (185 nm - 850 nm). An Edinburgh Xe900 450W Xenon arc lamp was used as exciting light source. Corrected spectra were obtained via a calibration curve supplied with the instrument.

To record the 77K luminescence spectra on one sample (DA_2GeI_4), the sample was put in glass tubes (2 mm diameter) and inserted in a special quartz Dewar, filled up with liquid nitrogen. For solid samples, λ_{em} have been calculated by corrected emission spectra obtained from an apparatus consisting of a barium sulfate coated integrating sphere (4 or 6 inches), a 450W Xe lamp (λ_{exc} = tunable by a monochromator supplied with the instrument) as light sources, and a R928 photomultiplier tube as signal detectors, following the procedure described by DeMello *et al.* Experimental uncertainties are estimated to be $\pm$ 20% for emission quantum yields, $\pm$ 2nm and $\pm$ 5 nm for emission peaks, respectively.

For the high-pressure absorbance and PL measurements two samples, DA_2GeI_4 and DA_2PbI_4, were prepared in DACs utilizing 400 µm culets. A 250 µm thick Re gasket was pre-indented to ~ 45 mm, and a ~ 200 mm hole was laser-drilled for the sample chamber. The perovskite samples were loaded as ~ 10 µm thick pressed pellets within an inert Ar glove box (MBraun, < 0.5 ppm O_2/H_2O). After sealing under ~ 1 atm Ar, the samples were loaded with high-pressure Ar gas at ~ 1 kbar, which served as the pressure transmitting medium and absorbance reference. A ruby chip was used for pressure calibration. Optical absorbance measurements were performed on two samples on using a Bruker Vertex spectrometer with Hyperion microscope utilizing two-sided, knife-edge collimation (~ 50 µm x 50 µm) and reflecting objectives. A high-intensity water-cooled tungsten lamp served as the NIR-VIS light source. PL measurements were performed using a 532 nm laser excitation source with emission collected in the backscatter geometry through a 50 µm confocal filter and focused onto the entrance slit of a Princeton Instruments spectrograph (SP2750) utilizing a 300 gr/mm grating

(500 nm blaze) and liquid-nitrogen-cooled CCD detector. For the DA_2GeI_4 sample, a 405 nm laser excitation source was also tested, but no PL was detected at room temperature.
Low temperature photoluminescence (PL) measurements were performed on two samples keeping the sample powders inside a flowing liquid nitrogen cryostat (Janis SVT-200-05) equipped with a Lakeshore 331 temperature controller. The sample was excited with a continuous wave laser (Spectra-Physics Millennia IV) operating at 533 nm with 30 mW/cm^2 excitation power density. PL signal was collected with achromatic lenses, spectrally dispersed with a grating spectrograph (Acton SpectraPro 2300i) and finally detected using a Hamamatsu digital camera (model C4742-95).

Results and discussion

High pressure XRD and optical characterization of DA_2PbI_4

DA_2PbI_4 has been prepared by wet-chemistry route, as described before, and the ambient temperature and pressure XRD pattern can be refined in the orthorhombic *Pbca* space group as reported previously.[1]
High-pressure XRD data have been collected at the XPress beamline, Elettra synchrotron, from ambient pressure to 9.4 GPa by using silicone oil as pressure transmitting medium (PTM) at the wavelength of 0.495 Å. An overview of the diffraction patterns collected as a function of the applied pressure is reported in Figure 94, also including the pattern after pressure release (''0 GPa decomp'' at the top of Figure 94).

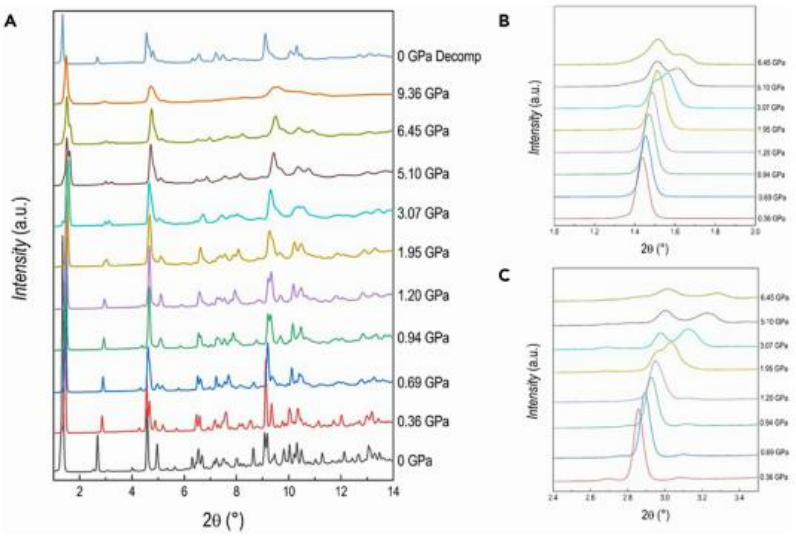

Figure 94 *Diffraction data of DA_2PbI_4: (A) XRD patterns (λ = 0.495 Å) as a function of pressure (reported in GPa on the right) for DA_2PbI_4; (B) and (C) highlights selected intervals of the pattern to better shown the evolution of the (001) and (002) reflections as a function of pressure.*

A sketch of ambient pressure DA_2PbI_4 structure together with bond angles and lengths of the inorganic framework are reported in Figure 95.

Already at the first pressure investigated, namely 0.36 GPa, the crystal structure can no longer be indexed to the ambient conditions orthorhombic Pbca cell, and a monoclinic cell in the space group $P2_1/a$ has been found to properly describe the crystal structure. This symmetry is very close to the one obtained from single crystal data at low temperature (243 K).[1] A similar transition has been reported also for the $(BA)_2PbI_4$ at ≈ 2 GPa, again in analogy with the phase transition sequence as a function of temperature.[2,3] The refinement of the data at 0.36 GPa was then performed in the space group $P2_1/a$, obtained from single crystal data.[1] According to the structural study by Lemmerer and Billing, this $Pbca/P2_1/a$ transformation is mostly due

to changes in the inorganic layers that assume an eclipsed arrangement of adjacent layers, while the unit cell axis halves perpendicular to the layers.[1]

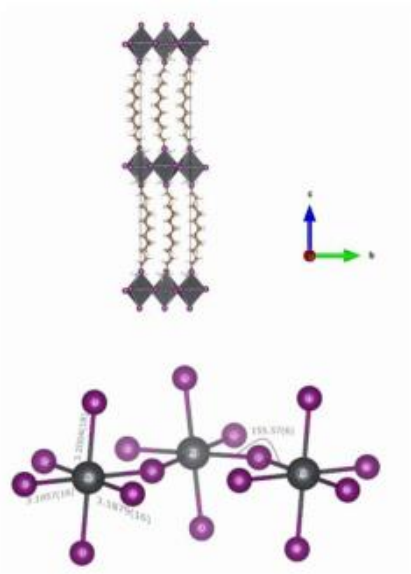

Figure 95 *DA_2PbI_4 structure, with bond angles and lengths.*

The DA_2PbI_4 sample retains the same symmetry up to 1.70 GPa, when the peaks at approximately 1.5 and 3°, corresponding to the single (001) and (002) reflections in the $P2_1/a$ symmetry, start to show a splitting that increases upon compression (Figures 94B and 94C). This phenomenon clearly indicates the presence of two distinct phases in the sample and the patterns were now refined with two phases with space group $P2_1/a$ characterized by the c-axes differing approximately 2 Å each other. Notably, the intensity of the (001) reflection initially decreases till 3.07 GPa, then it increases again on further compression indicating a variation of the relative phase amount with pressure. In this respect, considering the past literature data and the results of the present manuscript, it seems that a common trend of $(C_nH_{2n+1}NH_3)_2PbI_4$ perovskites is the evolution, upon the application

of pressure, to multiple-phase systems.[1,4] At 6.45 GPa the broadening of the peaks increases, and this effect appears more significant at 9.36 GPa, suggesting the onset of partial amorphization. The evolution of the cell parameters and lattice volume is summarized in Figures 96A and 96B.

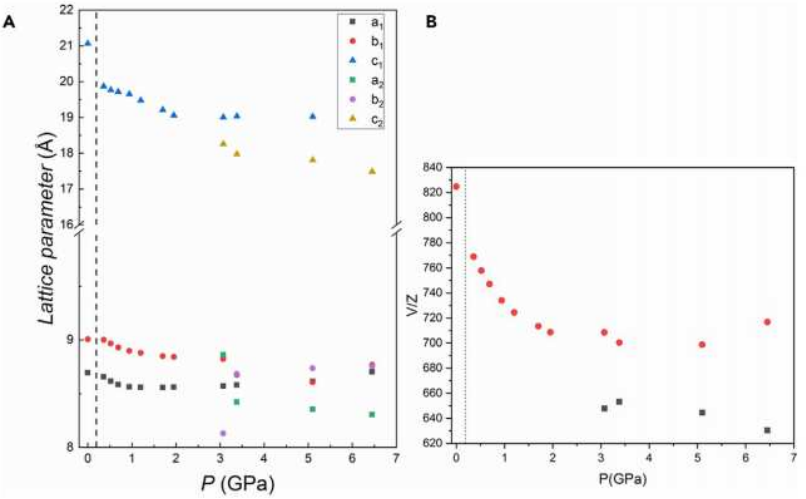

Figure 96 *Pressure dependence of structural parameters of DA_2PbI_4: (A and B) Pressure dependence of the cell parameters a, b, c (A) and of the cell volume (B) for DA_2PbI_4. The c axis of the orthorhombic cell was halved. The dashed line marks the transition from the orthorhombic to the monoclinic cell. Subscripts 1 and 2 refer to the two monoclinic phases. Error bars are smaller than the symbol.*

After pressure release, the pattern can be indexed again with the orthorhombic cell, suggesting at least a certain degree of reversibility of the transition (Figure 97). However, the long-range structural integrity of the sample has been reduced after pressure application, but the position of the most intense peaks in the pattern (00*l*) can be still found at the same positions as the starting sample (Figure 97).

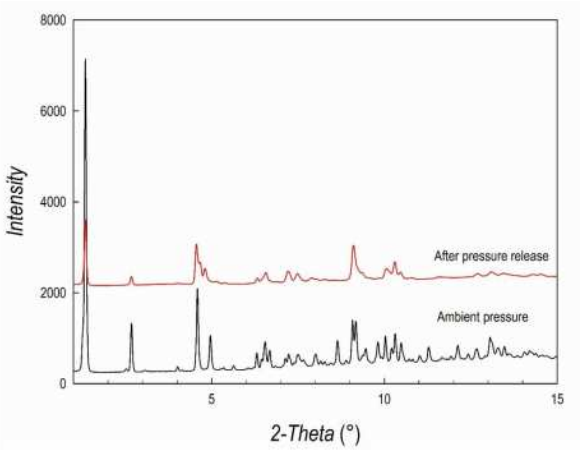

Figure 97 *XRD pattern of DA_2PbI_4 at ambient pressure (black line) and after pressure release (red line).*

The optical properties as a function of pressure have been investigated by absorption and PL spectroscopies and the data are reported in Figures 98A and 100A, respectively. The absorption data show a progressive and continuous red shift by increasing pressure. In general, the spectra reveal sharp edges even in the two-phase region determined by XRD, differently from the PL results (see below). A significant broadening of the spectra, with the appearance of a shoulder, is evident only in the spectra at 7.9 and 9 GPa. The trend of the absorption onset energy determined from the Tauc plot of the spectra of Figure 98A are reported in Figure 98B. The energy progressively decreases from the ambient pressure value of 2.28 eV, in agreement with previous literature data, down to 1.64 eV at 11.5 GPa.[5] No sign of variation is found in the region corresponding to the *Pbca* -- > $P2_1/a$ phase transition (0-0.36 GPa), while a different trend is observed (see continuous lines in Figure 98B) around the region where a two-phase system is found according to diffraction. The trend of absorption during decompression is fully reversible with the spectra at ambient pressure and after pressure release being superimposable (Figure 99).

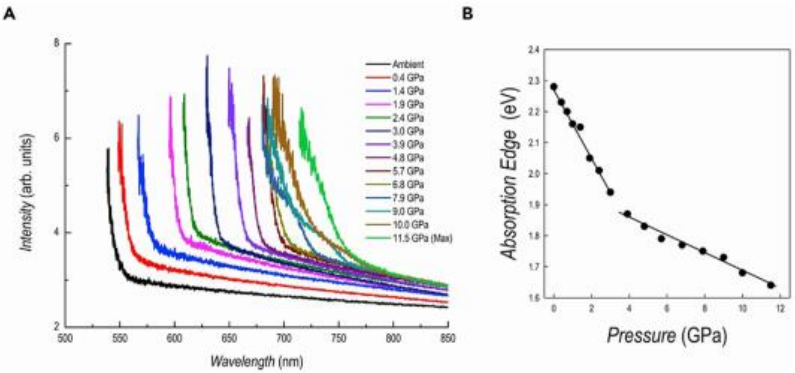

Figure 98 *(A) Absorption spectra as a function of pressure for DA_2PbI_4; (B) trend of the absorption edge extracted from the spectra as a function of pressure.*

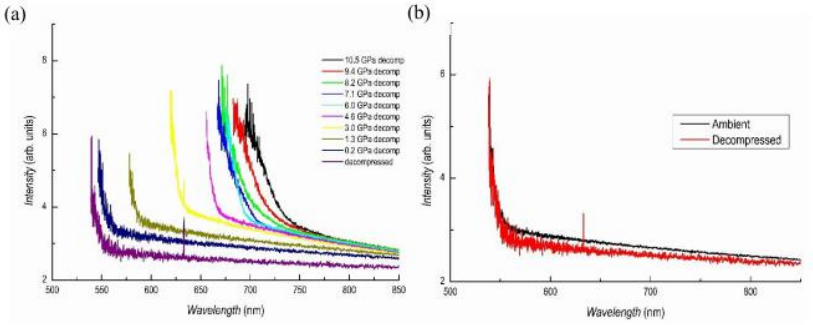

Figure 99 *(a) Absorption spectra as a function of pressure for DA_2PbI_4 during decompression; (b) ambient pressure spectra before applying pressure (black line) and after pressure release (red line).*

The PL spectra as a function of pressure are shown in Figure 100A. A single PL peak is found up to 1.4 GPa (blue curve in Figure 100A) while from 1.9 GPa two distinct peaks are clearly visible in the spectra, with the second one shifted at higher wavelengths. This phenomenon is most probably related to the presence, starting from 1.9 GPa, of two distinct monoclinic phases in

the sample, as shown by XRD analysis, with PL being more sensitive than absorbance in detecting this phase separation effect. The evolution of the peak position, expressed in eV, as a function of pressure is plotted in Figure 100B.

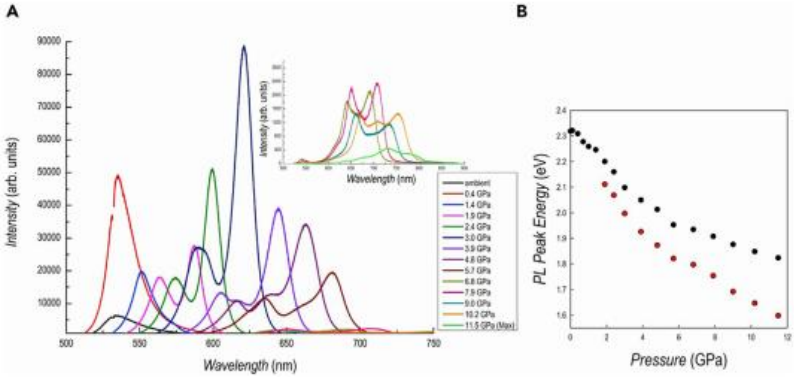

Figure 100 *(A) PL spectra as a function of pressure for DA_2PbI_4; (B) trend of the peak position of the PL data as a function of pressure.*

The intensity of the first peak (lower wavelength) increases passing from ambient pressure to 0.4 GPa (*Pbca* -- > $P2_1/a$ transition) and then gradually reduces its intensity. On the other hand, the low-energy peak intensity progressively increases up to 3 GPa and then decreases up to 5.7 GPa. The PL intensity of both peaks suddenly drops at 6.8 GPa even though the peaks continue to shift at lower energy (see the inset of Figure 100A). The trend of the first PL peak (black dots in Figure 100B) as a function of pressure is very similar to the trend of the band gap extracted from the absorbance data, with a slope deviation around 2 GPa. Possibly, the second peak could be ascribed to the second monoclinic phase with a more compressed c-axes characterized by a low energy band gap (red dots in Figure 100B). Similarly to the absorbance data, the PL after pressure release is superimposable to the one at ambient pressure, confirming the full reversibility of the sample (Figure 101).

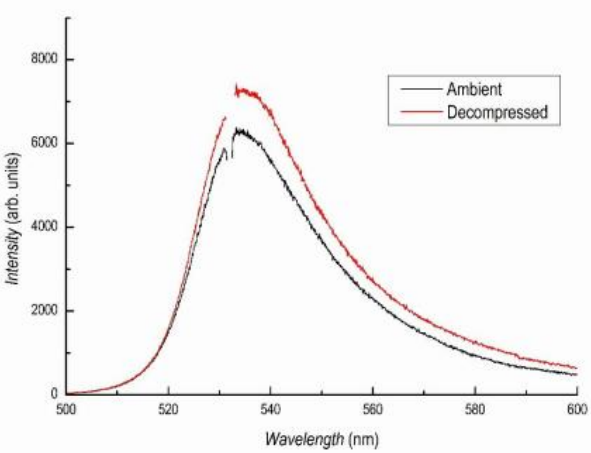

Figure 101 *PL of DA_2PbI_4 at ambient pressure before applying pressure (black line) and after pressure release (red line). Missed part are due to the removal of the laser contribution.*

The trend of the absorbance and PL results may be interpreted considering the progressive Pb-I bond length shortening induced by pressure which gradually narrows the band gap, as commonly found in 3D perovskites.[6] The presence of two distinct PL peaks is related to the presence of two different phases in the sample from about 2 GPa. As can be seen, the two PL peak maxima are well separated and the one at a higher wavelength has a more pronounced red shift with respect to the peak at lower wavelength. As we demonstrated with *in situ* XRD data, the two monoclinic phases have a difference in the c-axis of about 2 Å. It is reasonable to ascribe the low-energy PL peak to the more compressed phase, also considering the trend of the c-axes of both phases shown in Figure 96A, which in some way reconciles with the behaviour of the PL maxima of the two peaks. Some of the results reported here for DA_2PbI_4 have been observed also in BA_2PbI_4 (BA = butylammonium), namely the coexistence of two phases, the trend of the peak positions and intensity. A marked difference between the two samples is related to the absence of any blue-shift at low-pressure. The presence of a blue shift is common in 3D perovskites and is related to the

increase deviation from 180° of Pb-I-Pb bond angle, widening the band gap.[6] For a short alkyl chain, namely four carbon atoms, such an effect is still present whereas in DA_2PbI_4, having a longer chain, only a progressive red shift has been observed. Moreover, it is interesting to note that such red shift is present passing from the orthorhombic to the monoclinic phase and is continuous in such a crystal symmetry. In general, the more distorted octahedra of the monoclinic phase leads to an increase of the band gap, which is not the present case. It is highly probable that the origin of this effect is related to the variation of the organic spacer conformation which progressively becomes more distorted while leading to less tilted and more compressed PbI_6 octahedra and therefore band gap narrowing. This hypothesis has been formulated for the BA_2PbI_4 perovskite where, by increasing pressure, even in a more distorted phase, the octahedra result to be uncorrugated but, due to the low scattering contribution of the organic spacer, it is hard to gain solid insight into the orientation of the organic molecules.[2] A conclusion which may be drawn from the reported data is that a longer organic chain in lead-based 2D perovskites allows to reduce the tilting effects induced by pressure application on the inorganic framework (intralayer compression), making the layer-to-layer compression dominant and as the source of the observed continuous red shift. To corroborate this observation, it is possible to mention that by increasing the number of inorganic layers in the $(BA)_2(MA)_{n-1}Pb_nI_{3n+1}$ system, i.e., making the 2D progressively ''more 3D'', the pressure range of the red shift and the value at which the band gap blue-shift occurs progressively lowers.[7]

<u>High pressure XRD and optical characterization of DA_2GeI_4</u>

An analogous experimental approach has been used to investigate the HP behaviour of DA_2GeI_4, which presents as an orange powder. DA_2GeI_4 is a novel material, and its crystal structure has never been determined before. A sketch of the crystal structure together with bond angles and lengths of DA_2GeI_4 is reported in Figure 102.

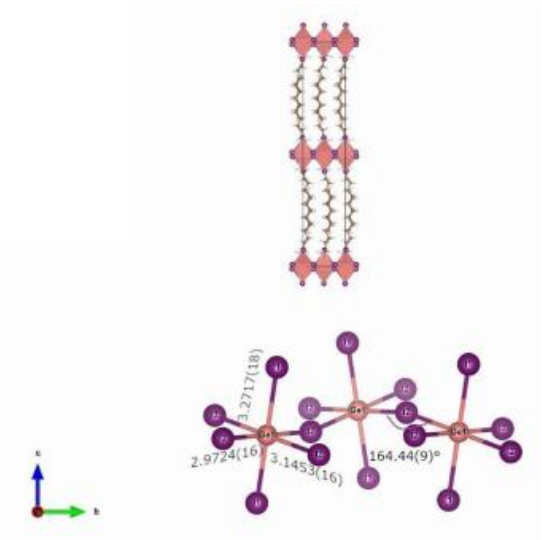

Figure 102 *Sketch of the crystal structure and bond angles and lengths of DA_2GeI_4.*

In addition, as mentioned above, this is the first study of the pressure response of any Ge-based 2D perovskite. Indexing and refinement of powder diffraction data at ambient pressure suggest that the compound crystallize in the orthorhombic system (*Pbca*), as the lead analogue DA_2PbI_4.[1] HP XRD data have been collected up to 11.1 GPa every ~0.5 GPa and some selected patterns are reported in Figure 103A. The first high-pressure pattern at 0.56 GPa shows a monoclinic symmetry in analogy with DA_2PbI_4. The sample persists as a single phase up to 2.20 GPa, when a splitting of the peaks at approximately 1.4° and 2.8° is clearly detectable (Figures 103A and 103B). Beyond this pressure, the patterns were refined with two phases with space group $P2_1/a$, where the c-axes differ by approximately 1 Å. In particular, the intensity of the (001) reflection of the first phase decreases while the (001) reflection of the second phase increases (Figure 103B) as a function of pressure. Already around 3.8 GPa, the phase with longer c-axes represents a significantly minority phase. A similar behaviour occurs for the

(002) reflections around 2.8° (Figure 103C). The two phases clearly coexist up to 5.06 GPa when the broadening of the peaks increases.

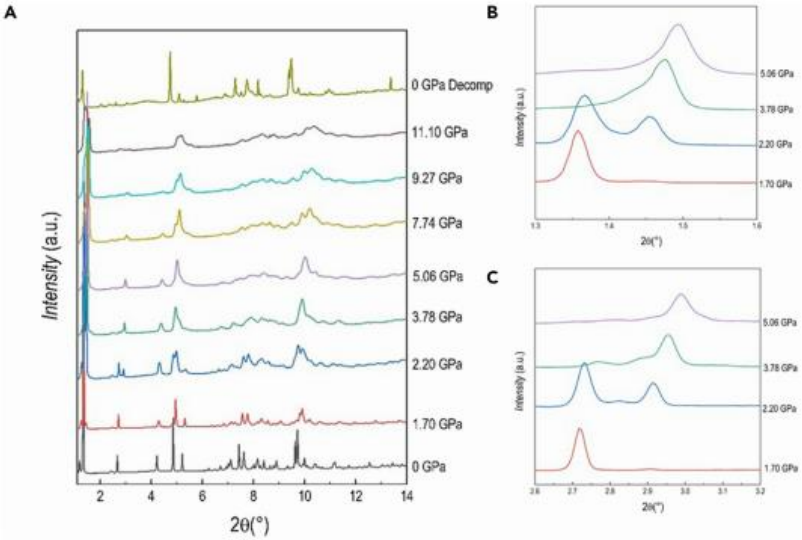

Figure 103 *Diffraction data of DA_2GeI_4: (A) XRD patterns (λ = 0.495 Å) as a function of pressure (reported in GPa on the right) for DA_2GeI_4; (B) and (C) highlights selected intervals of the pattern to better show the evolution of the (001) and (002) reflections as a function of pressure.*

The trend of lattice parameters and lattice volume as a function of pressure are reported in Figures 104A and 104B, respectively.

As mentioned above, DA_2GeI_4 is a novel compound and to get some insight into the structural behaviour observed under pressure we collected variable-temperature laboratory XRD patterns. The most interesting result has been observed by heating the sample from room temperature (RT). Data are reported in Figure 105.

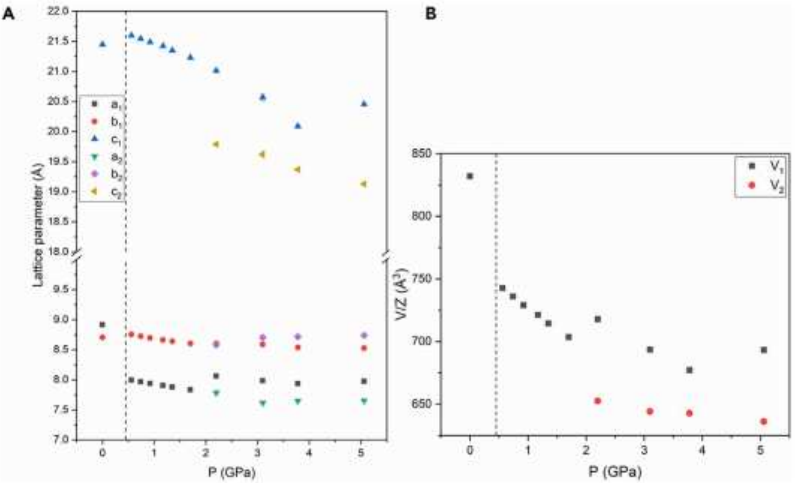

Figure 104 *(A and B) Pressure dependence of the cell parameters a, b, c (A) and of the cell volume (B) for DA_2GeI_4. The c-axis of the orthorhombic cell was halved. The dashed line marks the transition from the orthorhombic to the monoclinic cell. Error bars are smaller than the symbol.*

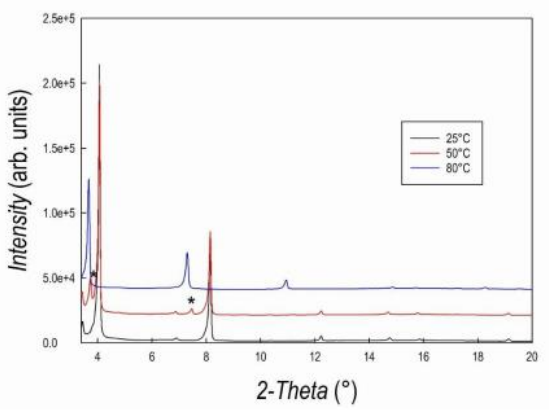

Figure 105 *XRD pattern of DA_2GeI_4 as a function of temperature. Asterisks mark the second peak in the two phases system.*

At 50°C we could observe a phase separation of the sample, analogous to what has been observed by applying pressure. In general, such an effect corresponds to a disordering or even melting of the organic spacer.[1,3,8] Further heating to 80°C leads to the restoration of a single phase (at least with the detection limits of our measurements). The common coexistence of two structural phases by the disordering/melting of the organic spacer by applying pressure and by increasing temperature is an interesting result which merits a further detailed investigation. As a matter of fact, it is known that in $(C_nH_{2n+1}NH_3)_2PbI_4$ perovskites there is a complex and rich phase transition behaviour due not only to the inorganic framework but also to the ordering of the organic spacer.[1,3,8]

The optical properties as a function of pressure have been studied by absorption (Figure 106A) and PL (Figure 107A) spectroscopy.

The spectra as a function of pressure for DA_2GeI_4 show a sudden blue shift after the application of a moderate pressure (0.2 GPa) which may correspond to the set-up of the orthorhombic to monoclinic transition, differently from DA_2PbI_4. Further pressure application gradually red shift the absorbance and, at 2.1 GPa, the spectra is nearly superimposable onto that collected at ambient pressure (cf. Figure 106A). The red shift is then continuous until the maximum pressure investigated (11.4 GPa). With respect to DA_2PbI_4, the absorption edges are less defined and this is a feature quite common in lead-free perovskites with a possible origin in their reduced defect-tolerance.[9] The values of the absorption onset extracted from the Tauc plots (except for some points at low pressure where, given the broad nature of the transitions, we used the maximum absorbance approach) show a change of slope and a sudden decrease in correspondence of about 2 GPa, *i.e.*, the pressure where the patterns were refined with two phases with space group $P2_1/a$ and the c-axes that differ by approximately 1 Å (see above the XRD section). As we pointed out earlier, the phase with shorter c-axis is dominant around 3 GPa, and this reconciles with the absence of multiple absorption edge in the spectra of Figure 106A.

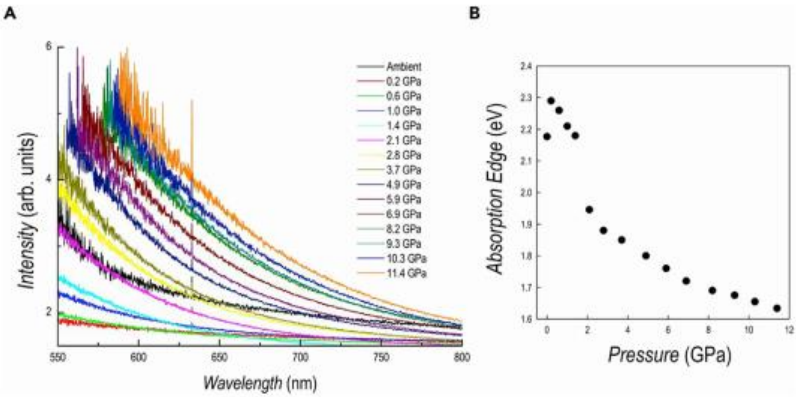

Figure 106 *(A) absorption spectra as a function of pressure for DA_2GeI_4. The peak at 633 nm is from the HeNe calibration laser; (B) trend of the absorption edge extracted from the spectra as a function of pressure.*

The trend of PL data for DA_2GeI_4 is reported in Figure 107A. At ambient pressure the sample has no detectable PL at room temperature while, from 2.1 GPa, a very broad peak, centered around 740 nm (1.67 eV) and with a Stokes shift > 70 nm, emerges and reaches it maximum intensity around 3.7 GPa. The Full width at half maximum (FWHM) of the peak is ~170 nm and both peak position and FWHM have a very modest dependence on pressure. Such behaviour is fully reversible during decompression (Figure 108) and, for comparison, the peak position at 3.7 GPa is 737 nm (compression), and 732 nm at 4.4 GPa (decompression), and the FWHM are 156 and 152 nm, respectively.

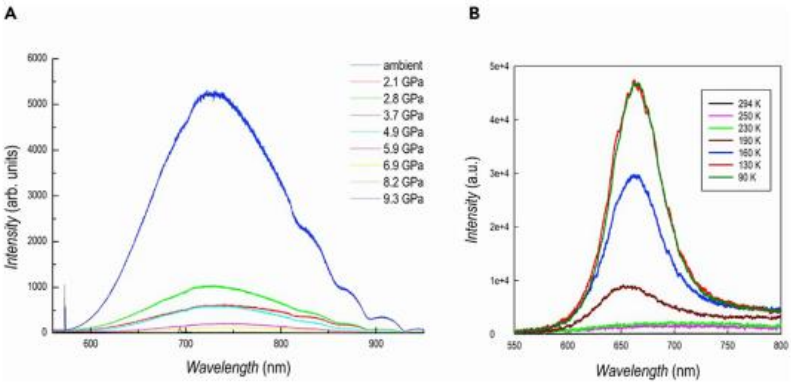

Figure 107 *(A) PL data under compression for DA_2GeI_4. Oscillations above ~800nm are caused by detector etaloning; (B) PL data as a function of temperature for DA_2GeI_4.*

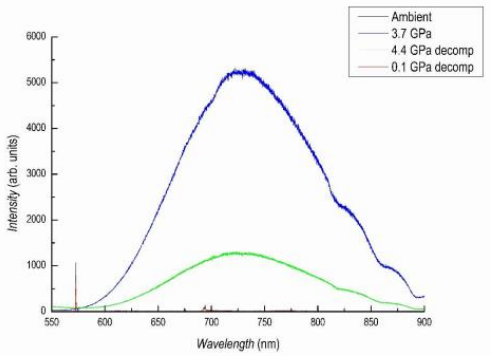

Figure 108 *PL of DA_2GeI_4 at ambient pressure before applying pressure (black line) and after pressure release (red line) and at 3.7 GPa during compression (blue line) and at 4.4 GPa during decompression (red line). Signal around 57' nm comes from the diamond while small peaks around 680 comes from the ruby signal.*

The evidence of a broadband emission by DA_2GeI_4 under pressure is a remarkable and interesting result. It is known that broadband emission in 2D perovskites is closely related to structural distortion induced by the organic spacers and by a wise chemical selection it is possible to modulate

such an effect.[10,11] In addition, we recently demonstrated that Ge-based 2D perovskite have an intrinsic higher degree of octahedra distortion in the bond-length distribution affecting the optical properties.[12] The emergence of broadband distortion around 2.1 GPa may be also correlated to the emergence of the novel monoclinic phase with reduced c-axes (majority phase) which nicely couples to the trend of the band gap shown in Figure 106B. This first evidence of broadband emission by a 2D Ge-containing perovskite under moderate pressure is important to design suitable lead-free materials with analogous properties by playing with the chemical nature of the organic spacer at ambient pressure. The only previous indication, at ambient pressure, of broad emission in a 2D perovskite with Ge was due to Mitzi, and minimal data on pressure-induced broadband emission in 2D perovskite (all lead-based and containing bromide) have been reported to date, namely on PEA_2PbBr_4, BA_2PbBr_4, and $(4BrPhMA)_2PbBr_4$.[13-16] In these cases, the origin of broad emission was found in self-trapped excitons (STEs) generated by lattice structural distortions, but it can also originate from permanent materials defects.[17] The pressure-induced emergence of wide emission in DA_2GeI_4, after the transition from the orthorhombic to the monoclinic phase, may suggest that an increase of structural distortion plays a role but, with the available datasets, we are not in the position of unequivocally assign the observed broad emission to self-trapping phenomena. A detailed discussion about the relaxation mechanisms in 2D perovskites can be found in Smith and Karunadasa (2018).[17] The different behaviour in the two perovskites investigated here, namely DA_2PbI_4 (narrow emission) and DA_2GeI_4 (broad emission) having a different central atom, but showing similar structural features at ambient and under applied pressure, is most likely correlated to the more significant distortion induced by germanium on octahedral bond elongation and bond angle variance, and less on the Ge-Br-Ge bond angle, with respect to Pb-containing perovskite.[12] This also couples to the dependence of the broadband emission on the increase of out-of-plane distortion in similar lead-based 2D perovskites.[12] It is also known that native (or structural related) defects may contribute to self-trapping phenomena related to

broad PL, and it is possible that this phenomenon may contribute to the observed high-pressure optical properties evolution of DA_2GeI_4 because, in general, lead-free materials are less defect tolerant.[10] The possible origin of broad emission in DA_2GeI_4 was further investigated by low-temperature PL measurements (Figure 107B). While still being a non-PL emitter at room temperature, a broad PL signal centered around 665 nm (with a quantum yield around 17 % at 77 K, see Figure 109) starts to be clear around 190 K and its intensity progressively increases by reducing temperature up to 130 K. The broad emission at low temperature has a smaller Stokes shift with respect to the one induced by pressure, being peaked around 665 nm, possibly because of the different extent of the lattice distortions induced by temperature and pressure.

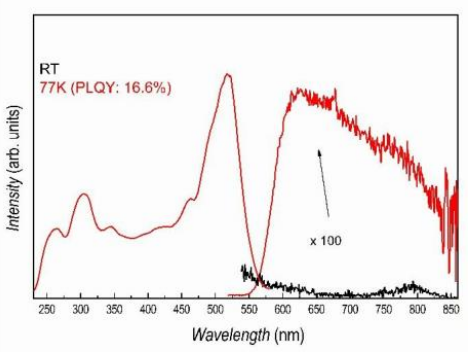

Figure 109 *PL data at room temperature (black line) and 77 K (red line) for DA_2GeI_4.*

As a matter of fact, during pressure application, DA_2GeI_4 converts to a monoclinic phase whereas no evidence of phase transition has been detected by lowering temperature (see differential scanning calorimetry measurement of Figure 110). These data could suggest the presence of STEs induced by lattice deformations as a key characteristic of DA_2GeI_4, with broad emission that can switched on by low-temperature and high-pressure. Further experimental and computational work will be carried out to get a solid microscopic description of the STEs nature in DA_2GeI_4 but it is

clear that the present results open a new avenue to search broad – and possibly white – emitters in lead-free layered perovskites.

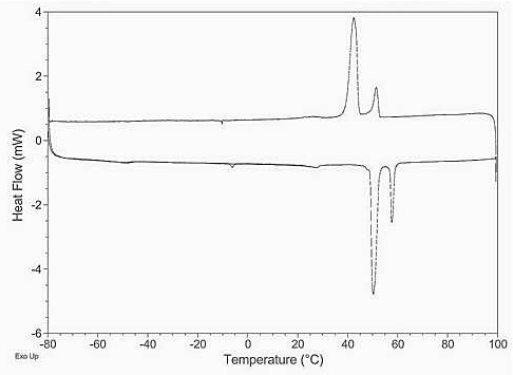

Figure 110 *DSC traces of DA_2GeI_4 (exo up).*

Conclusions

We investigated the structural stability and optical properties of DA_2PbI_4 and DA_2GeI_4 with the aim to provide the evidence of pressure-induced phenomena in 2D perovskites characterized by a long alkyl chain and highlight the role of a different central atom. In this dissertation, we also reported a novel lead-free 2D perovskite, namely DA_2GeI_4, performing the first high-pressure study of a layered Ge-containing phase. From a structural point of view, both perovskites present, at ambient pressure, an orthorhombic crystal structure which converts to a monoclinic symmetry at relatively low-pressure values (<2 GPa). After the phase transition, a further increase of pressure for both materials leads to the separation in two monoclinic phases, during which one of the two compounds displays a distinct shorter c-axis. The present data, together with sporadic literature evidences on pressure response of 2D perovskites, seem to indicate that phase separation might be a quite common behaviour in these systems,

differently from 3D perovskites; this phenomenon could possibly be due to the soft organic spacer that may cause disorders or undergo even melting by increasing pressure. The most remarkable difference between the two samples was found in the evolution of the optical properties as a function of applied pressure. DA_2PbI_4 shows a progressive red shift of the absorption from 2.28 eV at ambient conditions, to 1.64 eV at 11.5 GPa (maximum pressure studied). PL emission is narrow and clearly composed by two components, appearing the second one in concomitance with the phase separation, significantly shifted to lower energy. Maximum PL intensity was found around 3 GPa. Both structural and optical responses as a function of pressure look different with respect to BA_2PbI_4 (the other only alkyl-chain containing 2D perovskite studied to date), this suggesting that a systematic study of the role of chain length on these lead-based 2D perovskites is a valuable tool to elucidate the structure-property correlation as a function of pressure and number of carbon atoms of the spacer. DA_2GeI_4 optical properties under pressure revealed a transition from a non-PL system at ambient pressure to a clear broadband emitter, with a large stoke shift and an intensity maximum at about 3.7 GPa. Absorption measurements shows a first sudden blue-shift (at the orthorhombic to monoclinic phase transition) followed by a continuous red shift. Wide emission with FWHM around 170 nm at about 730 nm in a 2D perovskite containing germanium has not been reported in the current literature up to date. Although we have already assessed an increased octahedral distortion induced by Ge on other systems, such evidence of wide emission by a moderate pressure in a lead-free 2D perovskite is an intriguing result which deserves deep further investigation. By the appropriate choice of an organic spacer, capable of mimicking through chemical pressure a similar distortion degree, it would be possible to design efficient wide or even white lead-free emitters. To conclude, our study provided original insight into the role of alkyl chain length on the pressure-induced effects in lead-based 2D perovskites and unveiled a peculiar behaviour on Ge-based systems, particularly in the emergence of broadband emission. It needs to be emphasized that the scope of the present study should be extended to lead-based systems in

order to clarify the role of chain length on the structural and optical properties change with pressure; even more importantly, analogous Ge-containing 2D perovskites should be taken into account to understand the extent and origin of broadband emission, in order to be able to design suitable materials at ambient condition through chemical pressure effect.

Limitation of the study

In our research a pressure value at which the samples would become fully amorphous could not be reached: it would probably exceed 20 GPa. Moreover, the structures above the phase transitions have been refined by the Le Bail method, thus not allowing to provide a deeper knowledge on the structural parameters of the monoclinic phases. Further measurements with different excitonic wavelengths could allow the collection of the Raman spectra of the samples, because the PL was recorded in the actual experimental set-up. Finally, the absence of clear contributions by the two phases to the absorbance data of DA_2PbI_4 could originate from a low amount of the secondary phase and/or by the decreased sensitivity in the high-absorbance region beyond the transition. A definite answer on the relative importance of these two effects would actually require further challenging studies.

References

1) Lemmerer, A., and Billing, D.G. (2012). Synthesis, characterization and phase transitions of the inorganic-organic layered perovskite-type hybrids [$(C_nH2_{n+1}NH_3)_2PbI_4$], n = 7, 8, 9 and 10. *Dalton Trans.* 41, 1146–1157.
2) Yuan, Y., Liu, X., Ma, X., Wang, X., Li, X., Xiao, J., Li, X., Zhang, H., and Wang, L. (2019). Large band gap narrowing and prolonged carrier lifetime of $(C_4H_9NH_3)_2PbI_4$ under high pressure. *Adv. Sci.* 6, 1900240.

3) Billing, D.G., and Lemmerer, A. (2007). Synthesis, characterization and phase transitions in the inorganic-organic layered perovskite-type hybrids $[(C_nH_{2n+1}NH_3)_2PbI_4]$, n = 4, 5 and 6. *Acta Crystallogr. B Struct. Sci.* 63, 735–747.
4) Matsuishi, K., Suzuki, T., Onari, S., Gregoryanz, E., Hemley, R.J., and Mao, H.K. (2001). Excitonic states of alkylammonium lead-iodide layered perovskite semiconductors under hydrostatic pressure to 25 GPa. *Phys. Stat. Sol*. 223, 177–182.
5) Sichert, J.A., Hemmerling, A., Cardenas-Daw, C., Urban, A.S., and Feldmann, J. (2019). Tuning the optical bandgap in layered hybrid perovskites through variation of alkyl chain length. *APL Mater.* 7, 041116.
6) Postorino, P., and Malavasi, L. (2017). Pressure-induced effects in organic–inorganic hybrid perovskites. *J. Phys. Chem. Lett*. 8, 2613-2622.
7) Liu, G., Gong, J., Kong, L., Schaller, R.D., Hu, Q., Liu, Z., Yan, S., Yang, W., Stoumpos, C.C., Kanatzidis, M.G., et al. (2018). Isothermal pressure-derived metastable states in 2D hybrid perovskites showing enduring band gap narrowing. *Proc. Natl. Acad. Sci*. U S A 115, 8076-8081.
8) Billing, D.G., and Lemmerer, A. (2008). Synthesis, characterization and phase transitions of the inorganic-organic layered perovskite-type hybrids $[(C_nH_{2n+1}NH_3)_2PbI_4]$ (n = 12, 14, 16 and 18). *New J. Chem.* 32, 1736.
9) Xu, J., Maxwell, A., Wei, M., Wang, Z., Chen, B., Zhu, T., and Sargent, E.H. (2021). Defect tolerance of mixed B-site organic–inorganic halide perovskites. *ACS Energ. Lett*, 4220-4227.
10) Cortecchia, D., Neutzner, S., Srimath Kandada, A.R., Mosconi, E., Meggiolaro, D., De Angelis, F., Soci, C., and Petrozza, A. (2017). Broadband emission in two-dimensional hybrid perovskites: the role of structural deformation. *J. Am. Chem. Soc.* 139, 39–42.

11) Smith, M.D., Jaffe, A., Dohner, E.R., Lindenberg, A.M., and Karunadasa, H.I. (2017). Structural origins of broadband emission from layered Pb-Br hybrid perovskites. *Chem. Sci*. 8, 4497–4504.
12) Chiara, R., Morana, M., Boiocchi, M., Coduri, M., Striccoli, M., Fracassi, F., Listorti, A., Mahata, A., Quadrelli, P., Gaboardi, M., et al. (2021a). Role of spacer cations and structural distortion in two-dimensional germanium halide perovskites. *J. Mater. Chem. C*. 9, 9899–9906.
13) Gómez, V., Klyatskaya, S., Fuhr, O., Kalytchuk, S., Zbonl, R., Kappes, M., Lebedkin, S., and Ruben, M. (2020). Pressure-modulated broadband emission in 2D layered hybrid perovskite-like bromoplumbate. *Inorg. Chem.* 59, 12431–12436.
14) Mitzi, D.B. (1996). Synthesis, crystal structure, and optical and thermal properties of $(C_4H_9NH_3)_2MI_4$ (M = Ge, Sn, Pb). *Chem. Mater.* 8, 791–800.
15) Shen, P., Vogt, T., and Lee, Y. (2020). Pressure-induced enhancement of broad-band white light emission in butylammonium lead bromide. *J. Phys. Chem. Lett*. 11, 4131–4137.
16) Zhang, L., Wu, L., Wang, K., and Zou, B. (2019b). Pressure-induced broadband emission of 2D organic-inorganic hybrid perovskite $(C_6H_5C_2H_4NH_3)_2PbBr_4$. *Adv. Sci.* 6, 1801628.
17) Smith, M.D., and Karunadasa, H.I. (2018). White-light emission from layered halide perovskites. *Acc. Chem. Res.* 51, 619–627.

CHAPTER 8.

CONCLUSIONS AND FUTURE PERSPECTIVES

In the last few years, the level of understanding of properties and potential applications of 2D metal halide perovskites has been considerably increased by several research studies of novel phases incorporating different kinds of organic spacers, metallic cations and halides. Up to now, only a minute amount of the possible combinations has already been explored, while a complete understanding of structure-property correlation in 2D perovskites requires an expansion of the currently known structures.

In this PhD work, we have designed and characterized new hybrid layered metal halide perovskites with different compositions, crystal structures and physical properties, with the aim of further enlarging the range of materials with tunable optoelectronic and stability features, as well as to expand the knowledge on lead-free 2D perovskites. Moreover, the lack of systematic and complete investigations of structural and optical properties of already existent systems in the current literature triggered the interest in address these issues by providing comparative studies with our new materials, and between actual results, with previous data on analogue samples. Furthermore, one of the most important goals of this work is represented by the enlargement of the family of broadband emitters and the addition of further insights to develop efficient perovskite-based white light emitters.

The change of organic cation in 2D compounds allows to obtain a huge diversity of structures with tunable electronic and physical characteristics, and the spacer plays an important role in increasing the stability and hydrophobicity. Indeed, our results confirm the possibility of inducing distortions in the inorganic lattice by modifying the nature of organic cation and, therefore, modulating the optical properties. The fundamental key to successfully prepare novel 2D structures is selecting new spacer cations with the right features in terms of charge, shape, size and presence of

heteroatoms. This is because the choice of organic cation has a great influence on the topology of the structure, determining whether the layered motif can occur or not, as we demonstrated in our works. However, in order to raise the number of organic spacers that can be intercalated between the inorganic layers in 2D structures and to extend the knowledge of new hybrid phases, single-crystal, bulk-powder and thin-film synthetic chemistry routes need to be improved and optimized. Indeed, advancing the synthesis and the characterization techniques will particularly of help in preparing multilayer perovskites ($n > 1$), which are more difficult to synthetize and characterize because they are thermodynamically less favourable. Furthermore, several interesting phenomena occurring in layered perovskites, such as self-trapped excitons, exciton-exciton annihilation, charge and energy transfer between different layers, make them suitable for the vast majority of optoelectronic applications; however, more spectroscopic studies are required to explore and understand the mechanisms at the basis of such different behaviour of 2D materials with respect to the 3D compounds, in order to provide a rigorous and ultimate correlation with structural features. All these experimental studies should be correlated as well by sophisticated computational modelling.

Lastly, current literature reports only few examples of lead-free 2D halide perovskites; in view of this finding, we presented the first detailed investigation on 2D germanium-containing phases, also providing a complete overview and an original insight into the role of organic spacer on the pressure-induced effect, never reported up to date. Since the toxicity of lead is a critical topic impacting on the concrete implementation of these materials, global perovskite research should focus more on finding suitable sustainable alternatives, expanding the panorama of possible metals.

Numerous operating difficulties still limit the practical applications of these materials, such as oxidation, degradation, general instability towards moisture, air and water; moreover, the set of available structural data of 2D perovskite compounds is even partial; nevertheless, the project launched during my PhD may represent a starting point to face these crucial issues, providing 2D perovskites with superior stability and structural diversity,

suggesting designing rules for material properties tuning, and defining possible future directions to pursue.

BIBLIOGRAPHY

1. Correa-Baena, J.-P.; Saliba, M.; Buonassisi, T.; Grätzel, M.; Abate, A.; Tress, W.; Hagfeldt, A. Promises and Challenges of Perovskite Solar Cells. *Science* **2017**, 358, 739–744, doi:10.1126/science.aam6323.
2. Lin, K.; Xing, J.; Quan, L.N.; de Arquer, F.P.G.; Gong, X.; Lu, J.; Xie, L.; Zhao, W.; Zhang, D.; Yan, C.; et al. Perovskite Light-Emitting Diodes with External Quantum Efficiency Exceeding 20 per Cent. *Nature* **2018**, 562, 245–248, doi:10.1038/s41586-018-0575-3.
3. Chiara, R.; Morana, M.; Boiocchi, M.; Coduri, M.; Striccoli, M.; Fracassi, F.; Listorti, A.; Mahata, A.; Quadrelli, P.; Gaboardi, M.; et al. Role of Spacer Cations and Structural Distortion in Two-Dimensional Germanium Halide Perovskites. *J. Mater. Chem. C* **2021**, 9, 9899–9906, doi:10.1039/D1TC02394B.
4. Slavney, A.H.; Smaha, R.W.; Smith, I.C.; Jaffe, A.; Umeyama, D.; Karunadasa, H.I. Chemical Approaches to Addressing the Instability and Toxicity of Lead–Halide Perovskite Absorbers. *Inorg. Chem.* **2017**, 56, 46–55, doi:10.1021/acs.inorgchem.6b01336.
5. Zhu, P.; Zhu, J. Low-Dimensional Metal Halide Perovskites and Related Optoelectronic Applications. *InfoMat.* **2020**, 341–378, doi:10.1002/inf2.12086.
6. Li, X.; Hoffman, J.M.; Kanatzidis, M.G. The 2D Halide Perovskite Rulebook: How the Spacer Influences Everything from the Structure to Optoelectronic Device Efficiency. *Chem. Rev.* **2021**, 121, 2230–2291, doi:10.1021/acs.chemrev.0c01006.
7. Maheshwari, S.; Savenije, T.J.; Renaud, N.; Grozema, F.C. Computational Design of Two-Dimensional Perovskites with Functional Organic Cations. *J. Phys. Chem. C* **2018**, 122, 17118–17122, doi:10.1021/acs.jpcc.8b05715.
8. Akkerman, Q.A.; Manna, L. What Defines a Halide Perovskite? *ACS Energy Lett.* **2020**, *5*, 604–610, doi:10.1021/acsenergylett.0c00039.

9. Manser, J.S.; Christians, J.A.; Kamat, P.V. Intriguing Optoelectronic Properties of Metal Halide Perovskites. *Chem. Rev.* **2016**, 116, 12956–13008, doi:10.1021/acs.chemrev.6b00136.
10. Shamsi, J.; Urban, A.S.; Imran, M.; De Trizio, L.; Manna, L. Metal Halide Perovskite Nanocrystals: Synthesis, Post-Synthesis Modifications, and Their Optical Properties. *Chem. Rev.* **2019**, 119, 3296–3348, doi:10.1021/acs.chemrev.8b00644.
11. Sum, T.C.; Mathews, N. Advancements in Perovskite Solar Cells: Photophysics behind the Photovoltaics. *Energy Env. Sci* **2014**, 7, 2518–2534, doi:10.1039/C4EE00673A.
12. Goldschmidt, V.M. Die Gesetze der Krystallochemie. *Naturwissenschaften* **1926**, 14, 477–485, doi:10.1007/BF01507527.
13. Krishna, A.; Gottis, S.; Nazeeruddin, M.K.; Sauvage, F. Mixed Dimensional 2D/3D Hybrid Perovskite Absorbers: The Future of Perovskite Solar Cells? *Adv. Funct. Mater.* **2019**, 29, 1806482, doi:10.1002/adfm.201806482.
14. Kovalenko, M.V.; Protesescu, L.; Bodnarchuk, M.I. Properties and Potential Optoelectronic Applications of Lead Halide Perovskite Nanocrystals. *Science* **2017**, 358, 745–750, doi:10.1126/science.aam7093.
15. Travis, W.; Glover, E.N.K.; Bronstein, H.; Scanlon, D.O.; Palgrave, R.G. On the Application of the Tolerance Factor to Inorganic and Hybrid Halide Perovskites: A Revised System. *Chem. Sci.* **2016**, 7, 4548–4556, doi:10.1039/C5SC04845A.
16. Liang, M.; Lin, W.; Lan, Z.; Meng, J.; Zhao, Q.; Zou, X.; Castelli, I.E.; Pullerits, T.; Canton, S.E.; Zheng, K. Electronic Structure and Trap States of Two-Dimensional Ruddlesden–Popper Perovskites with the Relaxed Goldschmidt Tolerance Factor. *ACS Appl. Electron. Mater.* **2020**, 2, 5, 1402-1412, doi:10.1021/acsaelm.0c00179.
17. Fu, Y.; Hautzinger, M.P.; Luo, Z.; Wang, F.; Pan, D.; Aristov, M.M.; Guzei, I.A.; Pan, A.; Zhu, X.; Jin, S. Incorporating Large A Cations into Lead Iodide Perovskite Cages: Relaxed Goldschmidt Tolerance Factor

and Impact on Exciton–Phonon Interaction. *ACS Cent. Sci.* **2019**, 5, 8, 1377-1386, doi:10.1021/acscentsci.9b00367.

18. Mao, L.; Stoumpos, C.C.; Kanatzidis, M.G. Two-Dimensional Hybrid Halide Perovskites: Principles and Promises. *J. Am. Chem. Soc.* **2019**, 141, 1171–1190, doi:10.1021/jacs.8b10851.
19. Stoumpos, C.C.; Cao, D.H.; Clark, D.J.; Young, J.; Rondinelli, J.M.; Jang, J.I.; Hupp, J.T.; Kanatzidis, M.G. Ruddlesden–Popper Hybrid Lead Iodide Perovskite 2D Homologous Semiconductors. *Chem. Mater.* **2016**, 28, 2852–2867, doi:10.1021/acs.chemmater.6b00847.
20. Mao, L.; Ke, W.; Pedesseau, L.; Wu, Y.; Katan, C.; Even, J.; Wasielewski, M.R.; Stoumpos, C.C.; Kanatzidis, M.G. Hybrid Dion–Jacobson 2D Lead Iodide Perovskites. *J. Am. Chem. Soc.* **2018**, 140, 10, 3775-3783, doi:10.1021/jacs.8b00542.
21. Soe, C.M.M.; Stoumpos, C.C.; Kepenekian, M.; Traoré, B.; Tsai, H.; Nie, W.; Wang, B.; Katan, C.; Seshadri, R.; Mohite, A.D.; et al. New Type of 2D Perovskites with Alternating Cations in the Interlayer Space, $(C(NH_2)_3)(CH_3NH_3)_nPb_nI_{3n+1}$: Structure, Properties, and Photovoltaic Performance. *J. Am. Chem. Soc.* **2017**, 139, 45, 16297-16309, doi:10.1021/jacs.7b09096.
22. Lemmerer, A.; Billing, D.G. Synthesis, Characterization and Phase Transitions of the Inorganic–Organic Layered Perovskite-Type Hybrids $[(C_nH_{2n+1}NH_3)_2PbI_4]$, n = 7, 8, 9 and 10. *Dalton Trans.* **2012**, 41, 1146-1157. doi:10.1039/C0DT01805H
23. Chiara, R.; Morana, M.; Folpini, G.; Olivati, A.; Albini, B.; Galinetto, P.; Chelazzi, L.; Ciattini, S.; Fantechi, E.; Serapian, S.A.; et al. The Templating Effect of Diammonium Cations on the Structural and Optical Properties of Lead Bromide Perovskites: A Guide to Design Broad Light Emitters. *J. Mater. Chem. C* **2022**, 10, 12367–12376, doi:10.1039/D2TC02113G.
24. Mao, L.; Guo, P.; Kepenekian, M.; Hadar, I.; Katan, C.; Even, J.; Schaller, R.D.; Stoumpos, C.C.; Kanatzidis, M.G. Structural Diversity in White-Light-Emitting Hybrid Lead Bromide Perovskites. *J. Am. Chem. Soc.* **2018**, 140, 40, 13078-13088, doi:10.1021/jacs.8b08691.

25. Mączka, M.; Zaręba, J.K.; Gągor, A.; Stefańska, D.; Ptak, M.; Roleder, K.; Kajewski, D.; Soszyński, A.; Fedoruk, K.; Sieradzki, A. [Methylhydrazinium]$_2$PbBr$_4$, a Ferroelectric Hybrid Organic–Inorganic Perovskite with Multiple Nonlinear Optical Outputs. *Chem. Mater.* **2021**, 33, 7, 2331-2342, doi: 10.1021/acs.chemmater.0c04440.
26. Billing, D.G.; Lemmerer, A. Synthesis, Characterization and Phase Transitions in the Inorganic–Organic Layered Perovskite-type Hybrids [($C_nH_{2n+1}NH_3$)$_2$$PbI_4$], *n* = 4, 5 and 6. Acta Cryst. *B* **2007**, 63, 735-747, doi:10.1107/S0108768107031758.
27. Billing, D.G.; Lemmerer, A. Synthesis, Characterization and Phase Transitions of the Inorganic–Organic Layered Perovskite-Type Hybrids [($C_nH_{2n+1}NH_3$)$_2$$PbI_4$] (*n* = 12, 14, 16 and 18). *New J. Chem*. **2018**, 32, 1736-1746, doi:10.1039/B805417G.
28. Li, X.; Hoffman, J.; Ke, W.; Chen, M.; Tsai, H.; Nie, W.; Mohite, A.D.; Kepenekian, M.; Katan, C.; Even, J.; et al. Two-Dimensional Halide Perovskites Incorporating Straight Chain Symmetric Diammonium Ions, ($NH_3C_mH_{2m}NH_3$)(CH_3NH_3)$_{n-1}$$Pb_nI_{3n+1}$ (*m* = 4–9; *n* = 1–4). *J. Am. Chem. Soc.* **2018**, 140, 38, 12226-12238, doi:10.1021/jacs.8b07712.
29. Billing, D.G.; Lemmerer, A. Inorganic–Organic Hybrid Materials Incorporating Primary Cyclic Ammonium Cations: The Lead Iodide Series. *CryEngComm*, **2007**, 9, 236-244, doi:10.1039/B618196A.
30. Billing, D.G.; Lemmerer, A. Inorganic–Organic Hybrid Materials Incorporating Primary Cyclic Ammonium Cations: The Lead Bromide and Chloride Series. *CryEngComm*, **2009**, 11, 1549-1562, doi:10.1039/B819455F
31. Tremblay, M.-H.; Bacsa, J.; Zhao, B.; Pulvirenti, F.; Barlow, S.; Marder, S.R. Structures of (4-Y-$C_6H_4CH_2NH_3$)$_2$$PbI_4$ {Y = H, F, Cl, Br, I}: Tuning of Hybrid Organic Inorganic Perovskite Structures from Ruddlesden–Popper to Dion–Jacobson Limits. *Chem. Mater.* **2019**, 31, 6145–6153, doi:10.1021/acs.chemmater.9b01564.
32. Ajayakumar, A.; Muthu, C.; Dev, A.V.; Pious, K.J.; Vijayakumar, C. Two-Dimensional Halide Perovskites: Approaches to Improve

Optoelectronic Properties. *Chem Asian J.* **2022**, 17, e2021010, doi:10.1002/asia.202101075.

33. Li, J.; Wang, H.; Li, D. Self-Trapped Excitons in Two-Dimensional Perovskites. *Front. Optoelectron.* **2020**, 13, 225–234, doi:10.1007/s12200-020-1051-x.
34. Cho, J.; DuBose, J.T.; Le, A.N.T.; Kamat, P.V. Suppressed Halide Ion Migration in 2D Lead Halide Perovskites. *ACS Mater. Lett.* **2020**, 2, 565–570, doi:10.1021/acsmaterialslett.0c00124.
35. He, X.; Wang, Y.; Li, K.; Wang, X.; Liu, P.; Yang, Y.; Liao, Q.; Zhai, T.; Yao, J.; Fu, H. Oriented Growth of Ultrathin Single Crystals of 2D Ruddlesden–Popper Hybrid Lead Iodide Perovskites for High-Performance Photodetectors. *ACS Appl. Mater. Interfaces* **2019**, 11, 17, 15905-15912, doi:10.1021/acsami.9b01825.
36. Smith, I.C.; Hoke, E.T.; Solis-Ibarra, D.; McGehee, M.D.; Karunadasa, H.I. A Layered Hybrid Perovskite Solar-Cell Absorber with Enhanced Moisture Stability. *Angew. Chem. Int. Ed.* **2014**, 53, 11232–11235, doi:10.1002/anie.201406466.
37. Dyksik, M.; Wang, S.; Paritmongkol, W.; Maude, D.K.; Tisdale, W.A.; Baranowski, M.; Plochocka, P. Tuning the Excitonic Properties of the 2D $(PEA)_2(MA)_{n-1}Pb_nI_{3n+1}$ Perovskite Family via Quantum Confinement. *J. Phys. Chem. Lett.* **2021**, 12, 6, 1638-1643, doi:10.1021/acs.jpclett.0c03731.
38. Ghosh, D.; et al. Charge Carrier Dynamics in Two-Dimensional Hybrid Perovskites: Dion–Jacobson vs. Ruddlesden–Popper Phases. *J. Mater. Chem. A,* **2020**, 8, 22009-22022, doi: 10.1039/D0TA07205B.
39. Cheng, B.; et al. Extremely Reduced Dielectric Confinement in Two-Dimensional Hybrid Perovskites with Large Polar Organics. *Commun Phys*, **2018**, 1, 80, doi:10.1038/s42005-018-0082-8.
40. Smith, M.D.; Karunadasa, H.I. White-Light Emission from Layered Halide Perovskites. *Acc. Chem. Res.* **2018**, 51, 3, 619-627, doi:10.1021/acs.accounts.7b00433.
41. Li, S.; Luo, J.; Liu, J.; Tang, J. Self-Trapped Excitons in All-Inorganic Halide Perovskites: Fundamentals, Status, and Potential Applications.

J. Phys. Chem. Lett. **2019**, 10, 8, 1999-2007, doi:10.1021/acs.jpclett.8b03604.

42. Dohner, E.R.; Hoke, E.T.; Karunadasa, H.I. Self-Assembly of Broadband White-Light Emitters. *J. Am. Chem. Soc.* **2014**, 136, 5, 1718-1721, doi:10.1021/ja411045r.
43. Abate, A. Perovskite Solar Cells Go Lead Free. *Joule* **2017**, 1, 659–664, doi:10.1016/j.joule.2017.09.007.
44. De Angelis, F. The Prospect of Lead-Free Perovskite Photovoltaics. *ACS Energy Lett.* **2021**, 6, 1586–1587, doi:10.1021/acsenergylett.1c00636.
45. Hoefler, S.F.; Trimmel, G.; Rath, T. Progress on Lead-Free Metal Halide Perovskites for Photovoltaic Applications: a Review. *Monatsh Chem*. 2017, 148, 795-826, doi:10.1007/s00706-017-1933-9.
46. Bonomi, S.; Malavasi, L. Physical and Chemical Vapor Deposition Methods Applied to All-Inorganic Metal Halide Perovskites. *J. Vac. Sci. Technol. A* **2020**, 38, 060803, doi:10.1116/6.0000568.
47. Cai, Y.; Xie, W.; Ding, H.; Chen, Y.; Thirumal, K.; Wong, L.H.; Mathews, N.; Mhaisalkar, S.G.; Sherburne, M.; Asta, M. Computational Study of Halide Perovskite-Derived A_2BX_6 Inorganic Compounds: Chemical Trends in Electronic Structure and Structural Stability. *Chem. Mater.* **2017**, 29, 7740–7749, doi:10.1021/acs.chemmater.7b02013.
48. Veronese, A.; Patrini, M.; Bajoni, D.; Ciarrocchi, C.; Quadrelli, P.; Malavasi, L. Highly Tunable Emission by Halide Engineering in Lead-Free Perovskite-Derivative Nanocrystals: The Cs_2SnX_6 (X = Cl, Br, Br/I, I) System. *Front. Chem.* **2020**, 8, 35, doi:10.3389/fchem.2020.00035.
49. Liu, D.; Liang, L.; Sa, R. First-Principles Calculations of Structural, Electronic, and Optical Properties of Double Perovskites $Cs_2Sn_{1-B}I6$ (B = Si, Ge; x = 0, 0.25, 0.50, 0.75, 1). *Chem. Phys.* **2021**, 542, 111075, doi:10.1016/j.chemphys.2020.111075.
50. Stoumpos, C.C.; Frazer, L.; Clark, D.J.; Kim, Y.S.; Rhim, S.H.; Freeman, A.J.; Ketterson, J.B.; Jang, J.I.; Kanatzidis, M.G. Hybrid Germanium Iodide Perovskite Semiconductors: Active Lone Pairs, Structural Distortions, Direct and Indirect Energy Gaps, and Strong Nonlinear

Optical Properties. *J. Am. Chem. Soc.* **2015**, 137, 6804–6819, doi:10.1021/jacs.5b01025.

51. Mancini, A.; Quadrelli, P.; Amoroso, G.; Milanese, C.; Boiocchi, M.; Sironi, A.; Patrini, M.; Guizzetti, G.; Malavasi, L. Synthesis, Structural and Optical Characterization of $APbX_3$ (A=methylammonium, Dimethylammonium, Trimethylammonium; X=I, Br, Cl) Hybrid Organic-Inorganic Materials. *J. Solid State Chem.* **2016**, 240, 55–60, doi:10.1016/j.jssc.2016.05.015.
52. Dang, Y.; Liu, X.; Cao, B.; Tao, X. Chiral Halide Perovskite Crystals for Optoelectronic Applications. *Matter* **2021**, *4*, 794–820, doi:10.1016/j.matt.2020.12.018.
53. Pisanu, A.; Ferrara, C.; Quadrelli, P.; Guizzetti, G.; Patrini, M.; Milanese, C.; Tealdi, C.; Malavasi, L. The $FA_{1-x}MA_xPbI_3$ System: Correlations among Stoichiometry Control, Crystal Structure, Optical Properties, and Phase Stability. *J. Phys. Chem. C* **2017**, 121, 8746–8751, doi:10.1021/acs.jpcc.7b01250.
54. Bernasconi, A.; Malavasi, L. Direct Evidence of Permanent Octahedra Distortion in $MAPbBr_3$ Hybrid Perovskite. *ACS Energy Lett.* **2017**, 2, 863–868, doi:10.1021/acsenergylett.7b00139.
55. Bernasconi, A.; Page, K.; Dai, Z.; Tan, L.Z.; Rappe, A.M.; Malavasi, L. Ubiquitous Short-Range Distortion of Hybrid Perovskites and Hydrogen-Bonding Role: The $MAPbCl_3$ Case. *J. Phys. Chem. C* **2018**, 122, 28265–28272, doi:10.1021/acs.jpcc.8b10086.
56. Sun, P.-P.; Li, Q.-S.; Yang, L.-N.; Li, Z.-S. Theoretical Insights into a Potential Lead-Free Hybrid Perovskite: Substituting Pb^{2+} with Ge^{2+}. *Nanoscale* **2016**, 8, 1503–1512, doi:10.1039/C5NR05337D.
57. Nagane, S.; Ghosh, D.; Hoye, R.L.Z.; Zhao, B.; Ahmad, S.; Walker, A.B.; Islam, M.S.; Ogale, S.; Sadhanala, A. Lead-Free Perovskite Semiconductors Based on Germanium–Tin Solid Solutions: Structural and Optoelectronic Properties. *J. Phys. Chem. C* **2018**, 122, 5940–5947, doi:10.1021/acs.jpcc.8b00480.

58. Ju, M.-G.; Dai, J.; Ma, L.; Zeng, X.C. Lead-Free Mixed Tin and Germanium Perovskites for Photovoltaic Application. *J. Am. Chem. Soc.* **2017**, 139, 8038–8043, doi:10.1021/jacs.7b04219.
59. Zhao, Y.-Q.; Liu, B.; Yu, Z.-L.; Ma, J.; Qiang Wan, Q.W.; He, P.; Cai, M.-Q. Strong Ferroelectric Polarization of $CH_3NH_3GeI_3$ with High-Absorption and Mobility Transport Anisotropy: Theoretical Study. *J. Mater. Chem. C* **2017**, 5, 5356–5364, doi:10.1039/C7TC01166K.
60. Ming, W.; Shi, H.; Du, M.-H. Large Dielectric Constant, High Acceptor Density, and Deep Electron Traps in Perovskite Solar Cell Material $CsGeI_3$. *J. Mater. Chem. A* **2016**, 4, 13852–13858, doi:10.1039/C6TA04685A.
61. Tang, L.-C.; Chang, Y.-C.; Huang, J.-Y.; Lee, M.-H.; Chang, C.-S. First Principles Calculations of Linear and Second-Order Optical Responses in Rhombohedrally Distorted Perovskite Ternary Halides, $CsGeX_3$ (X = Cl, Br, and I). *Jpn. J. Appl. Phys.* **2009**, 48, 112402, doi:10.1143/JJAP.48.112402.
62. Jong, U.-G.; Yu, C.-J.; Kye, Y.-H.; Hong, S.-N.; Kim, H.-G. Manifestation of the Thermoelectric Properties in Ge-Based Halide Perovskites. *Phys. Rev. Mater.* **2020**, 4, 075403, doi:10.1103/PhysRevMaterials.4.075403.
63. Seo, D.-K.; Gupta, N.; Whangbo, M.-H.; Hillebrecht, H.; Thiele, G. Pressure-Induced Changes in the Structure and Band Gap of $CsGeX_3$ (X = Cl, Br) Studied by Electronic Band Structure Calculations. *Inorg. Chem.* **1998**, 37, 407–410, doi:10.1021/ic970659e.
64. Liu, D.; Li, Q.; Jing, H.; Wu, K. Pressure-Induced Effects in the Inorganic Halide Perovskite $CsGeI_3$. *RSC Adv.* **2019**, 9, 3279–3284, doi:10.1039/C8RA10251A.
65. Schwarz, U.; Wagner, F.; Syassen, K.; Hillebrecht, H. Effect of Pressure on the Optical-Absorption Edges of $CsGeBr_3$ and $CsGeCl_3$. *Phys. Rev. B* **1996**, 53, 12545–12548, doi:10.1103/PhysRevB.53.12545.
66. Coduri, M.; Shiell, T.B.; Strobel, T.A.; Mahata, A.; Cova, F.; Mosconi, E.; De Angelis, F.; Malavasi, L. Origin of Pressure-Induced Band Gap

Tuning in Tin Halide Perovskites. *Mater. Adv.* **2020**, 1, 2840–2845, doi:10.1039/D0MA00731E.

67. Coduri, M.; Strobel, T.A.; Szafrański, M.; Katrusiak, A.; Mahata, A.; Cova, F.; Bonomi, S.; Mosconi, E.; De Angelis, F.; Malavasi, L. Band Gap Engineering in $MASnBr_3$ and $CsSnBr_3$ Perovskites: Mechanistic Insights through the Application of Pressure. *J. Phys. Chem. Lett.* **2019**, 10, 7398–7405, doi:10.1021/acs.jpclett.9b03046.
68. Postorino, P.; Malavasi, L. Pressure-Induced Effects in Organic–Inorganic Hybrid Perovskites. *J. Phys. Chem. Lett.* **2017**, 8, 2613–2622, doi:10.1021/acs.jpclett.7b00347.
69. Chang, X.; Marongiu, D.; Sarritzu, V.; Sestu, N.; Wang, Q.; Lai, S.; Mattoni, A.; Filippetti, A.; Congiu, F.; Lehmann, A.G.; et al. Layered Germanium Hybrid Perovskite Bromides: Insights from Experiments and First-Principles Calculations. *Adv. Funct. Mater.* **2019**, 29, 1903528, doi:10.1002/adfm.201903528.
70. Cheng, P.; Wu, T.; Zhang, J.; Li, Y.; Liu, J.; Jiang, L.; Mao, X.; Lu, R.-F.; Deng, W.-Q.; Han, K. $(C_6H_5C_2H_4NH_3)_2GeI_4$: A Layered Two-Dimensional Perovskite with Potential for Photovoltaic Applications. *J. Phys. Chem. Lett.* **2017**, 8, 4402–4406, doi:10.1021/acs.jpclett.7b01985.
71. Cheng, P.; Wu, T.; Liu, J.; Deng, W.-Q.; Han, K. Lead-Free, Two-Dimensional Mixed Germanium and Tin Perovskites. *J. Phys. Chem. Lett.* **2018**, 9, 2518–2522, doi:10.1021/acs.jpclett.8b00871.
72. Ma, L.; Ju, M.-G.; Dai, J.; Zeng, X.C. Tin and Germanium Based Two-Dimensional Ruddlesden–Popper Hybrid Perovskites for Potential Lead-Free Photovoltaic and Photoelectronic Applications. *Nanoscale* **2018**, 10, 11314–11319, doi:10.1039/C8NR03589J.
73. Stoumpos, C.C.; Kanatzidis, M.G. The Renaissance of Halide Perovskites and Their Evolution as Emerging Semiconductors. *Acc. Chem. Res.* **2015**, 48, 2791–2802, doi:10.1021/acs.accounts.5b00229.
74. Wang, Y.-L.; Chang, S.; Chen, X.-M.; Ren, Y.-D.; Shi, L.-F.; Liu, Y.-H.; Zhong, H.-Z. Rapid Growth of Halide Perovskite Single Crystals: From Methods to Optimization Control. *Chin. J. Chem.* **2019**, 37, 616-629, doi:10.1002/cjoc.201900071

75. Di, J.; Chang, J.; Liu, S.(F.). Recent Progress of Two-Dimensional Lead Halide Perovskite Single Crystals: Crystal Growth, Physical Properties, and Device Applications. *EcoMat.* **2020**, 2:e12036, doi:10.1002/eom2.12036.
76. Peng, W.; Yin, J.; Ho, K.-T.; Ouellette, O.; Bastiani, M.D.; Murali, B.; Tall, O.E.; Shen, C.; Miao, X.; Pan, J.; et al. Ultralow Self-Doping in Two-Dimensional Hybrid Perovskite Single Crystals. *Nano Lett.* **2017**, 17, 8, 4759-4767, doi:10.1021/acs.nanolett.7b01475.
77. Liu, Y. Multi-Inch Single-Crystalline Perovskite Membrane for High-Detectivity Flexible Photosensors. *Nat. Commun.* **2018**, 9, 5302, doi:10.1038/s41467-018-07440-2.
78. Xiao, M.; Huang, F.; Huang, W.; Dkhissi, Y.; Zhu, Y.; Etheridge, J.; Gray-Weale, A.; Bach, U.; Cheng, Y.-B.; Spiccia, L. A Fast Deposition-Crystallization Procedure for Highly Efficient Lead Iodide Perovskite Thin-Film Solar Cells. *Angew. Chem. Int. Ed.* **2014**, *53*, 9898–9903, doi:0.1002/anie.201405334.
79. Jeon, N.J.; Noh, J.H.; Kim, Y.C.; Yang, W.S.; Ryu, S.; Seok, S.I. Solvent Engineering for High-Performance Inorganic–Organic Hybrid Perovskite Solar Cells. *Nat. Mater.* **2014**, *13*, 897-903, doi:10.1038/nmat4014.
80. Tian, H.; Zhao, L.; Wang, X.; Yeh, Y.-W.; Yao, N.; Rand, B.P.; Ren, T.-L. Extremely Low Operating Current Resistive Memory Based on Exfoliated 2D Perovskite Single Crystals for Neuromorphic Computing. *ACS Nano* **2017**, 11, 12, 12247-12256, doi:10.1021/acsnano.7b05726.
81. Zhang, Y.; et al. Two-Dimensional $(PEA)_2PbBr_4$ Perovskite Single Crystals for a High Performance UV-Detector. *J. Mater. Chem. C,* **2019**, 7, 1584-1591, doi:10.1039/C8TC06129G.
82. Liu, Y.; et al. Surface-Tension-Controlled Crystallization for High-Quality 2D Perovskite Single Crystals for Ultrahigh Photodetection. *Matter,* 1, 465-480, doi:10.1016/j.matt.2019.04.002.
83. Barman, S.; Venkataraman, N.V.; Vasudevan, S.; Seshadri, R. Phase Transitions in the Anchored Organic Bilayers of Long-Chain

Alkylammonium Lead Iodides ($C_nH_{2n+1}NH_3)_2PbI_4$; *n* = 12, 16, 18. *J. Phys. Chem. B,* **2003**, 107, 1875–1883, doi:10.1021/jp026879h.

84. Ishihara, T.; Takahashi, J.; Goto, T. Optical Properties Due to Electronic Transitions in Two-Dimensional Semiconductors ($C_nH_{2n+1}NH_3)_2PbI_4$. *Phys. Rev. B,* **1990**, 42, 11099–11107, doi:10.1103/PhysRevB.42.11099.
85. Kitazawa, N.; Aono, M.; Watanabe, Y. Excitons in Organic–Inorganic Hybrid Compounds ($C_nH_{2n+1}NH_3)_2PbBr_4$ (*n*=4, 5, 7 and 12). *Thin Solid Films* **2010**, 518, 3199–3203, doi:10.1016/j.tsf.2009.09.014.
86. Sichert, J.A.; Hemmerling, A.; Cardenas-Daw, C.; Urban, A.S.; Feldmann, J. Tuning the Optical Bandgap in Layered Hybrid Perovskites through Variation of Alkyl Chain Length. *APL Mater.* **2019**, 7, 041116, doi:10.1063/1.5087296.
87. Sheikh, T.; Nag, A. Mn Doping in Centimeter-Sized Layered 2D Butylammonium Lead Bromide (BA_2PbBr_4) Single Crystals and Their Optical Properties. *J. Phys. Chem. C* **2019**, 123, 9420–9427, doi:10.1021/acs.jpcc.9b01550.
88. Kitazawa, N.; Aono, M.; Watanabe, Y. Synthesis and Luminescence Properties of Lead-Halide Based Organic–Inorganic Layered Perovskite Compounds ($C_nH_{2n+1}NH_3)_2PbI_4$ (*n*=4, 5, 7, 8 and 9). *J. Phys. Chem. Solids* **2011**, 72, 1467–1471, doi:10.1016/j.jpcs.2011.08.029.
89. Zonghan Hong; KiangChong, W.; Yun Ru Ng, A.; Li, M.; Ganguly, R.; Chien Sum, T.; Sen Soo, H. Hydrophobic Metal Halide Perovskites for Visible-Light Photoredox C-C Bond Cleavage and Dehydrogenation Catalysis. *Angew. Chem. Int. Ed.* **2019**, 58, 3456–3460, doi:10.1002/anie.201812225.
90. Saparov, B.; Mitzi, D.B. Organic–Inorganic Perovskites: Structural Versatility for Functional Materials Design. *Chem. Rev.* **2016**, 116, 4558–4596, doi:10.1021/acs.chemrev.5b00715.
91. Smith, M.D.; Crace, E.J.; Jaffe, A.; Karunadasa, H.I. The Diversity of Layered Halide Perovskites. *Annu. Rev. Mater. Res.* **2018**, 48, 111–136, doi:10.1146/annurev-matsci-070317-124406.

92. Cortecchia, D.; Neutzner, S.; Srimath Kandada, A.R.; Mosconi, E.; Meggiolaro, D.; De Angelis, F.; Soci, C.; Petrozza, A. Broadband Emission in Two-Dimensional Hybrid Perovskites: The Role of Structural Deformation. *J. Am. Chem. Soc.* **2017**, 139, 39–42, doi:10.1021/jacs.6b10390.
93. Knutson, J.L.; Martin, J.D.; Mitzi, D.B. Tuning the Band Gap in Hybrid Tin Iodide Perovskite Semiconductors Using Structural Templating. *Inorg. Chem.* **2005**, 44, 4699–4705, doi:10.1021/ic050244q.
94. Xu, Z.; Mitzi, D.B.; Dimitrakopoulos, C.D.; Maxcy, K.R. Semiconducting Perovskites $(2\text{-}XC_6H_4C_2H_4NH_3)_2SnI_4$ (X = F, Cl, Br): Steric Interaction between the Organic and Inorganic Layers. *Inorg. Chem.* **2003**, 42, 2031–2039, doi:10.1021/ic0261474.
95. Wang, P.-X.; Najarian, A.M.; Hao, Z.; Johnston, A.; Voznyy, O.; Hoogland, S.; Sargent, E.H. Structural Distortion and Bandgap Increase of Two-Dimensional Perovskites Induced by Trifluoromethyl Substitution on Spacer Cations. *J. Phys. Chem. Lett.* **2020**, 11, 10144–10149, doi:10.1021/acs.jpclett.0c02909.
96. Sanni, A.M.; Rury, A.S. Kinetic Molecular Cationic Control of Defect-Induced Broadband Light Emission in 2D Hybrid Lead Iodide Perovskites. *J. Phys. Chem. Lett.* **2021**, 12, 101–110, doi:10.1021/acs.jpclett.0c03359.
97. Paritmongkol, W.; Powers, E.R.; Dahod, N.S.; Tisdale, W.A. Two Origins of Broadband Emission in Multilayered 2D Lead Iodide Perovskites. *J. Phys. Chem. Lett.* **2020**, 11, 8565–8572, doi:10.1021/acs.jpclett.0c02214.
98. Yin, J.; Naphade, R.; Gutiérrez Arzaluz, L.; Brédas, J.-L.; Bakr, O.M.; Mohammed, O.F. Modulation of Broadband Emissions in Two-Dimensional ⟨100⟩-Oriented Ruddlesden–Popper Hybrid Perovskites. *ACS Energy Lett.* **2020**, 5, 2149–2155, doi:10.1021/acsenergylett.0c01047.
99. Gautier, R.; Paris, M.; Massuyeau, F. Exciton Self-Trapping in Hybrid Lead Halides: Role of Halogen. *J. Am. Chem. Soc.* **2019**, 141, 12619–12623, doi:10.1021/jacs.9b04262.

100. Smith, M.D.; Connor, B.A.; Karunadasa, H.I. Tuning the Luminescence of Layered Halide Perovskites. *Chem. Rev.* **2019**, 119, 3104–3139, doi:10.1021/acs.chemrev.8b00477.
101. Li, X.; Kepenekian, M.; Li, L.; Dong, H.; Stoumpos, C.C.; Seshadri, R.; Katan, C.; Guo, P.; Even, J.; Kanatzidis, M.G. Tolerance Factor for Stabilizing 3D Hybrid Halide Perovskitoids Using Linear Diammonium Cations. *J. Am. Chem. Soc.* **2022**, 114, 9, 3902-3912, doi:10.1021/jacs.1c11803.
102. Cortecchia, D. White Light Emission in Low-Dimensional Perovskites. *J. Mater. Chem. C* **2019**, 7, 4956-4969, doi:10.1039/C9TC01036J.
103. Smith, M.D. et al. Structural Origins of Broadband Emission from Layered Pb–Br Hybrid Perovskites. *Chem. Sci.* **2017**, 8, 4497-4504, doi:10.1039/C7SC01590A.
104. Romani, L.; Malavasi, L. Solar-Driven Hydrogen Generation by Metal Halide Perovskites: Materials, Approaches, and Mechanistic View. *ACS Omega* **2020**, 5, 25511–25519, doi:10.1021/acsomega.0c03829.
105. Huang, H.; Pradhan, B.; Hofkens, J.; Roeffaers, M.B.J.; Steele, J.A. Solar-Driven Metal Halide Perovskite Photocatalysis: Design, Stability, and Performance. *ACS Energy Lett.* **2020**, 5, 1107–1123, doi:10.1021/acsenergylett.0c00058.
106. Romani, L.; Bala, A.; Kumar, V.; Speltini, A.; Milella, A.; Fracassi, F.; Listorti, A.; Profumo, A.; Malavasi, L. PEA_2SnBr_4: A Water-Stable Lead-Free Two-Dimensional Perovskite and Demonstration of Its Use as a Co-Catalyst in Hydrogen Photogeneration and Organic-Dye Degradation. *J. Mater. Chem. C* **2020**, 8, 9189–9194, doi:10.1039/D0TC02525A.
107. Zheng, C.; Rubel, O. Unraveling the Water Degradation Mechanism of $CH_3NH_3PbI_3$. *J. Phys. Chem. C* **2019**, 123, 19385–19394, doi:10.1021/acs.jpcc.9b05516.
108. Pisanu, A.; Speltini, A.; Quadrelli, P.; Drera, G.; Sangaletti, L.; Malavasi, L. Enhanced Air-Stability of Sn-Based Hybrid Perovskites Induced by Dimethylammonium (DMA): Synthesis, Characterization, Aging and

Hydrogen Photogeneration of the $MA_{1-x}DMA_xSnBr_3$ System. *J. Mater. Chem. C,* **2019**, 7, 7020-7026, doi:10.1039/C9TC01743G.

109. Bresolin, B.-M.; et al. Anchoring Lead-Free Halide $Cs_3Bi_2I_9$ Perovskite on UV100-TiO_2 for Enhanced Photocatalytic Performance. *Sol. Energy Mater. Sol. Cells* **2020**, 204, 110214. doi:10.1016/j.solmat.2019.110214.
110. Jaffe, A.; Lin, Y.; Karunadasa, H.I. Halide Perovskites under Pressure: Accessing New Properties through Lattice Compression. *ACS Energy Lett.* **2017**, 2, 7, 1549-1555, doi:10.1021/acsenergylett.7b00284.
111. Li, Q. Metal Halide Perovskites under Compression. *J. Mater. Chem. A,* **2019**, 7, 16089-16108, doi:10.1039/C9TA04930D.
112. Shi, Y.; et al. Structural Regulation and Optical Behavior of Three-Dimensional Metal Halide Perovskites under Pressure. *J. Mater. Chem. C,* **2020**, 8, 12755-12767, doi:10.1039/D0TC02796K.
113. Szafrański, M.; Katrusiak, A. Photovoltaic Hybrid Perovskites under Pressure. *J. Phys. Chem. Lett.* **2017**, 8, 11, 2496-2506, doi:10.1021/acs.jpclett.7b00520.
114. Marta Morana; Malavasi, L. Pressure Effects on Lead-Free Metal Halide Perovskites: A Route to Design Optimized Materials for Photovoltaics. *Sol. RRL* **2021**, 5, 2100550, doi:10.1002/solr.202100550.
115. Jiao, Y.; Yi, S.; Wang, H.; Li, B.; Hao, W.; Pan, L.; Shi, Y.; Li, X.; Liu, P.; Zhang, H.; et al. Strain Engineering of Metal Halide Perovskites on Coupling Anisotropic Behaviors. *Adv. Funct. Mater.* **2021**, 31, 2007243, doi:10.1002/adfm.202006243.
116. Zhu, C.; Niu, X.; Fu, Y. et al. Strain Engineering in Perovskite Solar Cells and Its Impacts on Carrier Dynamics. *Nat. Commun*. **2019**, 10, 815, doi:10.1038/s41467-019-08507-4.
117. Saidaminov, M.I.; Mohammed, O.F.; Bakr, O.M. Low-Dimensional-Networked Metal Halide Perovskites: The Next Big Thing. *ACS Energy Lett.* **2017**, 2, 889–896, doi:10.1021/acsenergylett.6b00705.
118. Zhou, C.; et al. Low Dimensional Metal Halide Perovskites and Hybrids. *Mater. Sci.* **2019**, 137, 38-65, doi:10.1016/j.mser.2018.12.001.

119. Zhang, L.; Wang, K.; Lin, Y.; Zou, B. Pressure Effects on the Electronic and Optical Properties in Low-Dimensional Metal Halide Perovskites. *J. Phys. Chem. Let.t* **2020**, 11, 12, 4693-4701, doi:10.1021/acs.jpclett.0c01014.
120. Yin, T.; Liu, B.; Yan, J.; Fang, Y.; Chen, M.; Chong, W.K.; Jiang, S.; Kuo, J.-L.; Fang, J.; Liang, P.; et al. Pressure-Engineered Structural and Optical Properties of Two-Dimensional $(C_4H_9NH_3)_2PbI_4$ Perovskite Exfoliated nm-Thin Flakes. *J. Am. Chem. Soc.* **2019**, 141, 3, 1235-1241, doi:10.1021/jacs.8b07765.
121. Yuan, Y.; Liu, X.-F.; Ma, X.; Wang, X.; Li, X.; Xiao, J.; Li, X.; Zhang, H.-L.; Wang, L. Large Band Gap Narrowing and Prolonged Carrier Lifetime of $(C_4H_9NH_3)_2PbI_4$ under High Pressure. *Adv. Sci.* **2019**, 6, 1900240, doi:10.1002/advs.201900240.
122. Matsuishi, K.; Suzuki, K.; Onari, S.; Gregoryanz, E.; Hemley, R.J.; Mao, H.K. Excitonic States of Alkylammonium Lead-Iodide Layered Perovskite Semiconductors under Hydrostatic Pressure to 25 GPa. *Phys. Stat. Sol. (b)* 2001, 223, 177, doi:10.1002/1521-3951(200101)223:1<177::AID-PSSB177>3.0.CO;2-J.
123. Klotz, S.; Chervin, J.-C.; Munsch, P.; Le Marchand, G. Hydrostatic Limits of 11 Pressure Transmitting Media. *J. Phys. Appl. Phys.* **2009**, 42, 075413, doi:10.1088/0022-3727/42/7/075413.
124. Zha, C.-S.; Mao, H.; Hemley, R.J. Elasticity of MgO and a Primary Pressure Scale to 55 GPa. *PNAS* **2000**, 97(25), 13494-13499.

Publications

Reproduced

Chiara, R.; Morana, M.; Malavasi, L. Germanium-Based Halide Perovskites: Materials, Properties, and Applications. *ChemPlusChem.* (**2021**) 86, 879–888.

Chiara R., Morana M., Boiocchi M., Coduri M., Striccoli M., Fracassi F., Listorti A., Mahata A., Quadrelli P., Gaboardi M., Milanese C., Bindi L., De Angelis F., Malavasi L. Role of Spacer Cations and Structural Distortion in Two-Dimensional Germanium Halide Perovskites. *J. Mater. Chem. C* (**2021**) 9, 9899-9906.

Morana M., **Chiara R.**, Joseph B., Shiell T. B., Strobel T. A., Coduri M., Accorsi G., Tuissi A., Simbula A., Pitzalis F., Mura A., Bongiovanni G., Malavasi, L. Pressure response of decylammonium-containing 2D iodide perovskites. *iScience* 25,104057, April 15 (**2022**).

Chiara, R.; Morana, M.; Folpini, G.; Olivati, A.; Albini, B.; Galinetto, P.; Chelazzi, L.; Ciattini, S.; Fantechi, E.; Serapian, S. A.; Petrozza, A.; Malavasi, L. The templating effect of diammonium cations on structural and optical properties of lead bromide perovskites: a guide to design broad light emitters. *J. Mater. Chem. C.* (**2022**) 10, 12367-12376.

Romani, L.; Speltini, A.; **Chiara, R.**; Morana, M.; Medina-Llamas, M.; Coccia, C.; Armenise, V.; Colella, S.; Milella, A.; Listorti, A.; Profumo, A.; Ambrosio, F.; Mosconi, E.; Pau, R.; Pitzalis, F.; Simbula, A.; Ricciarelli, D.; Saba, M.; De Angelis, F.; Malavasi, L. Air and water stable and photocatalytically active germanium-based 2D perovskites by organic spacer engineering. Accepted by Elsevier (December 11, **2022**) in *Cell Reports Physical Science*.

Other publications

Chiara, R.; Ciftci, Y. O.; Queloz, V. I. E.; Nazeeruddin, M. K.; Grancini, G.; Malavasi, L. Green-Emitting Lead-Free Cs_4SnBr_4 Zero-Dimensional Perovskite Nanocrystals with Improved Air Stability. *J. Phys. Chem. Lett.* (**2020**), 11, 3, 618-623.

Corti, M.; **Chiara, R.**; Romani, L.; Mannucci, B.; Malavasi, L.; Quadrelli, P. g-C_3N_4/metal halide perovskite composite as photocatalysts for singlet oxygen generation processes for the preparation of various oxidized synthons. *Catal. Sci. Technol*. (**2021**), 11, 2292-2298.

Corti, M.; Bonomi, S.; **Chiara, R.**; Romani, L.; Quadrelli, P.; Malavasi, L. Application of metal halide perovskites as photocatalysts in organic reactions. *Inorganics* (**2021**) 9, 56.

Corti, M.; **Chiara, R.**; Romani, L.; Mannucci, B.; Malavasi, L.; Quadrelli, P. Nanocrystals perovskites photocatalyzed singlet oxygen generation for light-driven organic reactions. *Photochemical & Photobiological Sciences* (**2022**) 21, 613-624.